PHYSICAL PROPERTIES OF PULSED LASER ABLATION AND CHEMICAL VAPOUR DEPOSITION SYNTHESISED CARBON NANOSPHERES

Author
Othmane Mouane
othmane.mouane@gmail.com
Supervised by
Prof. Elias Sideras-Haddad
elias.sideras-haddad@wits.ac.za
Co-Supervised by
Prof. Daniel Wamwangi
Daniel.Wamwangi@wits.ac.za
& Prof. Andrew Forbes
Andrew.Forbes@wits.ac.za

A Thesis submitted to the Faculty of Science, University of the Witwatersrand, Johannesburg, in fulfilment of the requirements for the degree of Doctor of Philosophy.

Johannesburg, 2021.

DECLARATION

I, Othmane Mouane, declare that this thesis is my own, unaided work. It is being submitted for the Degree of Doctor of Philosophy at the University of the Witwatersrand, Johannesburg. It has not been submitted before for any degree or examination at any other University.

(Signature of candidate)

The twenty-first of April 2021 in Johannesburg.

DEDICATION

I dedicate this thesis to:

My Parents for their love,
My Brother, Sisters, and Friends for their support,
and those who believed in my potential and helped me to grow.

"You Will Never Forget a Person Who Came to You with a Torch in The Dark".

ACKNOWLEDGEMENTS

I would like to thank my supervisors for their continuous support, encouragement, patience, and availability along my PhD studies. I am very grateful to my supervisor, Prof. Elias Sideras-Haddad, who was very generous in sharing his extensive knowledge and experience as a physicist and a person and I will never forget the long hours and energy he devoted so I could finalise this thesis. Many thanks to Prof. Daniel Wamwangi who helped me to overcome obstacles and challenges that I faced while conducting my research. I also enjoyed the regular and exciting discussions about physics whenever I passed by his offices. This work could not be completed without the assistance of the technical staff, especially Mr. Gerrard Peters, of the department of physics and other facilities of the university.

I would like to acknowledge the Material Physics Research Institute in the School of Physics, University of the Witwatersrand (grant 7690), the National Research Foundation of South Africa (grant Sideras-Haddad 99105), the National Laser Centre-CSIR (LREQA32) and African Laser Centre of CSIR (LHIP 500) for financial and research infrastructure support.

Finally, I would like to thank my family and close friends for their patience and unconditional support.

ABSTRACT

Monodispersed and uniform carbon nanospheres with a diameter in the range of 40-50 nm were synthesised with a new and fast laser based developed technique. The synthesis method consisted of the irradiation of Highly Oriented Pyrolytic Graphite (HOPG) sample by an ultraviolet pulsed laser with power densities in the order of 10^8 $W.cm^{-2}$ under the presence of hydrogen gas. The morphological and elemental characterisation carried with Scanning Electron Microscopy revealed the existence of two different regions within a shockwave generated at the irradiated spots and the formation of pure carbon nanostructures with spherical shape. Raman line-scans confirmed the nano-structuration of the HOPG surfaces and the appearance of carbon nanospheres at the shockwave regions. The detailed study of different parameters which influenced the growth process allowed the uncovering of the optimum conditions at which the formed carbon nanospheres were of high quality and of high production rate. It was found that the fluence threshold and the hydrogen presence were crucial for the formation of these carbon nanospheres. In addition, the critical thermodynamic parameters (pressure and temperature) generated by the pulsed laser were calculated. This provided a better insight regarding the phase transformation of HOPG from a macro to a nano-structure and the nucleation process which leads to the formation of carbon nanospheres.

The second part of this work focused on investigating the magnetic and electric properties of different carbon nanospheres synthesised by chemical vapour deposition, using a state of the art physical property measurement system (PPMS). Scanning electron microscopy imaging of the two investigated sets of carbon nanospheres, grown under slightly different conditions, revealed a difference in size with diameters of about 200 and 400 nm respectively. Induced coupled plasma mass spectroscopy showed the presence of ferromagnetic impurities such as Fe, and Ni at concentration levels less than 120 and 3 ppm respectively. PPMS magnetic measurements of the two samples showed two different characteristics. In Sample “A”, with nanospheres of about 200 nm in diameter, clear ferromagnetism behaviour was observed, while in sample “B”, diamagnetic behaviour was observed except at low temperature (>10 K), at which clear

superparamagnetic behaviour is observed. The electrical measurements on a network of carbon nanospheres of sample “A” revealed a semiconductor characteristic and showed a variable range hopping class of conductivity in agreement with work conducted on carbon nanotubes networks.

CONTENTS

LIST OF FIGURES

Chapter I

Chapter II

Chapter III

Chapter IV

Chapter V

Chapter VI

Chapter VII

LIST OF TABLES

Chapter III

Chapter V

Chapter VI

Chapter VII

CHAPTER I

1 INTRODUCTION

1.1 Background

Carbon is the fourth abundant element in the universe and exists in many different forms. Diamond and graphite exist in natural form and are considered as the most known bulk carbon allotropes for centuries. They can also be synthesised in laboratories. The physical and electronic properties of these two carbon allotropes, are different and unique, and depend on the electronic structure and type of chemical bonding formed which result in extreme differences between the two. Diamond is a transparent and hard material with a very weak electrical conductivity, while graphite is an opaque, soft and good electrical conductor. The different chemical bonds of diamond and graphite are the sp^3 and sp^2 hybridisation respectively resulting in different atomic lattice structures as shown in Figure 1.1.

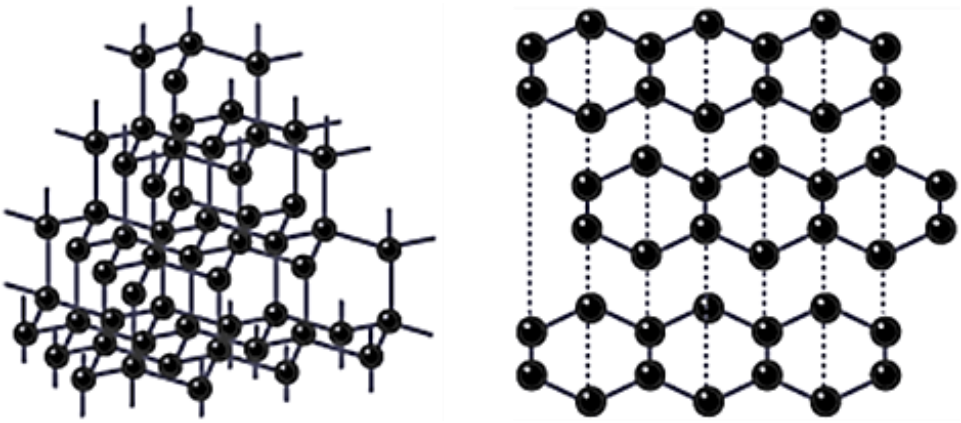

Figure 1.1: Atomic bonding structures of diamond and graphite [1].

In a graphite crystal, planar parallel layers of carbon atoms (also known as graphene) are stacked along the z-direction and bonded by Van der Waal interactions. While in the planar x-y direction, the monolayers of carbon are arranged in a hexagonal

structure. Each carbon atom within the layer forms σ bonds with three neighbouring carbon atoms. The remaining free electrons of the carbon atoms become delocalised, and circulate freely within the lattice. These two types of bonding σ and π are responsible for the high electrical and mechanical properties of graphite and determine the two known structures of graphite.

The first structure (rhombohedral) is found in nature and forms a sequence of ABCABC stack of layers, in which the projection of any atom on the next layer is located at the centre of the hexagon of carbon atoms. The second possible structure is a sequence of ABAB stacks. This hexagonal structure is typical for Highly Oriented Pyrolytic Graphite (HOPG) and can be obtained by heating up the natural graphite (ABCABC) to 1000 °C (Figure 1.2).

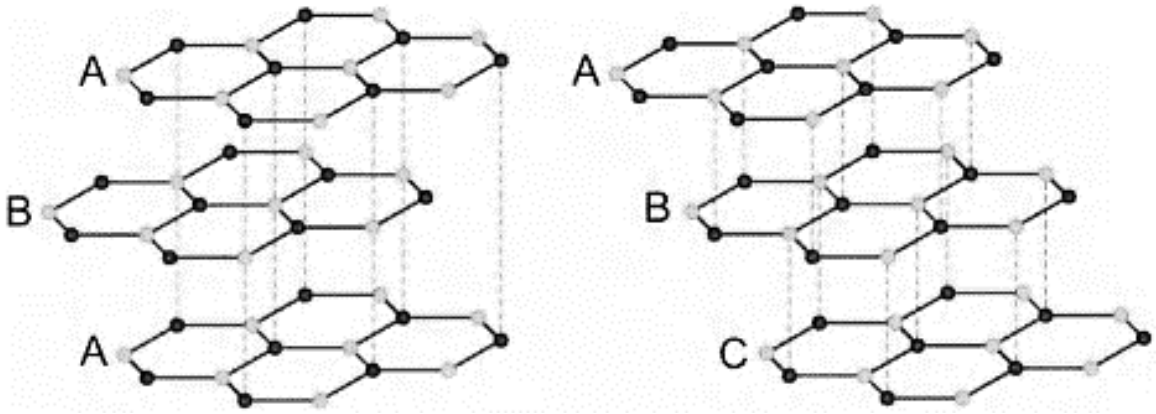

Figure 1.2: The structure of HOPG (ABAB stack) and the natural graphite (ABCABC or Rhombohedral stacking) [2].

In diamond on the other hand, the arrangement of carbon atoms is of tetrahedral type, with covalent bonds in the three directions. This configuration of carbon atoms is responsible for the hardness and insulating behaviour of the diamond. By the mid of the twentieth century, more carbon allotropes were discovered. Glassy carbon [3], hexagonal structure of diamond [4], and amorphous carbon were the new forms of synthesised carbon allotropes.

In the 1980s, Kroto *et al.* synthesised Buckminsterfullerene (C_{60}) by vaporisation of graphite with intense laser ablation [5], and introduced the first carbon nanomaterial. Kroto and co-workers reported that the formed clusters consisted of 60 carbon atoms arranged in a spherical form.

Besides C_{60}, carbon nanotubes are considered as the most well-known carbon nanostructures. Iigima and co-workers staggered the scientific community with the synthesis and the description of the structure of double-walled and multi-walled carbon nanotubes [6], then two years later of the single-wallet carbon nanotubes [7]. Such discovery of carbon nanotubes attracted the interest of researchers because of the lattice structures, the unique physical properties, and their potential to be used in mainstream applications in electronics, medicine and healthcare diagnosis, environment, and energy.

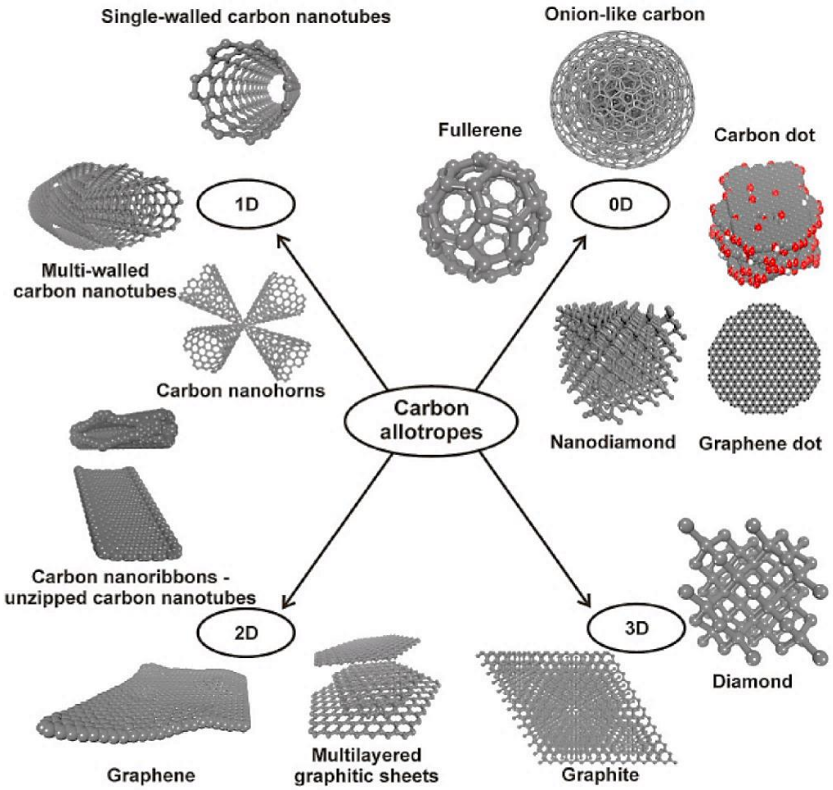

Figure 1.3: Different carbon allotropes based on their dimensionality [1].

In addition to carbon nanotubes, multiple carbon nanomaterials of different forms and structures were identified and studied. Carbon nanofoams [8], nanodots [9],

nanofibers [10], nanorods [11], nanospheres [12], graphene [13] and other nanocarbon allotropes considered as cousins to fullerene and carbon nanotubes and all together formed a base for carbon nanoscience. Their unique properties have been the main focus of research over the last twenty years.

Magnetism in carbon nanomaterials is an interesting, exciting and complicated research domain. In general, carbon allotropes exhibit a diamagnetic behaviour with a susceptibility in the range of $-(10^{-4}\text{-}10^{-6})$ emu.g^{-1} per magnetic field unit [14]. However, several reports revealed exceptional magnetic behaviour in a variety of carbon materials. Unexpected ferromagnetic characteristics were observed firstly in pure and polymerised C_{60} at high temperatures around 800 K [15], [16]. Another astonishing and unforeseen discovery came along with the observation of induced ferromagnetic behaviour in a wide range of temperatures [17], [18] after low MeV–proton irradiation of HOPG. Through laborious and methodical work, it was shown that the magnetisation was not related to ferromagnetic impurities. Furthermore, ferromagnetic-like hysteresis magnetisation loops were observed in additional carbon-based nanomaterials, such as nanographite [19], [20], carbon encapsulating Ar nanoparticles [21], composites of HOPG nanospheres [14], carbon nanofoams [22], [23], and microporous carbon [24]. The origin of this anomalous magnetic behaviour observed in carbon-based materials is still unclear and different assumptions are reported. Numerous research groups have speculated that the manifestation of these unusual magnetic properties are due to topographic defects, positive or negative surface curvatures (such as in graphene), and the chemical nature of the edges such as the mixture of sp_2 and sp_3 hybridised states [21]. The role of hydrogen and oxygen has also been investigated with respect to catalysing the process and inducing the observed magnetic behaviour in the carbon systems [21]. Li *et al*. reported also that morphological characteristics such as the crystallinity and size affect the magnetic properties in pyrolytic carbon [14]. Moreover, there is evidence that the magnetism originates from *s-p* symmetry unpaired electrons at structural defects rather than of *d* or *f* electrons of the impurities [14]. Such ferromagnetic properties in carbon nanomaterials can of course lead to technological breakthrough in spintronic, telecommunications, biology, and medicine.

On the other hand, carbon nanomaterials and specifically carbon nanotubes were reported to possess extraordinary electrical conductivity comparable to metals [25]. Contrary to the magnetism, the electrical properties are well understood in carbon nanomaterials, and are related mostly to the electronic structure and the dimensions of the nanomaterials. Thus, their use as composites, thin films, and networks in electronic and electrical applications overcame a number of issues (heavy weight, electromagnetic interference, lightning strikes and corrosion), and replaced metallic elements in different industries including aerospace.

Several techniques, such as arc-discharge, laser ablation and plasma processes, shock compression and chemical vapour deposition have been developed for the synthesis of carbon nanomaterials [12]. Chemical vapour deposition (CVD) offers a controllable process of synthesis, which is based on the decomposition of a precursor (solid or gas), mostly hydrocarbon, in a reactor [26]. Also, the introduction of a catalyst is possible during the synthesis process, which allows the modification of the structure as well as the dimension of the produced carbon nanomaterial.

Among these techniques, Pulsed Laser Ablation (PLA) attracted more interest in the production of carbon materials and other applications such as patterning, micromachining, and artwork restoration [27]. This synthesis method has been fostered by the invention of lasers in the ’60s and offers numerous advantages such as simplicity, automation, and the possibility to carry the ablation in vacuum or gaseous and liquid environments. Besides, the use of a pulsed laser allows for greater control of pressure and temperature to a localized zone over a large range of values without changing the chemistry of the irradiated material.

Most of the research work on the production of carbon nanostructures by PLA has been based predominantly in liquid confinement. Ismail *et al.* demonstrated the synthesis of multi-walled carbon nanotubes and carbon nanoparticles by PLA in water for optoelectronic applications [28]. In a number of recent works, the synthesis of graphene nanosheets, graphene like-phase, and carbon nanoparticles by PLA in different liquids

has been reported [29]–[34]. Moreover, the formation of nanodiamonds by PLA continues to attract research interest in several research groups [35]–[38]. Fabbro and co-Workers [39] have shown that the PLA outcomes depend heavily on the confining medium and on laser-based parameters such as fluence, wavelength, and pulse width. These variables are critical as they determine the size, morphology, and structure of the produced carbon nanomaterials. Also it is reported that the role of the confinement amplifies the effect of the thermodynamic parameters (local pressure at impact and temperature gradient) to the ablated zone by the generated shockwaves [39].

1.2 Overview of the present/research work

In contrast to carbon nanostructures mentioned above, and given the variety of applications that require different physico-chemical characteristics and properties, synthesis techniques of carbon nanomaterials, such as carbon nanospheres, have not been investigated thoroughly for the fabrication of low cost, pure, and high-quality nanospheres of 20-100 nm in diameter. Also, the produced carbon nanomaterials by synthesis methods such as arc-discharge, plasma processes, shock compression and chemical vapour deposition may contain an amount of impurities in the level of part per million. The impurities such as Fe, Ni, and Co can interfere with the carbon nanospheres properties either positively or negatively. An improvement of the size distribution and the formation process of carbon nanospheres in comparaison with previous synthesis techniques is expected to offer new solutions to the challenges in applications involving specially carbon nanospheres.

In this study, a new, simple, and reproducible synthesis technique of uniform and monodispersed carbon nanospheres was investigated and developed. This novel method uses an ultraviolet nanosecond pulsed laser to irradiate a HOPG sample in a background gas of hydrogen. The experimental system and research procedures for the study of the different influencing parameters such as energy density, gas flow rate, number of pulses and repetition rate are presented in Chapter III. The purpose of the parameters study was

to understand the physical interactions and processes involved in the formation of the observed carbon nanospheres. Thus in Chapter II, the fundamentals and the relevant basic physics with respect to laser-solid interactions, material response, ablation and synthesis processes, the thermodynamics of nucleation, as well as shockwaves generation by pulsed lasers, are explained in details. The different characterisation methods used to investigate the carbon nanostructures are presented and described in Chapter IV.

In Chapter V and VI, the results and the discussion of the laser ablation of HOPG are reported respectively. In the results chapter, presentation of the newly observed nanostructures due to the laser irradiation is given with a number of visual images provided by extensive scanning electron microscopy studies for many different parameter sets. Results from Raman spectroscopy studies provide crucial information regarding the crystallinity, structure, bonding type and the domain size of the formed carbon nanostructures. Also, the effect of the important parameters that influence the growth of carbon nanospheres are outlined and the crystallites size of the formed carbon nanospheres are calculated using the ratios of the D and G bands intensities I_D/I_G in the Raman spectra.

In chapter VI, the physical process including effects and contributions of each parameter that lead to the formation of the carbon nanospheres are described in details. The thermodynamic parameters such as the pressure and the temperature are calculated, and a phase diagram which shows the critical parameter-area at which the carbon nanospheres are likely to be formed is deduced. Also, by the use of the calculated thermodynamic parameters, quantities such as the supersaturation is calculated and important information in regards to the nucleation process is revealed.

In Chapter VII, the magnetic and electric properties of carbon nanospheres synthesised by chemical vapour deposition are presented and discussed. The morphology and elemental composition of carbon nanospheres are investigated by scanning electron microscopy, while, induced coupled plasma mass spectroscopy is

performed to detect traces of impurities at the part per million level within the samples. Additional analysis of the samples making use of Mössbauer spectroscopy was also carried out. The last chapter of the thesis is a summary of the research work that was implemented and shared in the previous chapters and proposition of ideas about future research works is mentioned.

CHAPTER II

2 FUNDAMENTALS OF LASER-SOLID INTERACTIONS IN THE SYNTHESIS OF NANOMATERIALS

2.1 Introduction

Laser irradiation is widely used in applications with respect to material treatment, processing, developing and in engineering of novel structures. Since 60s, the first experimental studies were carried out with pulsed lasers impinging on materials, fundamental permanent changes in the properties have been observed as a result of the interaction between the incident photons and the physical surface system. In this way, transformation of the local chemistry, morphology, and crystal structure constitute the main modifications caused by such interactions on the surface or interface of materials [40], [41].

One of the major features which characterises pulsed laser beams is the large power density deposition on the surface of the solid, which is of the order of ~10^{10} -10^{14} W/cm^2, within time scales in the range between a few femtoseconds to nanoseconds. The initial recipient of this large power density is the electronic system of the surface. The intense electronic excitations and ionizations which take place, together with the highly spatial localization of the excitation, result in surface modifications as well as formation of nano-defects on exactly the surface of the target material. This is the most important aspect of the photon-surface interactions and opens up the possibilities of applications such as surface nano-structuring and surface patterning and structural and electronic surface modifications.

The interaction between the laser and the solid surface is complex and depends on many different parameters such as the photon energy, the duration of the interaction

and hence the pulse width, and the electronic structure of the material itself. A series of interaction events take place within different time scales within the surface of the interacting material which is summarised in Figure 2.1 [42]. The light absorption process inside the material also plays the role of a secondary source of energy. The response of the solid to this secondary source is expressed as heat transfer and dissipation in three dimensions within the material.

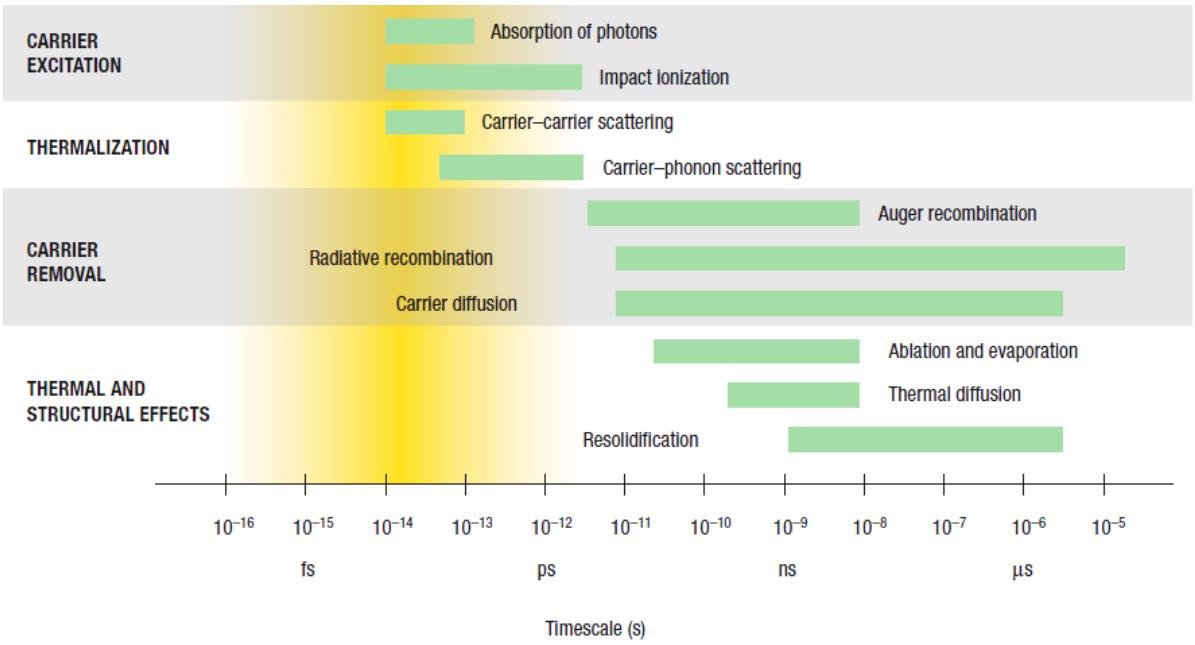

Figure 2.1: Timescales of various electrons and lattice processes in laser-excited solids. Each green bar represents an approximate range of characteristic times over a range of carrier densities [42].

2.2 Laser-Material Interaction

In the next sections, a theoretical framework underlining the principles and the equations describing the propagation of light and its absorption by the material are provided. With respect to the heat flow, the focus is on a mathematical treatment of the physical aspects governing the thermal response of a material under photon irradiation.

2.2.1 Propagation of light in materials

The propagation of a monochromatic, coherent, and linearly polarized light beam is described by plane waves of an electric field E and a magnetic field H according to:

$$I = |E \times H| \tag{2.1}$$

The interaction between an electromagnetic wave and an electron results in a force exerted on the electron given by [43]

$$f = -e\left[E + \left(\frac{n_1}{c}\right)(v \times H)\right] \tag{2.2}$$

where e, n_1, c and v are the electron charge, refractive index of the medium, speed of light, and the electron velocity [43]. In most cases, the ratio v/c is very small rendering the contribution due to the magnetic field negligible. Therefore the phenomena of light-matter interaction which will be discussed in the next sections are strictly related therefore to the term $-\mathrm{eE}$ in the expression above.

The electric field of a laser beam propagating in a homogenous and non-absorbing medium is defined as

$$E = E_0 e^{-i\left(\frac{2\pi z}{\lambda} - \omega t\right)} \tag{2.3}$$

with z indicating the direction of propagation, λ and ω are the wavelength and the angular frequency. The wavelength λ is also expressed as a function of the angular frequency, the index of refraction of the medium of propagation n_1, and the speed of light c as $\lambda = (2\pi\mathrm{c}/\omega\mathrm{n}_1)$.

The interaction between the laser and the surface of a material is mediated by three major processes, namely;

- Absorption in which a portion of the light intensity is absorbed into the material, the parameter that describes this process is absorbance, *A* which is related to the extinction coefficient of the materials.
- Reflection, *R* for which some of the light is reflected at the interface of two media having distinct refractive indices.
- Transmission, *T*, where by the non-absorbed light is refracted and enabled to penetrate the medium without absorption.
- In the presence of surface corrugations, diffuse reflection contributes to an additional interaction also known as scattering, represented by *S*.

The reflectivity R, of an irradiated and weakly absorbing material depends on the relative index of refraction of the two media. The reflectivity coefficient R is derived from Fresnel equations [44] in the form;

$$R = \left(\frac{n_1 - n_{mat}}{n_1 + n_{mat}}\right)^2 \tag{2.4}$$

Expression (2.4) defines the reflection coefficient for a laser beam at normal incidence to a solid of refractive index $\mathrm{n_{mat}}$ in a medium of refractive index $\mathrm{n_1}$. This reflectivity is due to the discontinuity of the index of refraction, which is complex for an absorbing medium of the form $\mathrm{n = n_1 + in_2}$. The imaginary term is the so-called the extinction coefficient and is directly linked to the absorption coefficient of the irradiance (2.5) [43].

$$\alpha = -\frac{1}{I}\frac{dI}{dz} = \frac{4\pi n_2}{\lambda} \tag{2.5}$$

The inverse of the absorption coefficient is defined as the optical penetration δ [43], [44], for which the irradiance of the transmitted laser beam reduces to $1/e$ of its initial value at the material crossing point (interface).

Figure 2.2 below shows the optical penetration for a range of wavelengths from 0 to 2000 nm for diverse range of metals and semiconductors [45]. It is evident that the optical absorption depth is significantly smaller for metals than semiconductors, such as Silicon and Germanium, due to the contribution of free electrons in metals. The absorption depths for insulators become comparable to the ones for metals only for short wavelengths below the UV optical region, where upon the photons have sufficient energy for interband transitions.

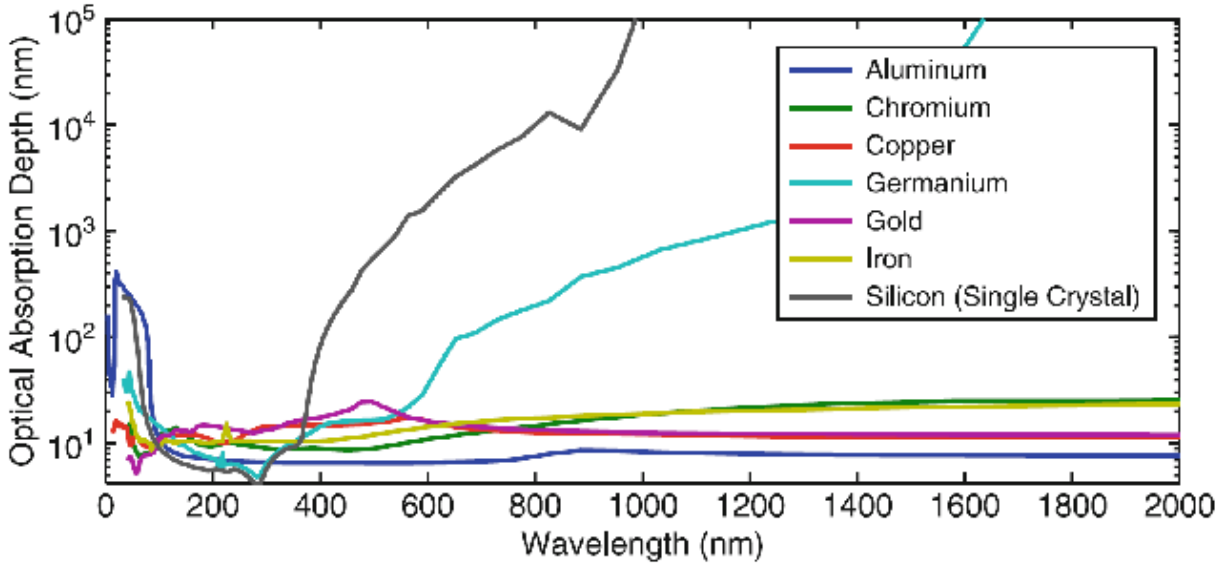

Figure 2.2: Optical absorption depths for several materials over a range of wavelengths [45].

As the laser beam traverses the bulk of the material, its irradiance decreases with depth. The rate of decrease is determined by the absorption coefficient of the material. By integrating (2.5) the well-known Beer-Lambert expression is derived for the exponential decay of the beam irradiance along the depth of the material which depends on its absorption coefficient α [43], [44];

$$I(z) = I_0 e^{-\alpha z} \tag{2.6}$$

where I_0 is the irradiance at the interface, and z is the depth along the direction of propagation.

2.2.2 Laser-Metal interaction

Optical absorption in materials is attributed to the coupling of photons into existing electronic or vibrational states. In semiconductors and insulators, photo-absorption occurs mainly through resonant electronic excitations from the valence band to the conduction band (inter-band transitions), or inside bands (intra-band transitions) [46]. The excited electronic states can then transfer energy to the lattice by coupling to phonon states. In this manner, only photons with energies larger than the band-gap can induce such electronic transitions and be absorbed. For photons with energies below the band-gap, no absorption is expected, except if defects or impurities are present with energy states within the energy gap.

In metals, electrons located in states near the Fermi energy level, known as free electrons or conduction electrons, are responsible for the optical absorption. Those free electrons do not possess any resonance frequency and therefore, the energy transfer to the lattice phonons takes place through collisions.

The response of a material to an electromagnetic field is described by the complex dielectric function of a free electron given by [43]:

$$\epsilon = 1 + \omega_p^2 \frac{-\tau_e^2 + i\,{}^{\tau_e}/_{\omega}}{1 + \tau_e^2 \omega^2} = \epsilon_1 + i\epsilon_2 \,. \tag{2.7}$$

where ω_p is the electron plasma frequency, $\omega_p = \sqrt{(N_e e^2)/(m_e \epsilon_0)}$, and is identified as a significant parameter which links the electron density of a metal N_e to its optical

properties [43]. The real and imaginary parts of the dielectric function are associated with the terms of the complex refraction index $\mathrm{n} = \mathrm{n}_1 + \mathrm{in}_2$ by [43]:

$$\epsilon_1 = n_1^2 - n_2^2\,; \qquad \epsilon_2 = 2n_1n_2. \tag{2.8}$$

When the value of the frequency is equal to the plasma frequency, which is in the ultraviolet for most metals, both the real part of the dielectric function ϵ_1 and the index of refraction n_1 vanish.

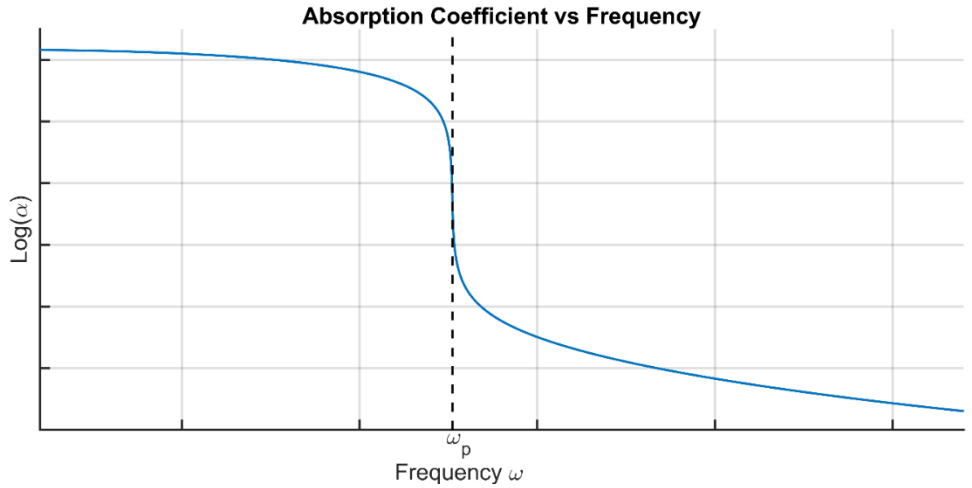

Figure 2.3: The absorption coefficient of a free-electron metal (expression (2.5)) as a function of the frequency. The graph is plotted for $\hbar\omega = 8.3\ \mathrm{eV}$, corresponding to $N_e = 5.10^{22} cm^{-3}$, and $\hbar/\tau_e = 0.02\mathrm{eV}$ [43]. The dashed lines represent the plasma frequency ω_p position within the frequency axes.

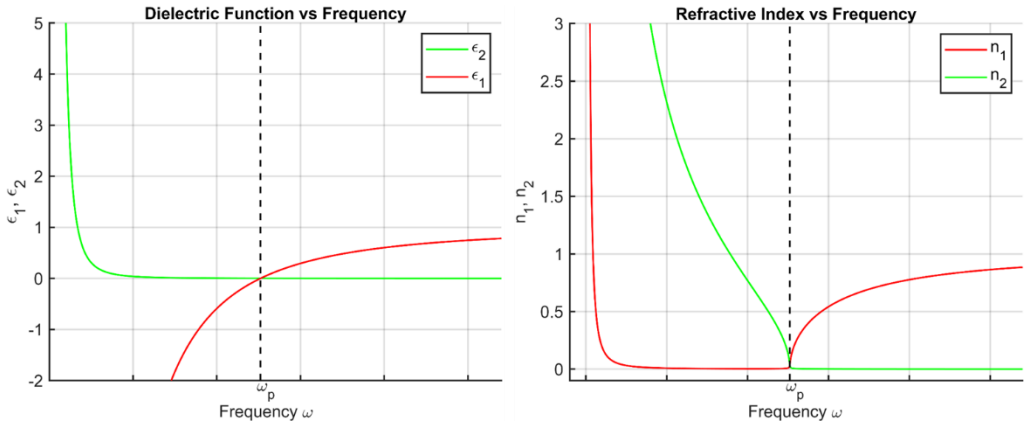

Figure 2.4: Frequency dependence of the dielectric function and refractive index of a free-electron metal, for $\hbar\omega = 8.3\ \mathrm{eV}$, corresponding to $\mathrm{N_e} = 5.10^{22}\mathrm{cm}^{-3}$, and $\hbar/\tau_e = 0.02\mathrm{eV}$ [43].

As seen in Figure 2.3 and Figure 2.4, the two different optical properties or regimes are separated by the plasma frequency. For $\omega < \omega_p$, the electrons screen the electric field of the irradiating light, consequently, high absorbance and reflectivity are observed (Figure 2.4). In contrast, for $\omega > \omega_p$, the absorbance and the reflectivity drop dramatically (Figure 2.4), because the electrons cannot respond fast enough to screen the electric field component of the E-M wave with frequencies above the plasma frequency [43], [44].

The optical properties discussed above concern ideal metals. In reality, interband transition, plasmons, polaritons, and diffused scattered electrons can be excited [47]. Impurities, contaminants, and defects existing on the surface of the metal, are the source of these electronic and vibrational states mentioned above.

From a classical approach, the oscillatory energy of an electron oscillating in phase with the light beam electric field is converted into thermal energy, known also as collisional heating. Such conversion is caused by knocking-out electrons out of phase during collisions with nuclei [48] and the resulting energy transfer from electrons to the lattice phonons lead to thermalisation. The energy relaxation time, or thermalisation time, for which the total kinetic energy is transmitted to the lattice is in the order of 10^{-12}-10^{-10} s for most metals [46].

2.3 Aspects of the material response to laser irradiation

The manner in which the surface or the bulk of a material responds following a pulsed laser irradiation and subsequent absorption of the laser energy depends both on the material type (semiconductor, insulator, or metal) as well as on the parameters describing the impacting laser pulse which define the so-called interaction conditions. These interaction conditions are the ones which will determine the type of physical processes and modifications which take place.

2.3.1 Laser parameters determining the induced effects of irradiated surfaces

The most important laser parameters involved in different processes are the energy density, number of pulses, and excitation rate.

Naturally, the power density deposited on the surface or the bulk of the material determines the effect of the interaction. The fluence of the laser pulse used, therefore, is of utmost importance. Each material is characterized by a well-defined fluence threshold value, for which the early stage of changes and modifications by laser irradiation of its surface begins to manifest. For a massive fluence or deposited energy density, light irradiation can result in melting, sublimation, or material ejection. Otherwise, for fluences below the threshold value, the density of the hot electrons is small and as a result, no major changes on the surface of the target occur. There is a plethora of studies by many different research groups in which the fluence dependence of material modifications has been investigated and threshold values were determined for a range of materials such as graphite [49], [50], graphene [51], or some metals, and semiconductors [52].

As discussed in the preceding sections, laser-material interaction is a complicated physical phenomenon, and it involves irradiations with either a “single laser pulse” or “multiple laser pulses”. These cause different types of responses from the surface or bulk of the material. In the case of multiple laser pulses, laser induced interactions become more complicated and difficult to model. The multiple pulses irradiation has a cumulative character and increases therefore the energy deposited on the material surface, resulting in heat accumulation and decrease of the fluence threshold, simply known as incubation effect, are involved in the process. This results in further damage and deformations, and different transitions and structures are witnessed [53], [54]. The multiple laser pulses irradiation is applied in several applications, such as optical hyper-doping, and surface texturing [55]–[57], in which incubation effects play the principal role.

The repetition rate of the laser is another critical parameter, which determines timing aspects of the interaction and in that sense it influences critically the type of mechanism involved in the modifications and changes taking place on the material surface. For example, an excitation rate lower than the thermalisation rate of the material produces a purely thermal effect. This is known as the photo-thermal mechanism (pyrolytic). Instead, in the case of an excitation rate higher than thermalisation rate, the modifications are expressed by photo-decomposition (breaking bonds). During this later mechanism, the temperature remains comparatively constant, which implies that any induced changes on the target surface are not due to thermal effects and are rather attributed to photo-chemical processes [58]. In certain cases, a combination of thermal and non-thermal effects is also observed and is due to a photo-physical mechanism [46].

The parameters cited above are not the only ones influencing induced modifications on the material surface. Other parameters such as the pulse width (nanosecond, femtosecond etc.) which determines the dwell time of the laser [56], as well as the wavelength (UV, IR), and the ambient environment (reactive or non-reactive atmosphere) can play a principal role in defining the laser-solid interactions and the mechanisms involved resulting in different surface modifications.

2.3.2 Laser heating of materials

As explained in section 2.2.1, the response of a material to absorbed light is primarily an electronic phenomenon based on the coupling of the oscillatory energy states of electrons and the phonons states which in this manner result to thermal energy after the collision [48]. This energy conversion or energy equipartition is a complicated step in which the energy transmission involves different conversion mechanisms depending on the energy relaxation time τ_E [59]. For a metal, the characteristic energy relaxation time τ_E is in the order of 10^{-13} s, while for non-metallic materials is of the order between 10^{-12}-10^{-6} s [44]. The laser irradiated region is therefore characterised by the flow heat within the irradiated spot. This temperature distribution within the material can be deduced by the heat flow equation [46]:

$$\frac{K(x,T)}{D(x,T)}\frac{\partial T(x,t)}{\partial t} - \nabla[K(x,T)\nabla T(x,t)] + \frac{K(x,T)}{D(x,T)}\, v_s \nabla T(x,t) = Q(x,t) \qquad (2.9)$$

with $\mathrm{D(x,T)} = \mathrm{K(x,T)}/(\rho(\mathrm{x,T})\mathrm{c_p(x,T)})$ being the thermal diffusivity, where $\mathrm{K(x,T)}$, $\rho(\mathrm{x,T})$, $\mathrm{c_p(x,T)}$, and $\mathrm{v_s(x,T)}$ are the thermal conductivity, mass density, specific heat (as a function of temperature), and velocity of the substrate relative to the heat source of the irradiated surface. $\rho(\mathrm{x,T})$, $\mathrm{c_p(x,T)}$ are both at constant pressure.

In many standard textbooks on laser-material interactions and laser heating of material, the solutions of the volumetric heating rate $\mathrm{Q(x,t)}$ are derived either analytically, by assuming material properties as constants [44], [59], or numerically [60], by using methods like the finite difference model. In the analytic approach, certain assumptions and boundary conditions which depend on the particular problem are considered.

In the simple case of a pulsed laser of a Gaussian beam profile and rectangular pulse length τ, and by assuming that $\mathrm{K(x,T)}$, $\rho(\mathrm{x,T})$, $\mathrm{c_p(x,T)}$, are independent of temperature, then the temperature rise can be written as follows [61]:

$$\Delta T_c = \frac{\sqrt{2}\, P(1-R)}{\sqrt{\pi^3}\, K w_0} \arctan(A) \qquad (2.10)$$

where $\mathrm{A} = (2\sqrt{2\mathrm{Dt}})/\mathrm{w_0}$, and $\mathrm{t} \leq \tau$. P, R, and $\mathrm{w_0}$ are the power, the reflectivity, and the beam waist. At the instance when the laser pulse stops, the impacted region begins to cool down and a cooling temperature is established. In order to estimate this cooling temperature for a rectangular pulse shape τ, the previous expression (2.10) is modified to describe the temperature beyond the pulse duration. The cooling temperature for the cooling cycle after one pulse irradiation is given by [61]:

$$\Delta T_c = \frac{\sqrt{2}\,P(1-R)}{\sqrt{\pi^3}\,K w_0}\arctan\left(\frac{A-B}{1+AB}\right) \tag{2.11}$$

where $B = 2\sqrt{2D\,(t-\tau)}/w_0$, and $t > \tau$. Figure 2.5 below shows the rise of temperature and subsequent cooling of a Silicon target irradiated by a nanosecond laser of a pulse width of 20 ns. The material constants for Si are taken from "*Chemical Processing with Lasers*" by D. Bäuerle [61].

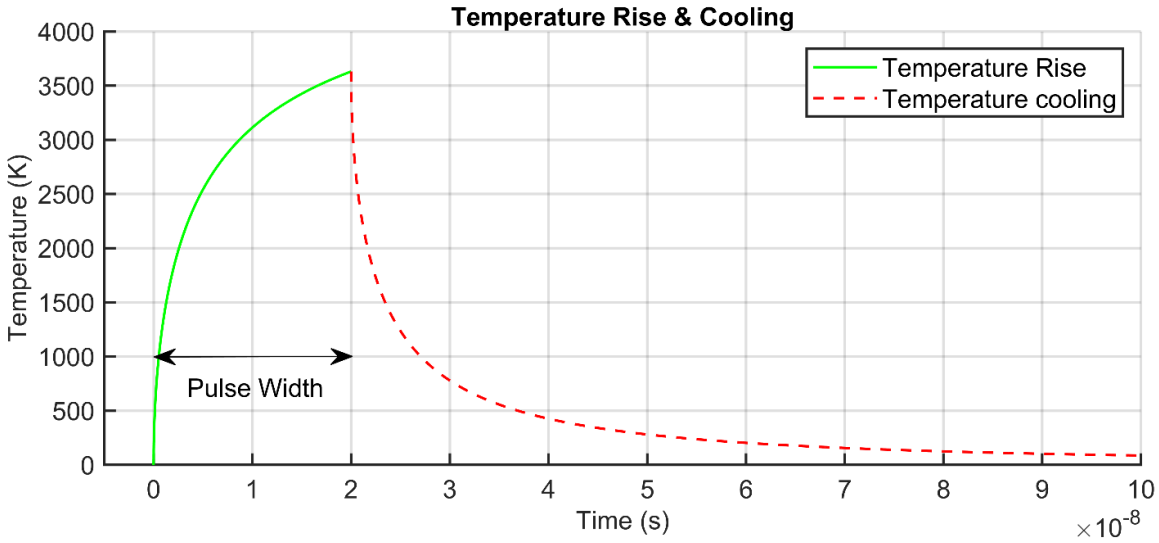

Figure 2.5: Temperature rise and cooling for Si irradiated by a laser with a pulse width of 20 ns.

In the case of thin films, with a thickness smaller than thermal diffusion length, exposed to a pulsed laser, the heating process with respect to the temperature evolution is treated in a more simplified manner [59]. The temperature rise of a surface as a function of time is given by [62], [63]:

$$\Delta T(t) = \frac{I_0}{K}\left(\frac{k}{\pi}\right)^{\frac{1}{2}}\int_0^t f(t-\tau)\tau^{-\frac{1}{2}}\,d\tau \tag{2.12}$$

with $f(t)$ is the normalized pulse shape over time. I_0, and τ are the power density and the pulse width of the irradiating light beam. K, and k are the thermal conductivity and thermal diffusivity of the irradiated material.

For a laser pulse of squared shape, the temperature within the material at ambient temperature T_0 can be written as [59]:

$$T(t) = T_0 + \Delta T_{max}\left(\sqrt{\frac{t}{\tau}} - [t > \tau]\sqrt{\frac{t}{\tau - 1}}\right) \quad (2.13)$$

where $\Delta T_{max} = (2I_0/K)(k\tau/\pi)^{1/2}$, is the maximum temperature rise reached at $t = \tau$, and $[t > \tau]$ is equal to 1 for $t > \tau$, and 0 otherwise.

The example above of the temperature rise and cooling (2.13) due to the absorption of a squared pulse of light, concerns an ideal case and gives a rough estimate of the temperature change. In some studies, [63], [64], more realistic descriptions of the pulse shape are taken into account which includes approximations for the shape of the pulse in terms of its rising and decay times. This results in more realistic predictions of the surface temperature.

2.3.3 Effects induced during laser-material interactions

The generated heat flow and distribution inside a material upon laser irradiation is the source of different phenomena, non-equilibrium and equilibrium processes. These series of processes depend strongly on the energy density and other parameters as explained in previous sections and cause local changes, and phase transitions on the material surface. Irradiating a material with a nanosecond laser pulse generates a heating rate of the order of 10^9 $K.s^{-1}$ [44], and it reaches higher values with a femtosecond lasers. In the next sections, description of different material responses mainly the ones involving photo-thermal effects is provided.

a. Melting

Surface melting occurs for fluences above the melting threshold of a material. The energy densities for which the melting is manifested are limited since evaporation is more plausible compared to melting [62]. There are two different forms of surface melting; thermal and non-thermal. Thermal melting occurs when the electrons transfer their energy to the lattice by electron-phonon collisions [65]. This process takes time over a few picoseconds, hence melting is considered purely thermal for irradiation with lasers of a pulse-width longer than few picoseconds. Non-thermal melting is another way of disordering a crystal. Contrary to thermal melting, the non-thermal melting occurs much faster and within a few femtoseconds, before the lattice heats up by the transferred energy from the electrons [42], [66], [67]. After the melting, solidification is established. The reformed melted material depends mainly on the rate of solidification. For slow resolidification rates, the new structure of the material contains larger grains compared to the original one. Instead, rapid quenching, can result in the formation of defects, supersaturated solutes [68], and metastable phases.

If the irradiating energy density is lower than the melting threshold, the hot carriers transfer their energy to the lattice, by electron-electron, or electron-phonon interactions through a process known as annealing.

Surface melting is used in a wide range of applications from surface homogenization, microstructure refinement to laser welding, and surface hardening.

b. Ablation and shockwave generation

During pulse laser irradiation of a material the absorption of its pulse energy can cause material removal. This process of material extraction is known as laser ablation and it also makes use of intense continuous wave (CW) lasers. Here too, as in the case of surface melting, in order for laser ablation to occur, an energy density above a specific threshold value must be applied. Typical energy density threshold are between 1 to 10 $J.cm^{-2}$ for metals, while for other types of materials such as semiconductors and

insulators, threshold values are much lower [44], [46]. Interestingly, the threshold value can diminish as the number of pulses increases, caused by effects as defects, and incubation effects involved in the process of irradiation. In addition to the fluence, laser ablation depends also on the type of material and its properties, as well as on the laser parameters such as wavelength, and the dwell time.

There are three different types of laser ablation:

i. Photo-thermal ablation

This process is characterised by a rapid energy dissipation within the material. The photo-thermal ablation involves low excitation energy and is associated mostly with evaporation and sublimation. As the laser fluence is increased, the localized temperature rises, resulting in more fractures and deformations by thermo-elastic waves generated in the solid by thermal expansion and its coupling with the rate of strain [56]. These elastic waves of stresses are principally observed at low energy densities since at higher energy density, the recoil pressure generates the so-called shockwaves. For higher fluences, leading to very high temperatures, phenomena like explosive boiling are manifested. This phase explosion is due to rapid homogenous nucleation and expansion of vapour bubbles fragments [69], caused by the rapid heating of the material as it reaches a thermodynamic critical temperature. Another form of boiling described as normal boiling, is caused by the heterogeneous nucleation of vapour bubbles.

ii. Photo-chemical ablation

Photo-chemical ablation also known as a non-thermal mechanism, occurs when the excitation time is shorter than the relaxation time. This process is therefore well observed with ultrafast lasers, in which direct breaking bonds and phenomena as Coulomb explosion [49], [70], and a-thermal phase transitions are demonstrated, as consequences of direct ionization, and formation of dense electron-hole plasmas [44]. This material sputtering from the surface is simply explained by insufficient time for the laser energy to spread in the surrounding of the irradiated region of the material before

being ejected. Short pulse lengths, therefore, are important in material ejection applications.

iii. Photo-physical ablation

In this process, both thermal and photochemical effects are involved. This mechanism is characterised by induced transformation which is mostly led by the non-thermal excitation [71], [72]. Photo-physical ablation is often used in photo-medical applications and biosciences in order to ablate cell tissues and tumours with pulsed nanosecond lasers [73].

In all cases described previously, the intense absorption of the laser beam focused onto the solid material, generates a highly directed plume above the irradiated zone. This vapour plume may initially contain solid, and liquid clusters, which under further ablation become ionized, causing a phase transformation, and the outcome is hot dense plasma. The blow-off of this high-temperature plasma, just a few microns above the irradiated zone, induces a mechanical impulse to this solid material causing plastic deformation and work hardening. The result of the pressure waves produced on the target surface is two shockwaves travelling within the solid. The first shockwave propagates through the sample plane, and the second travel laterally in the plane of the sample.

A number of research groups have tried to model laser-induced shockwaves and the relevant applications in deformation processing [74]. The generation of shockwaves is induced in two different ways; direct, or confined ablation. For direct ablation, the hot plasma generated expands freely in the surrounding atmospheric air, or vacuum. In this regime, the pressure reaches values from a few kBar to 50 MBars by varying the incident laser beam intensity. The pressure effect lasts for a duration of a laser pulse due to the rapid cooling of the generated plasma.

In the case of confined ablation, the confinement is due to the overlay of a transparent medium such as water [35], [36], [38], glass [75]–[77] or quartz, with the surface of the laser irradiated material. Contrary to the direct ablation, the expansion of

the plasma produced in the confined ablation regime is delayed by the confining medium. The use of confinement was firstly applied in order to enhance the pressure applied to the surface by these stress waves needed in metallurgical, and medical applications. Fabbro *et al*, showed in their paper titled ‘’Physical study of laser-produced plasma in confined geometry’’ [39], how is easy to reach 50 kBar, and that the shockwaves duration is 2-3 times longer as compared to the one generated by direct ablation.

Some studies focused on enhancing the effect of the shockwaves generated on the plane of the target for specialise applications mentioned above. For this purpose, the laser beam was shaped in a ring form and by controlling its spatial intensity profile, spherical and cylindrical shockwaves are generated. It was also seen that two different shock waves are formed; one propagating inward to the centre, and a second shockwave diverging and travelling outward [76], [78].

As described in the previous paragraph, the launched shockwave is an outcome of a pressure effect. Quantifying the amount of pressure applied to the material surface is very important in understanding any phase transformations, transitions or damage caused by the shockwave. A large number of publications were focused on developing a physical model of these two regimes of ablation, and analytical models were proposed in order to reach a better agreement with the experimental results and to draw a model based comparison between the direct and confined ablation regimes. Phipps *et al.* [79], developed a model for direct ablation in vacuum in which the pressure generated by a pulsed laser of intensity I, wavelength λ, and dwell time τ can be calculated:

$$\frac{P_d}{I} = b\left(I\lambda\sqrt{\tau}\right)^n \tag{2.14}$$

with b and n being dependent on the irradiated material.

Using this empirical formula, Fabbro *et al.* confirmed the validity of the physical model of Phipps *et al.* and the final expression for the pressure produced by direct ablation was the following [39],

$$P_d(\text{kbars}) = 3.93\, I^{0.7}(\text{GW.cm}^{-2})\, \lambda^{-0.3}(\mu\text{m})\tau^{-0.15}(\text{ns}). \tag{2.15}$$

In the case of confined ablation, two different simple cases were modelled. In the first, the interface between the target and confining material is purely solid. For this case the final pressure expression derived is given by [39]:

$$P_c(\text{kbars}) = 0.10 \left(\frac{\alpha}{2\alpha+3}\right)^{\frac{1}{2}} Z^{\frac{1}{2}}\, (\text{g.cm}^{-2}.\text{s}^{-1})\, I_0^{\frac{1}{2}}\, (\text{GW.cm}^{-2}), \tag{2.16}$$

where α is a constant (0.1-0.2), and z is the shock impedance of material, which is the density of the material ρ multiplied by the shock velocity D.

In the second case, the medium between the sample and the confining material is considered to be an ideal gas. The approximated generated pressure by the plasma can then be calculated from the following expression (2.17) [39],

$$P_c(\text{kbars}) = 32.2 \left(\frac{\alpha}{2\alpha+3}\right)^{\frac{2}{3}} \rho_0^{\frac{1}{3}}\, (\text{g.cm}^{-3})\, I_0^{\frac{2}{3}}\, (\text{GW.cm}^{-2}). \tag{2.17}$$

By replacing the density ρ_0 by $4\rho_{\text{gas}}$ in the expression (2.17), this analytical model proposed by Fabbro *et al.* [39] can also be used to calculate the pressure due to a pulsed laser, for a solid confined in a gas environment with a density ρ_{gas}. The evolution of the pressure-induced as a function of laser power density for direct ablation as well as for confined ablation with solid and gas confining media is shown in Figure 2.6.

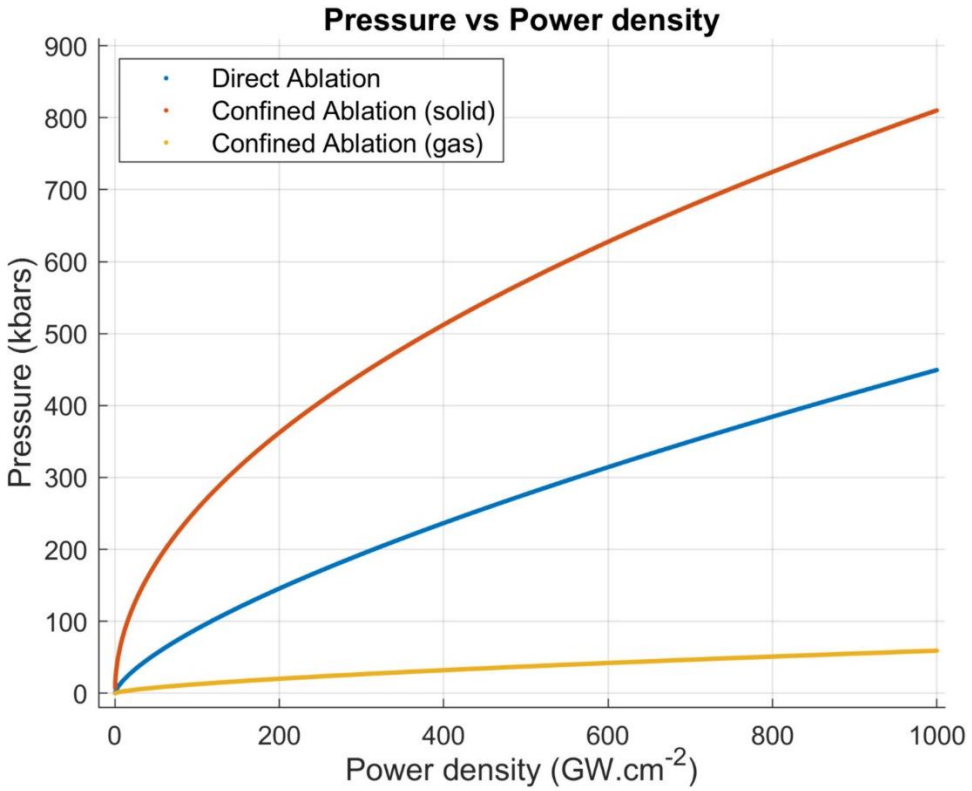

Figure 2.6: Pressure evolution as a function of power densities over a range 10^{8}-10^{12} W.cm^{-2}, for direct (2.15), and confined ablation (2.17) [39].

2.4 Laser synthesis of nanomaterials and its nucleation

The synthesis of nanomaterials including nanocrystals, nanowires, and nanocomposites, and the control of their sizes and shapes have been the focus of research in recent decades due to their important role in a wide range of specific applications from electronic nano-transistors and nano-sensors to health care.

2.4.1 The Basics of Pulsed Laser Ablation

Pulsed Laser Ablation (PLA) is a materials synthesis technique based on the removal of a volume of material due to the interaction of a pulsed laser characterized by a power density, pulse duration, and repetition rate with the bulk-material. The simplicity of the implementation of the PLA makes it a widespread technique in the field of

nanostructures synthesis [80], [81] and thin-film growth, known also as Pulsed Laser Deposition (PLD) [82]–[84].

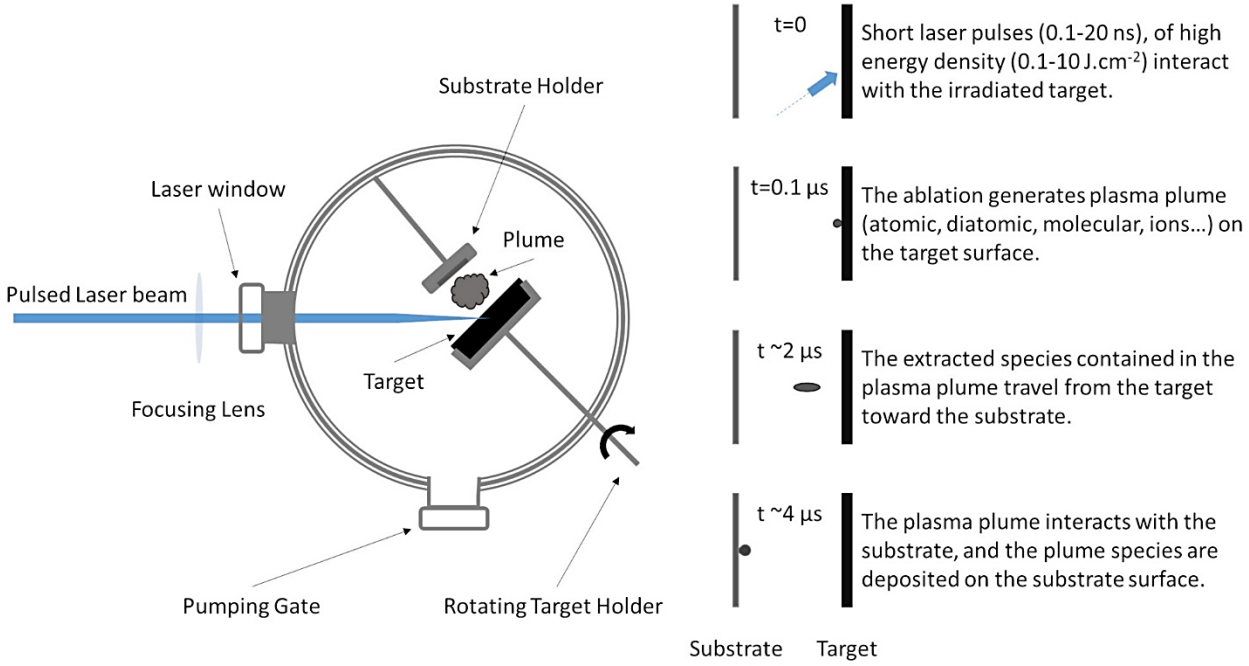

Figure 2.7: Illustration of the PLD system and the time evolution of the different processes which take place upon the laser pulse impact [83].

The principle of PLA is based on focusing a laser beam onto a liquid or a rotating target of solid form, placed priory in a chamber under a high pressure, as illustrated schematically in Figure 2.7. In PLA, the process of material ablation is driven by photo-thermal (evaporation and sublimation), photo-mechanical (shockwaves), or both mechanisms at the same time [44], [46], [85]. It correlates mostly with the pulsed laser in use (ns, ps, or fs lasers). While each pulse strikes the surface of the target, phase transition of the ejected materials to a metastable form, mainly vapour, is manifested by ablation.

The dense vapour formed within a few picoseconds is described as luminous, dense, and hot and is observed right above the ablation region [44], [84], [85], as explained in section 2.3.3. The generated plume consists initially of mostly clusters of atomic, diatomic, or even smaller species (Figure 2.8). Thereafter, the metastable

plasma-plume nucleates and grows into a stable solid form. This subsequently, by interacting with the substrate, is deposited on the surface in the form of films or nanostructures.

The created plasma-plume depends typically on the bulk material properties, as well as the energy density, wavelength, and pulse width of the laser. While the generation of the plasma-plume depends largely on the threshold of the applied energy density, the wavelength and the pulse length have a significant effect on the amount and interactions of the laser-induced plasma [80], [84], [85].

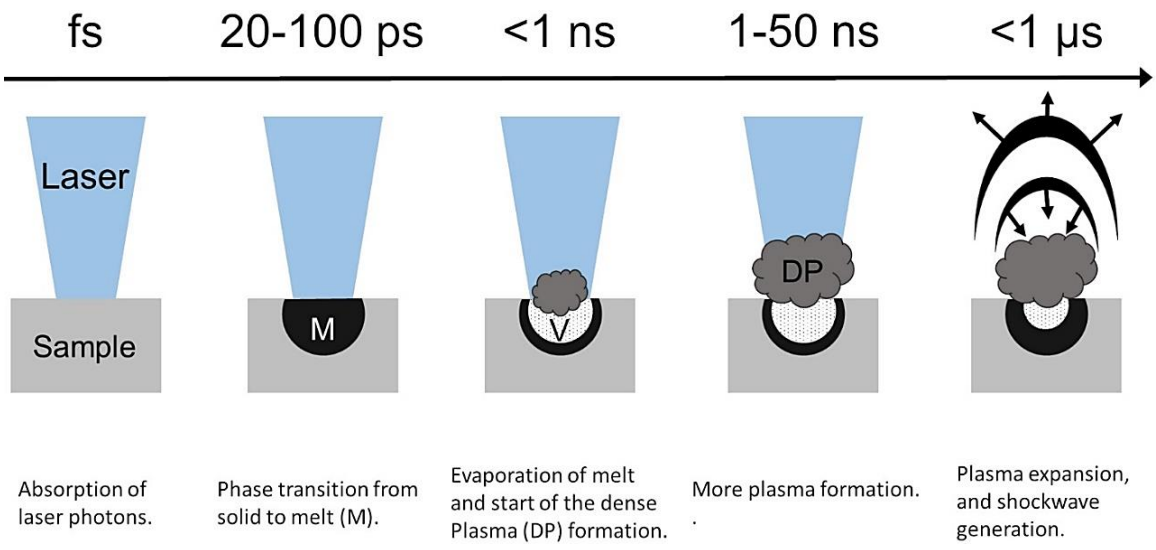

Figure 2.8: The dynamics of nanosecond PLA (plasma expansion and shockwaves generation) [80].

For an important amount of material removal, the ablation with laser energy greater than the threshold, and UV wavelength are recommended [83]–[85]. The penetration depth of UV light, in metals, is indeed very short (tens of nanometres, Figure 2.2) and as a consequence, most of the energy of the photons is deposited on the surface and eases in this way the removal of the material. The use of lasers with short-wavelengths which carry higher energies (the photon energies at 266 and 157 nm are respectively 4.66 and 7.90 eV [84]) facilitates evaporation, sublimation and ionization of the surface of the bulk material, and the generation of the plasma. In addition, the ablation with lasers of short

penetration depths limits extractions of micro-sized particles, which are undesirable for the growth of multilayer structured films [83].

The pulse width is important as it affects the ablation process and the plasma generation. Nanoseconds (ns) and femtoseconds (fs) pulsed lasers are the most common lasers used in PLA. The choice of the pulse width depends on the application and the material to be synthesised. While ns lasers are mostly used in thin-film growth [82]–[84], fs lasers are used in nanoparticle synthesis in particular [80], [81], with different ablation mechanisms triggered in the two applications.

In the case of fs ablation, the pulse duration is very short and the laser-plasma interaction is not possible. As there is insufficient time for the energy to be transferred to the lattice (non-metal materials) or to the electronic systems (metal materials), the thermal-waves are unable to dissipate within the material surface [44], [84] resulting in locally generated high temperatures and pressures due to the accumulation effect. In contrary to fs lasers, the irradiation of the bulk-material with ns lasers allows the heatwaves to propagate on the material surface. A larger deposition time of the laser energy favours the coupling with the electronic and the lattice vibrational modes. The heating, melting, and evaporation of the ablated surface lead to a plasma-plume formation as described in Figure 2.8. In addition, the large time-scale of the pulse permits interaction between the created plume and laser pulse.

PLA offers the possibility of the ablation of materials in diverse environments. For films growth, the ablation is carried either in a vacuum or with the presence of a background gas, depending on the desired physical and chemical characteristics of the thin-film under-growth [83], [84]. The background gas is either an inert or reactive gas. Argon is considered as the most used inert gas in PLA. The role of the inert gas is to cool the surrounding environment of the created plume and to reduce the kinetic energy of the vapour flux.

The introduction of reactive gases in PLD is important for the growth of multi-components thin-films [83]. The reactive species from gases like methane, oxygen, and nitrogen, interact with the laser-induced plume. The outcome of these reactions is a vapour flux of atomic or diatomic species, depending on the injected reactive gas. The formed plasma-plume after interaction contains molecular species of atoms or clusters from the ablated bulk and the active background gas. This plasma-plume acts as the material source for the formation of multi-components deposited thin-films [83].

The background gas plays also the role of a confining environment, which slows the plasma-plume expansion, as mentioned in section 2.3.3. In addition, the generation of shockwaves is another reason for background gas injection. The expansion of the ablated plume in the background gas produces a compression on the surface. The pressure of the system (plume and background gas) reaches equilibrium by the launch of a shockwave (details in 2.3.3). This mechanism depends on the plume dynamics, and is strictly related to the type and pressure of the reactive gas [84].

2.4.2 Thermodynamics of nucleation

The major step leading to nanomaterials growth after laser ablation is nucleation which promotes growth. In general, any system of fluid or solid in a metastable phase tries to occupy a lower energy state to reach equilibrium. The difference in the Gibbs free energy from one state to another is the thermodynamic driving force for any phase transformation such as from metastable to stable state [86]. This phase transition is defined as a first-order transition and begins with the nucleation of the new phase stable clusters [87]. The nucleation is directly related to the variation in the Gibbs free energy (G_{old} - G_{new}), defined as the supersaturation $\Delta\mu$ [86]. Physically, this quantity $\Delta\mu$ is the gain in free energy per clusters (atoms, molecules), directly related to the transition from an old to a new manifested phase. μ_{old} and μ_{new} represent the chemical potentials for the new and the old phases respectively, and M is the number of atoms or molecules contained in the volume of the system.

$$\Delta\mu \equiv \frac{G_{old} - G_{new}}{M} \equiv \mu_{old} - \mu_{new} \tag{2.18}$$

The quantity Δμ accounts for the nucleation in different simple cases in the course of the first-order transition, such as boiling, evaporation, or sublimation, and complex ones such as the crystallization of melt or the polymorphic transformation by cooling.

In the case of a first-order transition from a vapour form to a solid or liquid form, the value of Δμ determines whether the nucleation can proceed. From the literature, the Gibbs free energy of Van der Waals (VDW) fluid kept at constant temperature T, pressure P, for which the fluid is in stable thermodynamic equilibrium, is given as [87]:

$$G(V', T') = G_{\mathrm{ref}}(T') + MkT_{cr}\left[\frac{3P'V'}{8} - \frac{9}{8V'} - T'\ln(3V' - 1)\right] \tag{2.19}$$

with $\mathrm{V}' = \frac{\mathrm{V}}{\mathrm{V_{cr}}}, \mathrm{T}' = \frac{\mathrm{T}}{\mathrm{T_{cr}}}$ are respectively the reduced volume and reduced temperature expressed as a function of the fluid's critical volume and temperature, $\mathrm{G_{ref}}$ is the reference energy, and k is the Boltzmann constant. For the case described above, in which the old phase is vapour with Gibbs free energy $\mathrm{G_{old}}$, and the new phase is either liquid or solid with Gibbs free energy $\mathrm{G_{new}}$, the old and new Gibbs free energy are [86]:

$$G_{old} = G_{ref}(T') + MkT_{cr}\left[\frac{3P'V_g'}{8} - \frac{9}{8V_g'} - T'\ln\left(3V_g' - 1\right)\right] \tag{2.20}$$

,

$$G_{new} = G_{ref}(T') + MkT_{cr}\left[\frac{3P'V_{s,l}'}{8} - \frac{9}{8V_{s,l}'} - T'\ln\left(3V_{s,l}' - 1\right)\right] \tag{2.21}$$

By substituting G_{old} and G_{new} in the supersaturation formula , $\Delta\mu$, becomes

$$\Delta\mu = kT_{cr}\{T' \ln[(3V'_{s,l} - 1)/(3V'_g - 1)] + (9/8)(\frac{1}{V'_{s,l}} - \frac{1}{V'_g}) + (3/8)P'(V'_g - V'_{s,l})\} \quad (2.22)$$

and using the reduced equation of state for VDW fluid [87], the supersaturation formula is written as a function of the equilibrium pressure P_e, and the actual pressure P, and is approximated by [86]:

$$\Delta\mu(P,T) = kTln[P/P_e(T)] \quad (2.23)$$

The equilibrium pressure P_e has a significant influence in defining the direction of the phase first-order transition. From a metastable state to a new thermodynamically stable state, triggered by nucleation as the starting process of the transition. As a way of example, in Figure 2.9 the Gibbs free energy (expression (2.19)) of VDW fluid is plotted with respect to the reduced volume of the fluid V', known also as the volume for which the fluid is in stable thermodynamic equilibrium. The plot of the expression (2.19) is applied for a critical temperature $T' = 0.85$, three different pressures 0.470, 0505, and 0.550, and with an arbitrary reference energy $G_{ref} = 2MkT_{cr}$ [87]. The values of the Gibbs free energy at the two minima which correspond to the liquid and gas phases determine the direction and possibility of phase transitions taking place between the two phases. In the case that the values for a particular pressure are almost equal (green line at pressure 0.505) , no transition is possible and the two phases are coexisting in a stable equilibrium state μ_{equil}, while where there is a discrepancy between the gas and liquid values at minima (red line at pressure 0.540) a transition can be possible between the gas phase and liquid phase ($\mu_l > \mu_g$).

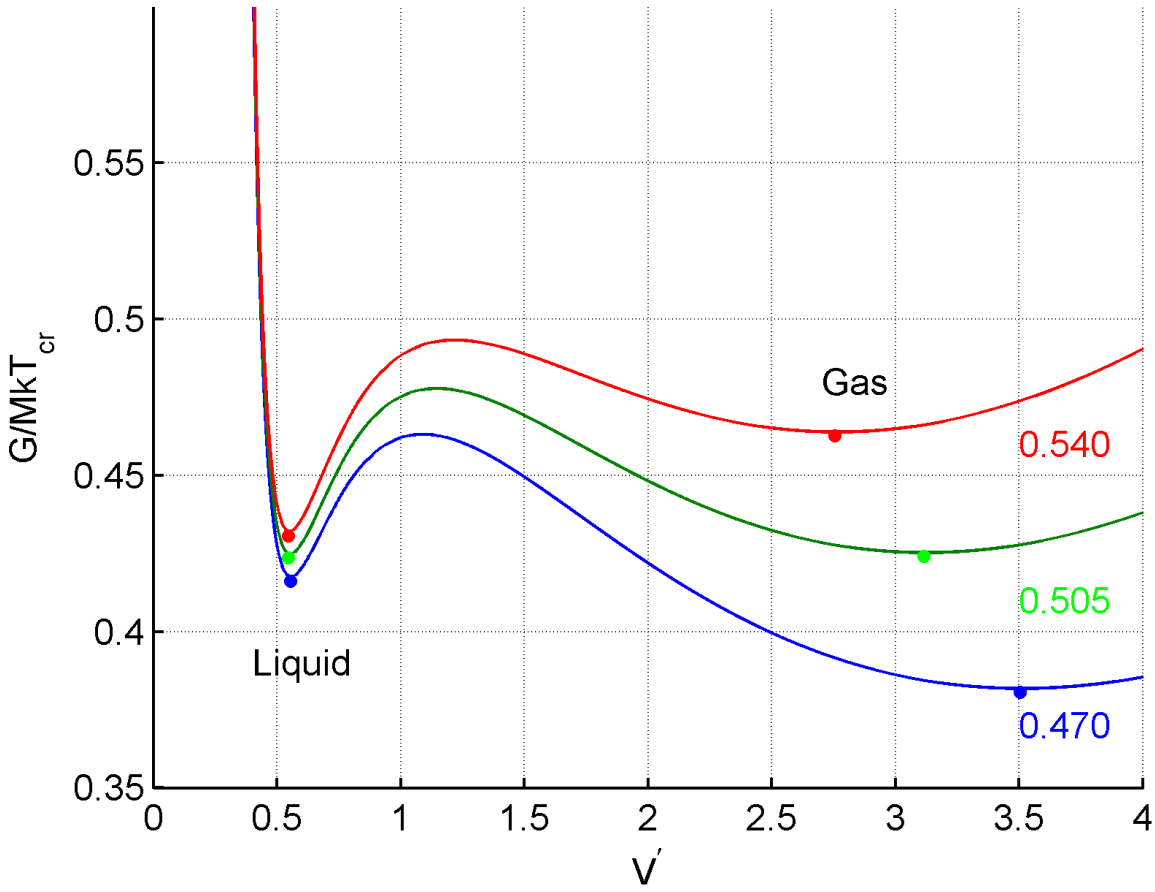

Figure 2.9: The Gibbs free energy (expression (2.19)) of VDW fluid on the reduced volume of the fluid at reduced pressures of 0.470, 0.505, 0.540 as labelled, and reduced temperature of 0.85. the bullets on the curves represent the G minima for the liquid, and gas phase.

Generally, this transition is mediated by a nucleation process in which the nanoscopic precursors of the new phase, or the embryos, are defined to be clusters of a few hundred or less of atoms or molecules. The classical nucleation theory is either homogenous (HON) or heterogeneous (HEN).

a. Homogenous nucleation

In this, the clusters are in direct contact with the phase parent only, and no different species are involved [88], as illustrated in Figure 2.10.

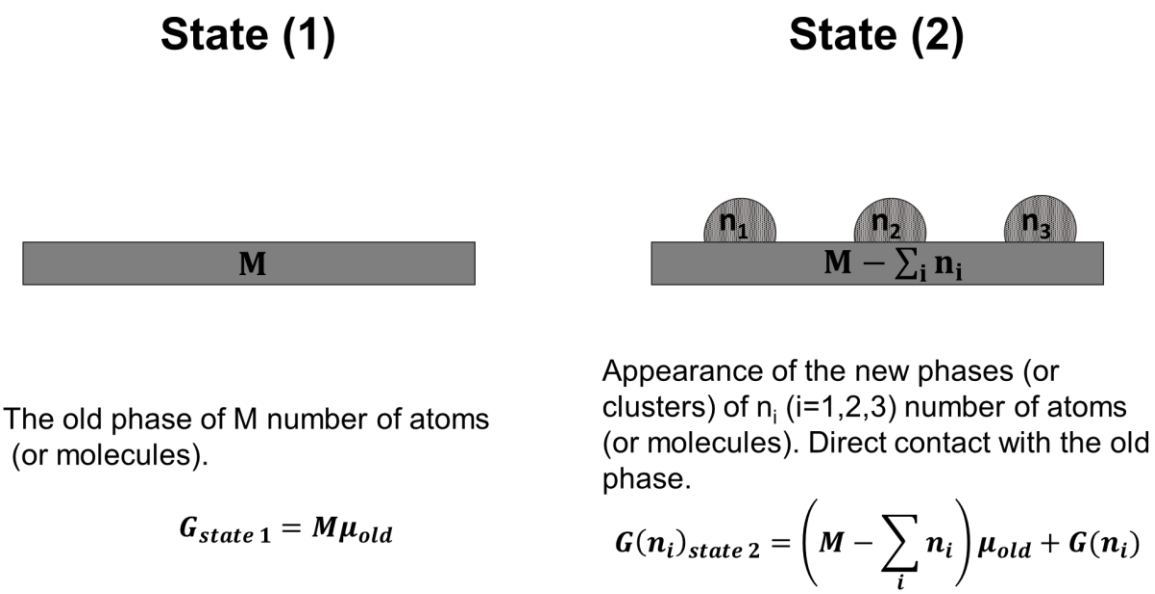

Figure 2.10: Illustration of homogenous nucleation (HON). State (1), and (2) describe the two phases before and after nucleation, with the expression of the Gibbs free energy for each phase.

Figure 2.10 describes in a simple way the two states before and after a HON is displayed. State (1) is the initial or parent phase, with the Gibbs free energy $G_{state\,1}$. State (2) is the phase after the nucleation and the start of clusters creation. The Gibbs free energy $G(n_i)_{state\,2}$ is a function of the Gibbs free energy of the old phase and the size of the clusters n_i, with $G(n_i)$ being the Gibbs free energy of the created clusters of n atoms (or molecules).

b. Heterogeneous nucleation

The nucleation is considered heterogeneous when the old phase contains foreign molecules or species such as particles, droplets, and bubbles, or it is in contact with different phases (growth on substrate) [88]. The appearance of the new phase clusters is more likely on the surfaces of those foreign species (Figure 2.11), making the HEN more abundant than HON in nature. For the calculation of the Gibbs free energy, the same HON formalism is followed, including G_s as the Gibbs free energy of the substrate, and $\Phi_{s,0}$ and $\Phi_s(n_i)$ representing the total energy of the substrate before and after nucleation is manifested [88].

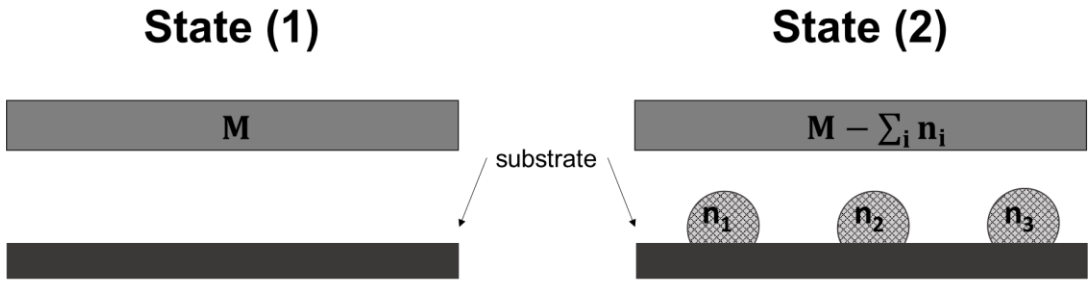

The old phase of M number of atoms (or molecules), and the substrate.

$$G_{state\,1} = M\mu_{old} + G_s + \Phi_{s,0}$$

Appearance of heterogeneous clusters of n_i (i=1,2,3) number of atoms (or molecules) on the substrate.

$$G(n_i)_{state\,2} = \left(M - \sum_i n_i\right)\mu_{old} + G(n_i) + G_s + \Phi_s(n_i)$$

Figure 2.11: HEN illustration before (State (1)) and after (State (2)) nucleation, and the corresponding Gibbs free energy corresponding to each state.

The nucleation takes place either in the three dimensions, like cap-shaped or lens-shaped clusters, or in two dimensions, like a disc-shaped cluster, [88]. In the present work, the nucleation is three dimensional of the form of condensed cap-shaped clusters (solid or liquid clusters) only.

Figure 2.12 represents an island of a spherical shape grown on a substrate surface. R and h symbolise the radius of the circular contact line and the height where the cap comes across to the substrate surface. θ is the angle located between the substrate surface and the tangent plane to the external surface of the cluster. The volume V_{cl} and the area A of the formed cluster of n molecules are expressed in function of the parameters R and θ in (2.24) [89].

$$V_{cl} = \frac{\pi R^3}{3}\frac{2+\cos\theta}{1+\cos\theta} + \frac{1-\cos\theta}{\sin\theta}, \qquad A = \frac{2\pi R^2}{1+\cos\theta}. \tag{2.24}$$

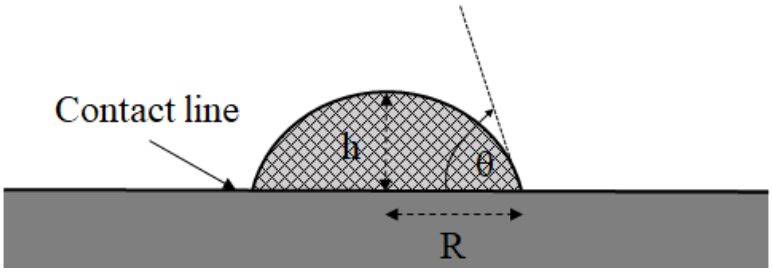

Figure 2.12: Schematic of a cap-shaped cluster of n molecules on the surface of a substrate. The contact line of the cluster with the surface is a circle of a radius R, and θ is the angle in between the tangent plane to the cluster and the substrate surface [89].

The calculation of the supersaturation is important in order to determine the phase transition, the possibility of nucleation taking place and to estimate the work W_{cl} for the formation of an n-sized stable clusters [88]. For the case of a condensed cluster formed by HEN, the work achieved in the formation of a stable cluster of n molecules is given by [88]:

$$W_{cl}(R) = \psi(\theta)\left[-\left(\frac{4\pi\Delta\mu}{3\nu_0}\right)R^3 + 4\pi\sigma R^2\right] \tag{2.25}$$

with $\psi(\theta) = (1/4)(2 + cos\,\theta\,)\,(1 - cos\,\theta\,)^2$, while θ is the wetting angle (Figure 2.12), deduced from the Young's equation describing the wetting angle of a droplet on a solid surface [88], [89]. ν_0, and σ are the volume occupied by one molecule within the cluster, and the specific surface energy of the formed cluster on the surface [88].

In the nucleation process, the nucleus is considered as the embryo of the created n-sized cluster. Hence, only nuclei with size and radius above a critical value can participate in the growth of the cluster [90]. Therefore, It makes it essential to determine the critical size n^*_{nuc}, and the critical radius R^*_{nuc} of the nuclei, and also to know the energy needed for the formation of stable critical nuclei W^*_{nuc}. The expressions of the work W^*_{nuc}, the critical size $\mathrm{n}^*_{\mathrm{nuc}}$, and radius $\mathrm{R}^*_{\mathrm{nuc}}$ of a spherical nucleus with respect to $\Delta\mu$, σ, and ν_0, of a spherical condensed cluster, are reduced to [90],

$$W_{nuc}^{*} = \psi(\theta)16\pi v_0^2\sigma^3/3\Delta\mu^2, \quad (2.26)$$

$$n_{nuc}^{*} = \psi(\theta)32\pi v_0^2\sigma^3/3\Delta\mu^3, \quad (2.27)$$

$$R_{nuc}^{*} = 2v_0\sigma/\Delta\mu. \quad (2.28)$$

2.5 Chemical vapour deposition

Chemical vapour deposition (CVD) is a controllable method of nanomaterials fabrication. The process involves the transport of a precursor to a reactor, and the generated vapour is deposited in solid form, such as a powder or on a substrate.

The CVD method offers the possibility of nanomaterials synthesis under different operating pressures (vacuum, atmospheric, low, and high pressure), as well as the use of precursor of gas (gas phase CVD), liquid (liquid injection CVD), or solid (sublimation CVD) forms.

The CVD is well-known of its success in the synthesis of carbon nanomaterials such a fullerene, graphene, carbon nanotubes and nanospheres. For this purpose, a precursor of carbon source, mostly hydrocarbon (C_2H_2, CH_4, C_2H_4, etc.) or CO is introduced in a quartz tube (reactor), which is a priori placed in a programmable furnace. The decomposition of the precursor is carried at atmospheric pressure, and the reaction may involve the addition of a catalyst, such as metals (catalytic CVD). The role of the catalyst is not primary during the synthesis process, but it modifies the structure and properties of the formed carbon nanomaterials. In the case of the absence of the catalyst, the method is reported as non-catalytic CVD.

The size, structure, shape, and the yield of the synthesised carbon nanomaterials depend on multiple parameters, such as the temperature, flow of the gas precursor in the

reactor, and the deposition time. Also, the orientation of the reactor (vertical or horizontal) in use has influence on the formed carbon nanomaterials. For example, with the use of a horizontal reactor, the synthesis of carbon spheres demands long deposition time (15 to 60 min) at high temperatures, while the use of a vertical reactor the reaction time is about a few minutes.

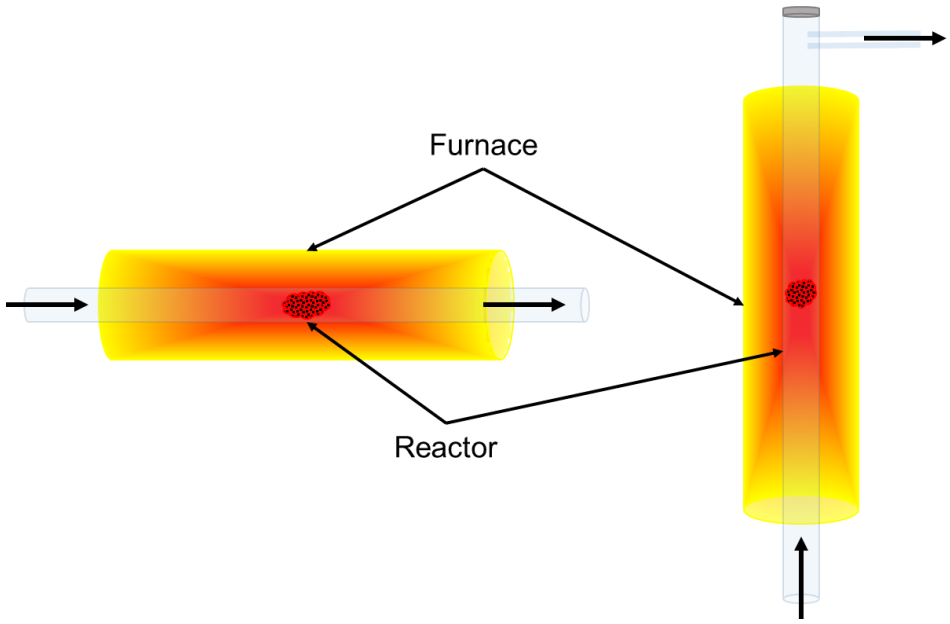

Figure 2.13: Horizontal and vertical CVD systems. The arrows show the gas in and outlet.

CHAPTER III

3 SYNTHESIS PROCEDURES AND LASER CHARACTERISATION METHODS

3.1 The Nanosecond Excimer Laser System

The experimental setup used in the present work was originally a Pulsed Laser Deposition (PLD) system which was modified for material ablation. The converted PLD system comprised of a nanosecond pulsed laser, as the main component, and a vacuum chamber. The excimer laser used was a Lambda Physik EMG with a Magnetic Switch Control (MSC) 103.

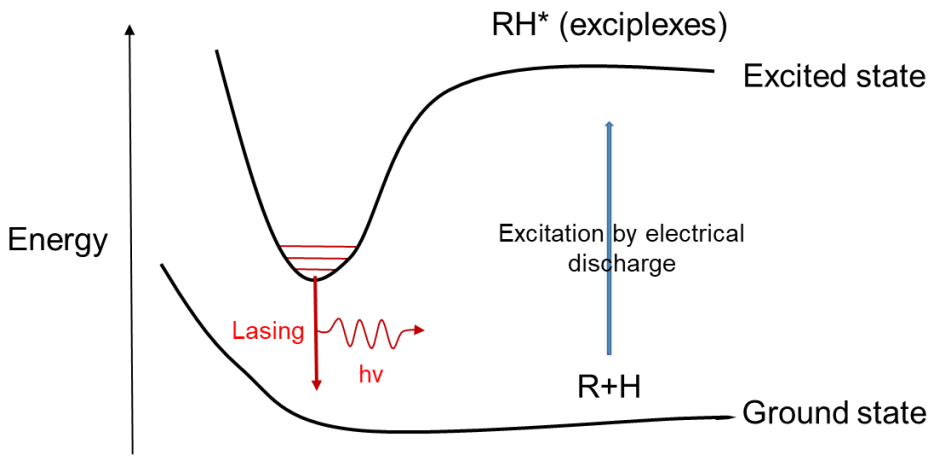

Figure 3.1: Schematic of the excited and ground electronic states in an excimer laser. R and H denote respectively the halide and rare atoms involved in the process of laser emission.

Excimer is a short term for excited dimer and is commonly used to refer to the class of lasers based on halides of noble gases (ArF (193 nm), KrF (248 nm), XeF (351 nm), and XeCl (308 nm)) [91]. The excimer laser is popular for UV light emission for a short time (usually of the order of a few nanoseconds) [92]. The gas mixture of noble (Ar, Kr, and Xe), halide (Cl and F), and buffer (Neon) gases is excited by an electric discharge

which leads to the formation of the excited complexes (exciplexes), also mentioned as RH* molecules, which represent the rare (R) and Halide (H) atoms [93]. Then, a laser transition between the excited (exciplexes RH*) and the ground (R+H) states of the excimer occurs due to the short lifetime of the RH* molecules.

In this thesis, the investigations were carried using a commercially available XeCl excimer laser, lazing at 308 nm [94]. The choice of the UV wavelength in this work was based on the need for higher energy photons rather than the ones generated from the IR or the visible radiations. In addition, the UV radiation is highly absorbed by metals as discussed in section 2 (Figure 2.2) [45]. The laser pulse width and the repetition rate of a Lambda Physik lasers depend on the gaseous mixture (ex ArF, KrCl…) and the type of the Magnetic Switch Control (MSC) used. According to the specifications from the manufacturer [94], the XeCl Excimer Lambda Physik Pulsed laser EMG 103 MSC emits a light pulse for a duration of 17 nanoseconds with a maximum repetition rate of 200 Hz. The highest available laser pulse rate used in this work was 7 Hz. This frequency limit was imposed by the lifetime excess of the thyratron, one of the most important components of the excimer laser technology [94]. The laser beam output has a rectangular shape of 10 × 22 mm^2 (Figure 3.2). For a stable beam profile and shape, a metallic circular pinhole of 5 mm diameter was used to reshape the laser beam.

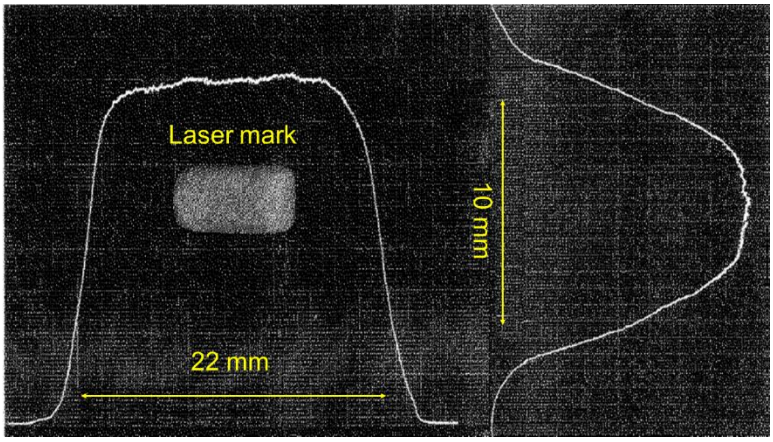

Figure 3.2: Laser beam profile on x and y axes and laser mark taken at 20 cm distance [94].

The laser beam characteristics are of primary importance as they determine the interaction between the impinging photons and the material surface. Energy and power density related characteristics as well as beam intensity, beam profile and pulsed beam time-structure (repetition rate and pulse width) characteristics are crucial in this respect.

3.2 Experimental System

The samples used in this work, namely Highly Oriented Pyrolytic Graphite (HOPG), was mounted on an “L” shaped metallic sample holder. The sample holder was placed inside a stainless steel vacuum chamber. The HOPG was sourced from a commercial manufacturer (SPI supplies). The HOPG is of high purity with a mosaic angle as small as 0.8° +/- 0.2°. The density and the thermal conductivity along the basal plane are 2.27 $g.cm^{-3}$ and 1800 $W.K^{-1}$ respectively.

The light pulses were focused onto the irradiated surface by a system of external optics comprising a converging UV lens of focal length of 300 mm. The lens was placed in front of the PLA vacuum chamber onto its viewport. The attenuation by the glass window was measured in order to know precisely the energy density of the laser deposited on the irradiated spot. The applied fluences were 1, 2, 5, and 9 $J.cm^{-2}$ at a constant laser energy of 2 mJ. In this geometry, a two-axis precision translation stage was used to translate the converging UV lens forwards and backwards and vary its focal distance with respect to the HOPG crystal located inside the chamber. This arrangement allows for selectivity of the required energy densities/fluences. The irradiations took place in a background gas of hydrogen.

The precise energy deposited onto the sample was established after taking into account the attenuation through the glass window of the chamber. This was established by measuring the incident and transmitted laser powers at the vacuum chamber with the help of a Field Master GS optical power metre. For a measured laser energy density of

3.5 J.cm^{-2} outside the chamber the attenuation inside the chamber was found to be 2.2 J.cm^{-2}.

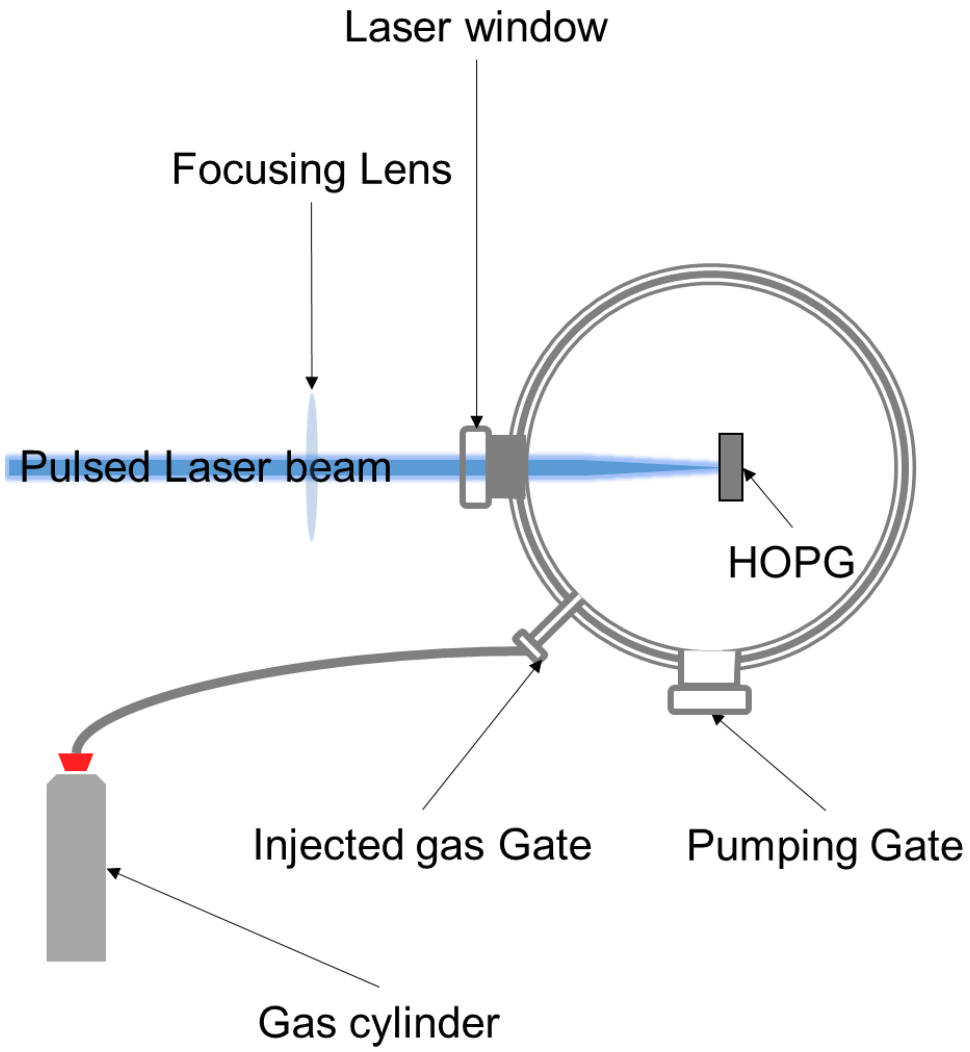

Figure 3.3: Representative diagram of the pulsed laser ablation (PLA) system.

A vacuum pressure of 10^{-2} Torr inside the chamber was reached using a rotary roughing pump and subsequent to that, a pressure of 10^{-8} Torr was reached by using a water cooled diffusion pump. The chamber was bled with gaseous mixture of either 4% Hydrogen and Argon or methane with different flow rates (standard cm^3/ min: sccm) monitored by a mass flow controller. The injection of the working gasses took place only once the pressure inside the chamber was within 10^{-5} Torr.

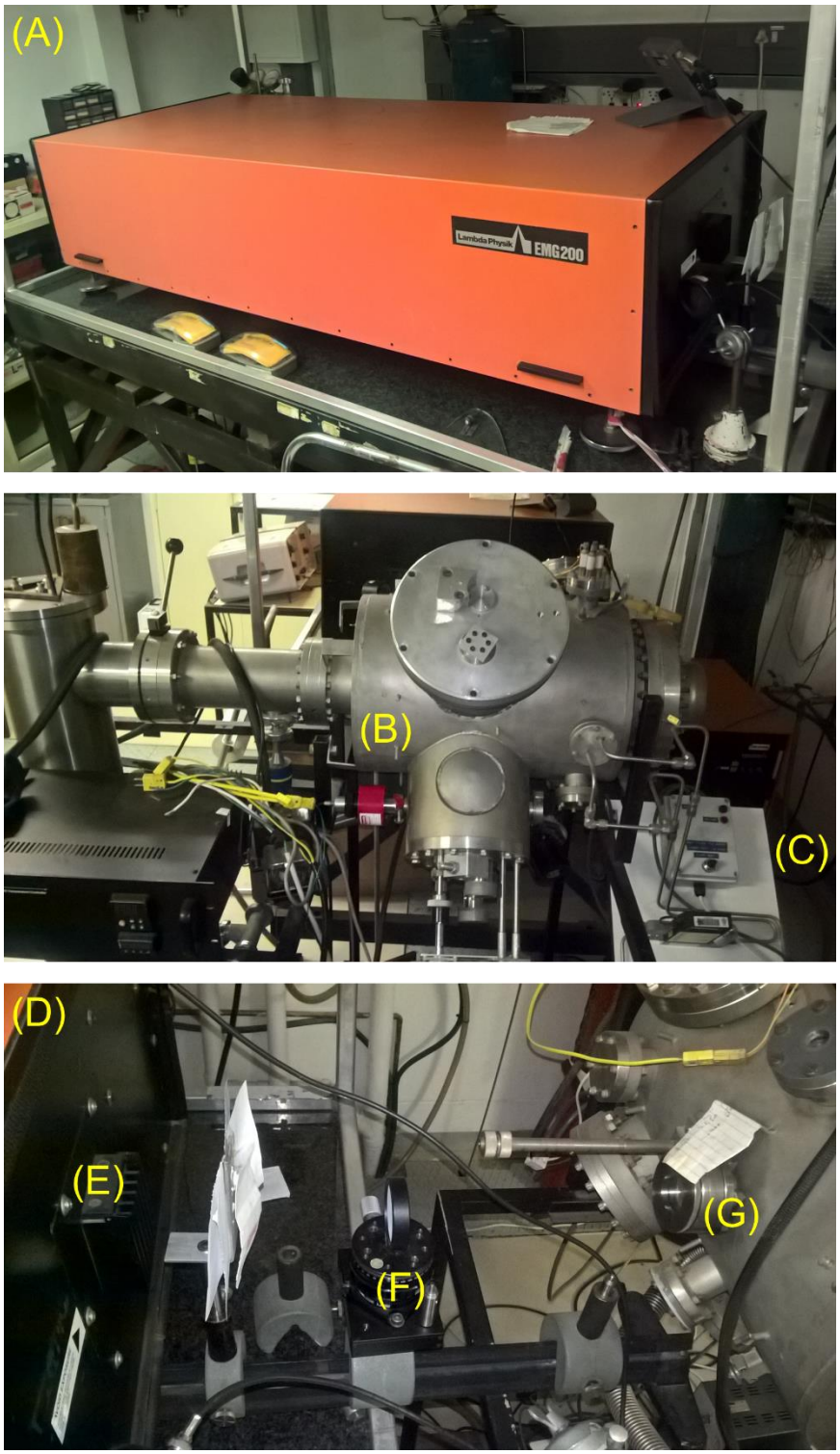

Figure 3.4: Photograph of the pulsed laser ablation system principal components. (A) the nanosecond pulsed laser, (B) the vacuum chamber, and (C) the gas flow controller. (D) shows the laser pulse path; from the laser box (left, (E): laser beam shutter) to the vacuum chamber (right) by the glass window (G), as it gets focused by the UV lens (F).

3.3 Laser Beam Characterisation

The profile distribution of the laser beam is described by a cylindrically symmetric Gaussian according to the expression,

$$I(r) = I_0 \, e^{-\frac{r^2}{w^2}}, \tag{3.1}$$

where I_0 is the energy flux per unit area, or simply the irradiance on-axis (at r = 0), and w is the beam radius.

The measurement of the diameter of a laser beam, r, poses a challenge in laser diagnostics. The irregularities of the beam intensity profile and the difficulties in defining the fine edges of some beam profiles are among the main problems encountered. A couple of methods have been, developed over the years. In this work, two different techniques were used to determine the laser beam waist; the knife-edge [95] and the wire method [96].

a. Knife-edge method

In this, a razor-blade is operated by a micrometre stage and is translated along the y-direction, obscuring the power metre detector. The y-position for which the razor-blade covers the laser beam completely is considered as the origin (0,0) for a 2D plane. The razer-blade is continuously translated along the y-axis in 100 microns steps, while simultaneously recording the laser power at each step until the laser beam is fully exposed. The measured laser beam power fraction as a function of the razor-blade position is shown in Figure 3.5.

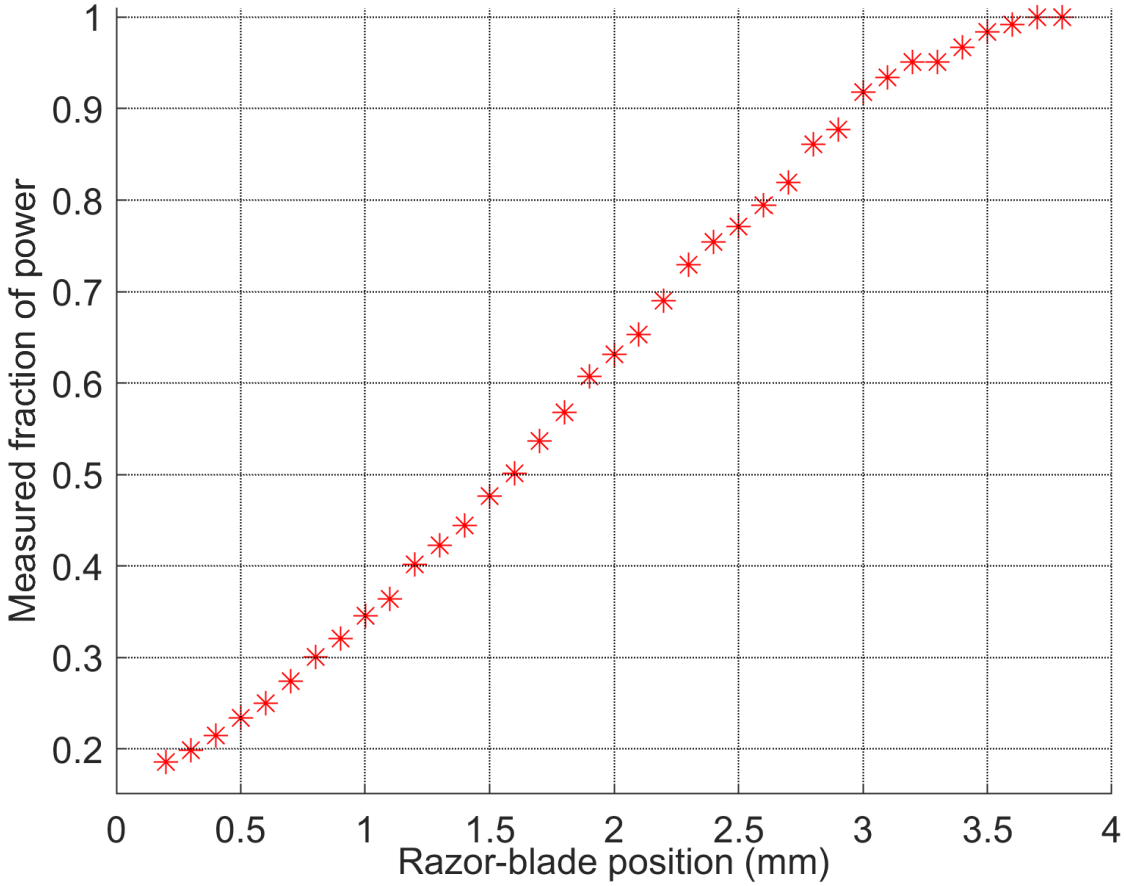

Figure 3.5: The razor-blade position and its related power fraction measurements using the knife-edge method.

For a Gaussian laser beam propagating in the z-direction, and passing via a razor-blade translating in the y-direction, the fraction of the laser power output is calculated by

$$\Phi(Y) = \frac{\Phi_0}{2}(1 - \mathrm{erf}(\sqrt{2}\frac{Y}{w_0})) \tag{3.2}$$

with Φ_0, and $\Phi(Y)$ being the total power and power output of the razor-blade at the position Y, and w_0 is the beam radius at $1/e^2$.

The razor blade positions at 10 and 90 % of the laser power output are commonly used to calculate the laser beam radius. However, due to the power meter inability to detect low powers accurately, the calculations were carried out at 20-80 % fractions of

the laser output. Therefore, the expression above for $\Phi(Y_{20}) = 0.2 \text{ x } \Phi_0$ for razor blade position Y_{20}, becomes

$$0.2 = \frac{1}{2}(1 - \text{erf}(\sqrt{2}\frac{Y_{20}}{w_0})) \tag{3.3}$$

$$\text{erf}\left(\sqrt{2}\frac{Y_{20}}{w_0}\right) = 0.6 \tag{3.4}$$

The Gaussian probability distribution is

$$P(t_{20}) = \frac{1}{2} + \frac{1}{2}\text{erf}\left(\frac{t_{20}}{\sqrt{2}}\right) \tag{3.5}$$

which, using the above error function, becomes

$$P(t_{20}) = 0.8, \quad \text{as } \frac{t_{20}}{\sqrt{2}} = \frac{\sqrt{2}Y_{20}}{w_0} \tag{3.6}$$

By using the standard probability distribution table [97], the t_{20} value was deduced and found to be equal to 0.85. Hence, the beam radius w_0 was obtained.

$$Y_{20} = 0.425\, w_0,\ t_{20} = 0.85 \tag{3.7}$$

Considering the symmetry of the Gaussian beam profile, the distance difference between the points where the transmitted power is 20% and 80% ($Y_{20\text{-}80}$) is two times larger than Y_{20}, and the beam radius w_0 is calculated to be 2.70 mm.

$$w_0 = \frac{Y_{20-80}}{2 \times 0.425} = 2.70\ mm,\ \ Y_{20-80} = 2.6 - 0.3 \tag{3.8}$$

Similar calculations were applied for Y_{25} and Y_{75}, and the beam radius w_0 at $1/e^2$ was found to be 2.64 mm. This second calculation confirms the result obtained for the case of $Y_{20\text{-}80}$ and helps to converge to an average beam radius value.

$$w_0 = \frac{Y_{25-75}}{2 \times 0.34} = 2.64\, mm, \;\; Y_{25-75} = 2.4 - 0.6 \tag{3.9}$$

b. Wire method

This new simple method is based on the use of a cylindrical object which acts as an obstacle to partially block the beam while measuring the fraction of the power transmitted with the help of a power metre [96].

A wire with a diameter of 2.1 mm was used as a beam obstacle, which was mounted on a micrometre stage, blocking horizontally a Gaussian beam propagating along the z-direction. The diameter of the cylindrical object is an important parameter for the calculation of beam radius. If the wire diameter is too small ($D_{wire} << 2w_0$), the recorded transmission is too large, resulting in inferior precision in measuring the beam radius. On the other hand, when the wire diameter is too large ($D_{wire} \geq 2w_0$), the estimate of the wings of the Gaussian beam is difficult [96]. To conclude, it is crucial to choose the diameter of the cylindrical obstacle carefully.

In our case, the wire obstacle was carefully placed over the centre of the laser beam by using a micro-mete stage holding the wire which was displaced by a few microns up and down. The minimum transmission measured in this way, corresponds to the wire been placed at the centre of the Gaussian beam profile, where it cuts off maximum part of the beam. The minimum transmission for each wire position was measured many times and an average power P_{avr} established for each translation. Table 3.1 shows the average power P_{avr}, T_{trans} represents the fraction of the minimum transmission to the total laser power, and the deduced beam radius w_0 from the formula below [96].

$$w_0 = \frac{D_{wire}}{\sqrt{2}\,\mathrm{erf}^{-1}(1 - T_{min})} \tag{3.10}$$

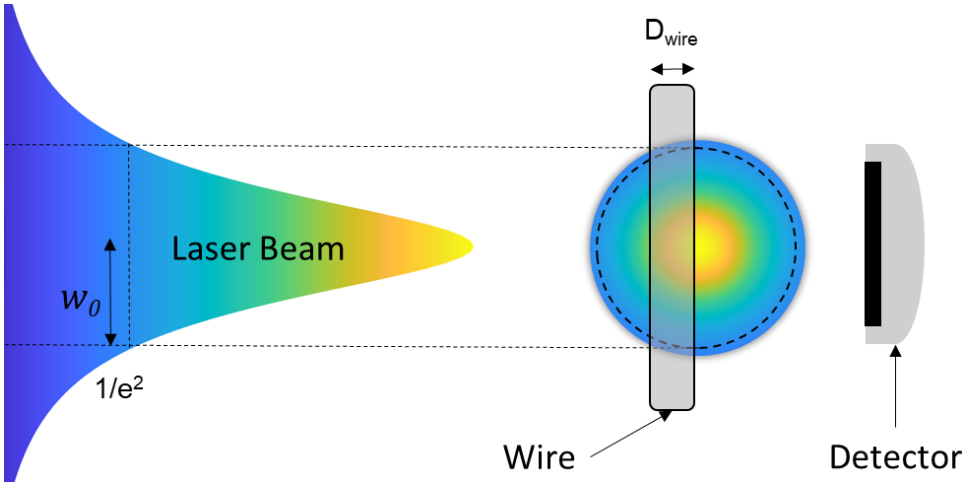

Figure 3.6: Schematic representation of the wire method setup, which consists of the laser beam whose radius w_0 has to be established, the wire of diameter D_{wire}, and a detector to record the power of the laser after propagating through the wire.

Table 3.1: The transmission T_{trans} for a total power P_{tot} of 11.3 mW, and the related calculated beam radius w_0.

P_{avr} (mW)	$T_{trans}=P_{avr}/P_{tot}$ (%)	w_0 (mm)
4.9050	43.41	2.68
4.9100	43.45	2.68
5.1250	45.35	2.80
5.2500	46.46	2.87
5.2600	46.55	2.87
5.2400	46.37	2.86
5.3400	47.26	2.92
5.3600	47.43	2.93
5.4250	48.01	2.97
5.4250	48.01	2.97
5.2500	46.46	2.87

According to the mathematical description given by Mylonakis *et al.,* the radius of the beam corresponds to the minimum transmitted laser intensity attributed to the placement of the wire at the centre of the Gaussian Profile. Therefore, from the above measurements, the value of w_o = 2.68 mm represents a realistic beam radius estimate at $1/e^2$.

The two values of the beam radius at $1/e^2$ obtained by the knife-edge (2.70 mm) and the wire method (2.68 mm) differ by less than 1%. This is a realistic estimate of the beam radius considering that the initial laser beam was reshaped by a circular metallic slit of 2.5 mm radius.

3.3.1 Calculation of the energy densities of the beam

The energy densities ($J.cm^{-2}$) used in this work were selected by keeping the energy of the laser constant and varying the size of the laser spot on the sample. This was achieved by simply changing the focal distance of a UV lens, of 300 mm focal length f, mounted on a translation stage. The focal spot size was deduced from the calculated beam waist by the expression

$$\omega^2(R) = \left(\frac{\lambda}{\omega_R \pi}\right)^2 R^2 + \left(1 - \frac{R}{f}\right)^2 \omega_R^2 \tag{3.11}$$

where R is the distance between the lens and the sample, and $\omega(R)$ is the beam waist at position R. λ is the laser wavelength, and ω_R is the laser beam radius before focus as calculated in section 3.3. The beam waist at the focal length of the UV lens (for $f = 300\ mm$) was calculated to be $\omega_0 = 10.97.10^{-3}$ mm.

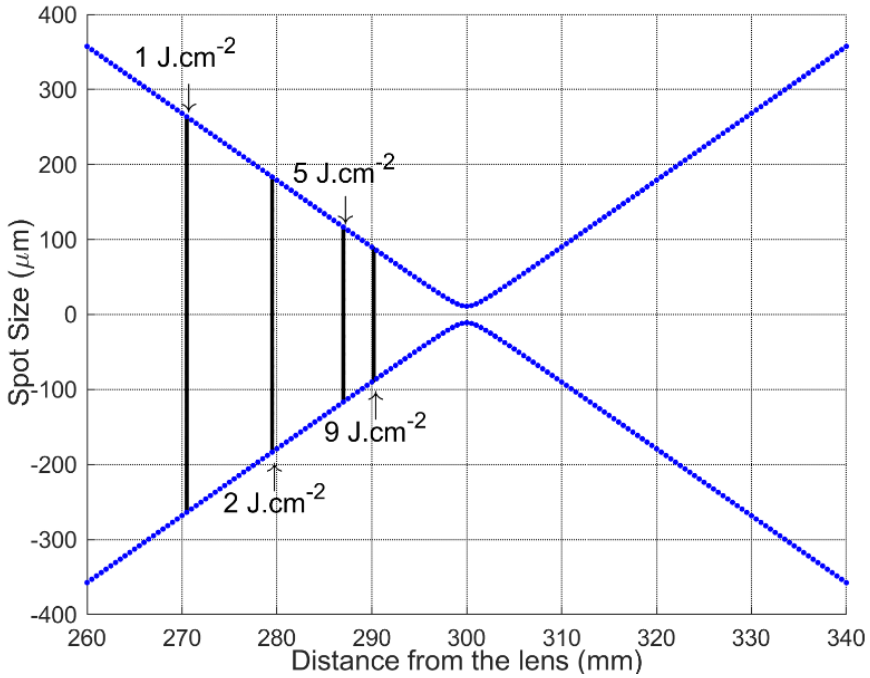

Figure 3.7: Laser beam propagation as a function of the focal length (300 mm). The solid black lines represent the position away from the lens, where the sample was placed in, as varied energy densities were applied depending on laser beam waist manipulation. At R = 300 mm (focal length), ω_0 is $10.97.10^{-3}\ mm$.

The laser beam optical envelope is shown in Figure 3.7 after passing through the lens, converging to the focal point at $f = 300\ mm$ inside the chamber. The arrows point out to the distances R between the sample and the lens with the corresponding required energy densities (1, 2, 5, and 9 J.cm^{-2}). The black lines represent the beam spots sizes corresponding to these selected fluences. The power density distribution of the beam with respect to the Rayleigh range $Z = 0$ is also shown in Figure 3.8 as calculated by

$$I(z) = I_o \left(\frac{\omega_0}{\omega(z)}\right)^2, \tag{3.12}$$

with,

$$\omega(z) = \omega_0 \left[1 + \left(\frac{z}{z_0}\right)^2\right]^{\frac{1}{2}} \tag{3.13}$$

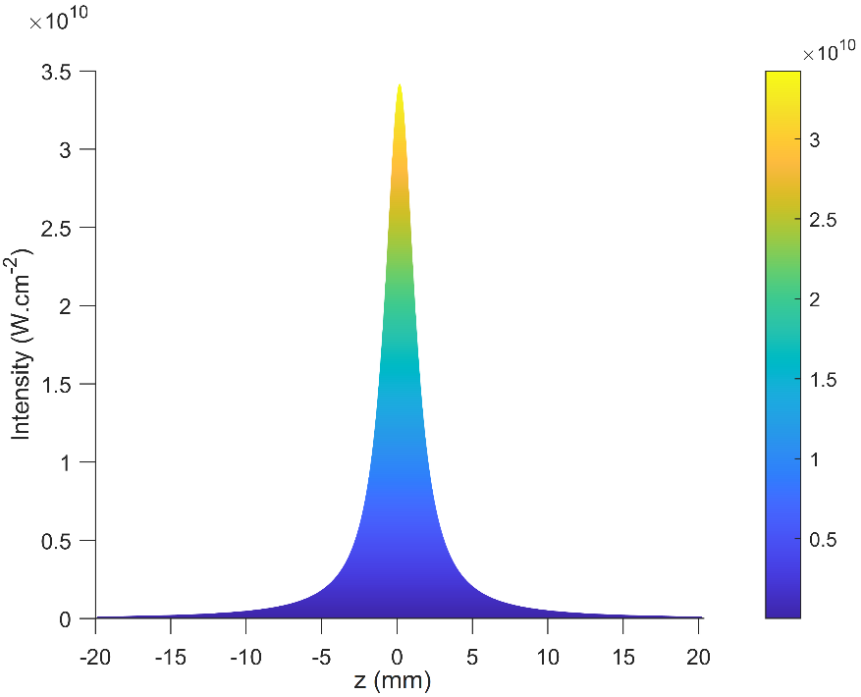

Figure 3.8: The graph represents the power density (energy density/pulse width) in W.cm^{-2} as a function of the propagation parameter *z*.

Laser interactions with the surface of Highly Oriented Pyrolytic Graphite (HOPG) and the resulting phase transitions and surface damage has been the main focus of the present study. HOPG samples have been irradiated using pulsed lasers in Hydrogen-Argon (4% of hydrogen) ambient atmosphere. The laser induced effects on the surface were studied as a function of the pulsed laser parameters such as:

- the energy density (J.cm^{-2}),
- the number of pulses, and
- the repetition rate (Hz), as well as the gas flow rate inside the chamber.

This elaborate effort was undertaken in order to obtain the optimum set of conditions for creating the desired nano-defects as well as to obtain a better understanding and insight of the physical processes and mechanisms involved in the formation and the growth of the micro and the nanostructures observed within and around the irradiated areas.

3.3.2 Laser irradiation of HOPG with diverse energy densities

Preliminary laser irradiations on the surface of HOPG at atmospheric pressure and room temperature indicated the existence of a fluence threshold, at which visible morphological changes on the surface emerge. The experiments have established the parameter window for the nanostructure formation to be in the range between 1 and 10 $J.cm^{-2}$. Subsequently, a background gas mixture of 4% of hydrogen and Ar was introduced during irradiations within this range of energy densities. The flow rate of the gas in the chamber (15 sccm), the number of pulses applied (1000 pulses) and the repetition rate of the laser (5 Hz) were initially kept constant during the irradiation of the HOPG surface using different energy densities as shown in Table 3.2.

Table 3.2: HOPG irradiations with the various fluences used.

Parameters	**H_2 Flow rate = 15 sccm, number of pulses = 1000, repetition rate = 5 Hz**			
Fluence ($J.cm^{-2}$)	1	2	5	9

3.3.3 Laser irradiation of HOPG with different gas environment / conditions

It is well known that the growth of nanomaterials using different synthesis methods such as CVD and PLD is greatly assisted when background gasses, such as inert argon or nitrogen, are introduced [98], [99]. The significant role that hydrogen concentration plays during different synthesis techniques of carbon-based nanomaterials cannot be overemphasised [100]. The hydrogen content is reported to control the morphology, structure, size, and quality during the synthesis process [101], [102]. It is demonstrated that the presence of the hydrogen is key for the formation of hydrocarbon radicals that favour and enhance the growth of carbon nanomaterials [103].

Therefore, possible phase transitions from a Highly Oriented Pyrolytic Graphite (HOPG) to a spherical nanostructured carbon during PLA in the presence of hydrogen as an active background gas, as well as methane, were investigated.

A summary, of the gas context conditions of HOPG ablations using both methane and hydrogen is shown in Table 3.3.

Table 3.3: Flow rates of the injected gas for different experiment runs.

Injected gas (sccm)	**Fluence = 2 J.cm^{-2}, number of pulses = 1000, repetition rate = 5 Hz**					
H_2/Ar	0	2	5	15	30	35
CH_4	0	2	5	10	-	-

3.3.4 Laser irradiation of HOPG with different number of pulses and repetition rates.

The number of pulses was part of the study related to the HOPG ablation. A series of irradiations was applied in the same way described before, with the number of pulses being the only parameter changed. The experiment runs were executed with different numbers of pulses, a constant fluence of 2 J.cm^{-2}, a flow rate of 15 sccm for the background gas containing H_2, and a repetition rate kept at 5 Hz. The applied numbers of pulses were 100, 500, 1000, and 10000 pulses. For the count of the number pulses, an electronic timer was used.

In addition, the effects of ablation were investigated with respect also to the repetition rate. For these sets of experiments, the excitation rates used were 2, 5, and 7 Hz as shown in Table 3.4

Table 3.4: Summary of the series experiments for the number of pulses and repetition rate study.

Parameters	**Fluence = 2 J.cm^{-2}, H_2 Flow rate = 15 sccm, repetition rate = 5 Hz**			
Number of pulses	100	500	1000	10000
	Fluence = 2 J.cm^{-2}, H_2 Flow rate = 15 sccm, number of pulses = 1000			
Repetition rate	2	5	7	

3.4 Carbon nanospheres synthesis by chemical vapour deposition

Chemical vapour deposition (CVD), arc-discharge, and laser ablation are the most commonly used techniques to synthesise carbon nanospheres.

In this research work, a non-catalytic horizontal CVD system was used in the synthesis of the carbon nanospheres. The synthesis system consisted of a quartz tube placed in a furnace, in which the temperature was controlled electronically. The synthesis with CVD consists of converting a heterogeneous volatile carbon source into a non-volatile solid material. For this work, the selected source of carbon was acetylene gas (C_2H_2).

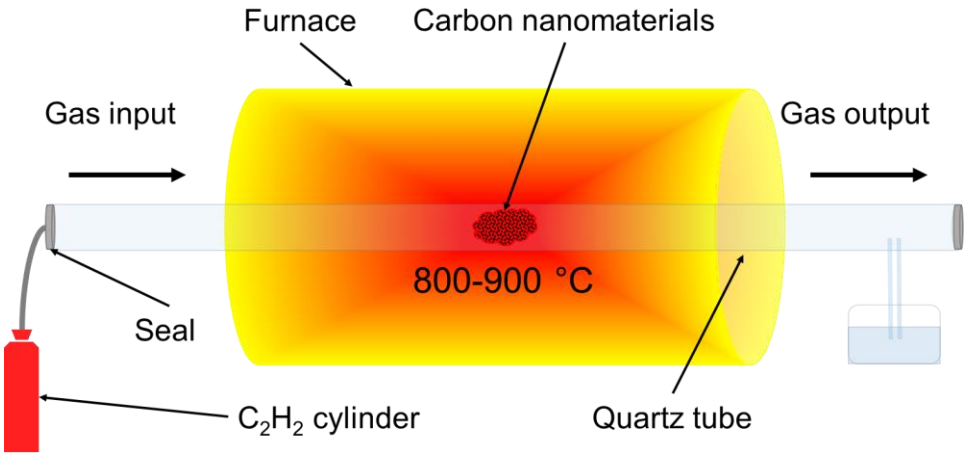

Figure 3.9: Diagram of the horizontal CVD system used in the synthesis of the carbon nanospheres.

The quartz reactor was placed in the furnace and the temperature set at 800-900 °C. Once, the required temperature was reached, the C_2H_2 gas was injected in the reactor at atmospheric pressure. The C_2H_2 gas is known to be toxic and explosive, so the input and output of the gas were sealed properly to prevent any leaks, and a water bubbler was placed to prevent the compression of the gas in the tube. The gas was left to flow in the quartz tube for a duration of time (20-40 min). After that the C_2H_2 flow was stopped and the furnace cooled to room temperature. Once the furnace cooled off, the formed solid powder from the process was collected, and placed in glass containers.

In this manner, two sets of carbon nanospheres were synthesised separately and were designated as “A” and “B”. The Scanning Electron Microscopy (SEM) images of Figure 3.10 illustrate the significant differences in the diameter of these two sample sets. Set “A” is characterised by a diameter of the order of ~200 nm while set “B” has a diameter of the order of 350 nm. It must be noted that one difference in the synthesis procedure between the two sets was the reaction time which was 20 min for set “A” and 40 min for set “B”.

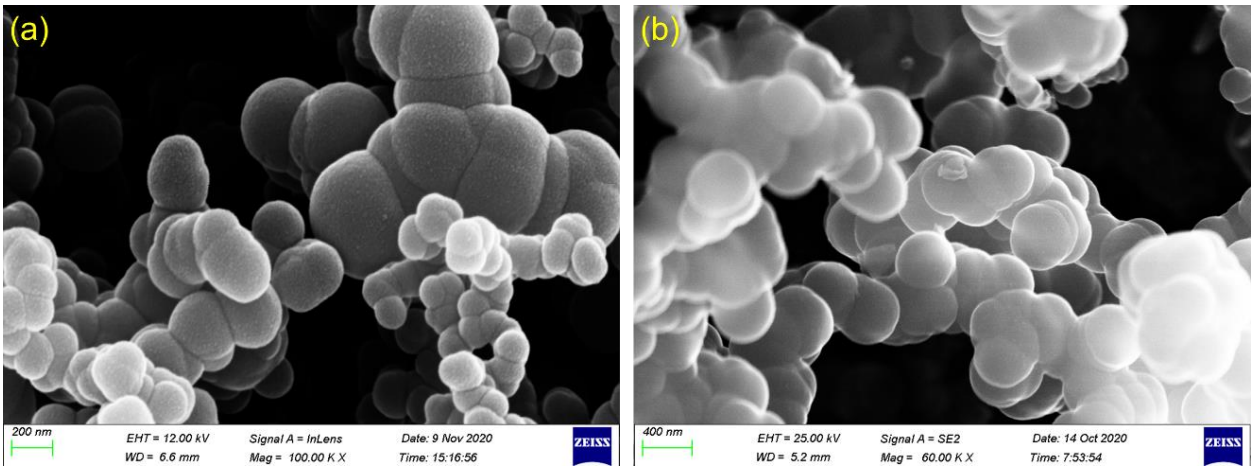

Figure 3.10: (a) and (b) are SEM images of synthesized carbon nanospheres by CVD collected from samples “A” and “B” respectively.

Chapter IV

4 CHARACTERIZATION METHODS

A number of different methods were used to characterize the ablated surfaces in a qualitative and quantitative manner. Raman spectroscopy was used to extract information with respect to molecular bonds and their vibrational modes, as well as for identification of possible formation of carbon allotropes. Scanning Electron Microscopy (SEM) was used to characterise the irradiated samples, in terms of nanoscale morphological imaging, structural modifications and nanostructures formation.

A state of the art Physical Properties Measurement System (Dynacool 12T PPMS) was used to explore possible phase transitions in the electronic and magnetic properties supplemented by the Mossbauer hyperfine technique.

4.1 Scanning Electron Microscopy

The use of electron instead of light in microscopic techniques permitted a major advance in the spatial resolution δ. As stated by the Rayleigh criterion (4.1), the spatial resolution of a microscope depends on the wavelength of the incoming probing particle, this being a photon or an electron (wave-particle). The spatial resolution for electron microscopy is limited by the wavelength of the electron beam used, as well as by the numerical aperture of the optics used and the electric conductivity of the sample [104].

$$\delta = 0.61\,\lambda/NA \tag{4.1}$$

The interaction of the accelerated electrons with the sample is a complicated and multifaceted process. As a result, secondary electron emission, atomic excitations and ionisation can occur. The result for these excitations is seen in the form of X-ray emission

due to electronic transitions or in the form of Auger electrons. The spectroscopic observation of these different emitted particles assists in a variety of information that can be attained in terms of 2D-imaging and trace element analysis. These secondary electrons are detected by electron detectors in coincidence with the electron beam rastering signal resulting in 2D-imaging of the sample. Figure 4.1 (a) is a schematic representation of the electron beam interaction with the surface and the processes that can take place.

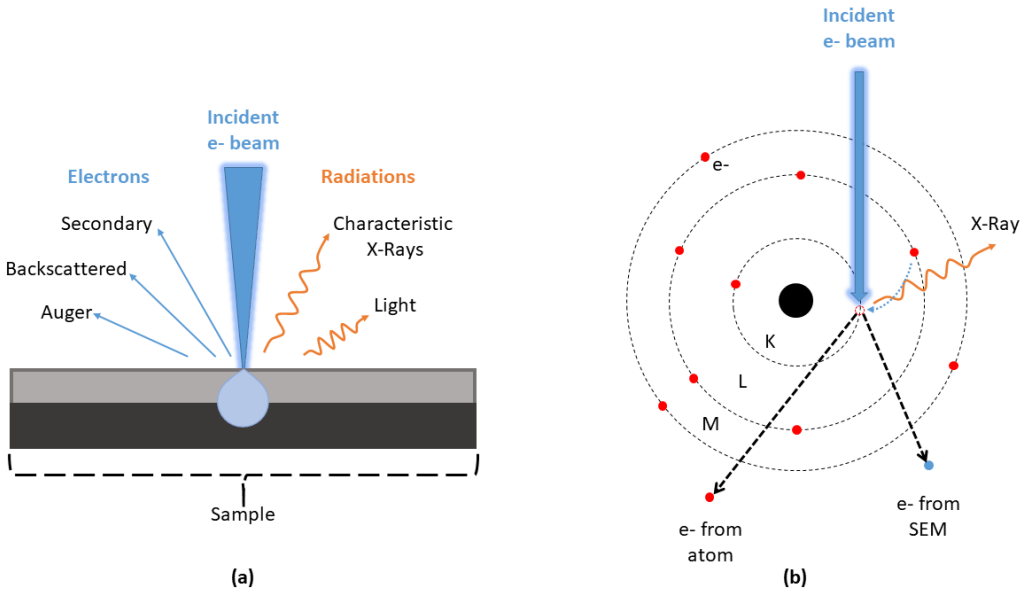

Figure 4.1: (a) Illustration of the different reflected signals after interaction of the e- beam with a sample. (b) Energy-Dispersive X-ray spectroscopy (EDX) process used for chemical characterization [104].

In this research work, a Nova 600 NanoLab Scanning Electron Microscope (SEM) was used for imaging and investigating the morphological modifications, the formed nanostructures, and their chemical composition within the irradiated spots, and the surrounding zones. The accelerating voltage is of the order of 30 kV which is sufficient for obtaining surface images at the nano-scale level. The interactions of these high energy electrons with the core electrons of the atoms at the surface and at a certain depth of the sample reveal information about the identity and the quantity of these atoms based on the X-ray emission from electronic transitions between different electronic orbitals. This

characterization technique, known as Energy-Dispersive X-ray spectroscopy (EDX) and its process is illustrated in Figure 4.1 (b) and was used in the present study.

4.2 Raman Spectroscopy

Raman spectroscopy is a standard non-destructive technique, suitable for characterization at ambient condition, with no sample preparation. This probing tool became widespread for its clear identification of crystalline, nanocrystalline, and amorphous carbon [105], as each structure of these carbon allotropes has a well-defined Raman signal. When a monochromatic light of $\hbar\omega_0$ energy strikes on a surface, two processes occur; elastic and inelastic scattering of the incoming light. The inelastic scattering known as Raman scattering is emitted with two different energies, $\hbar\omega_0 \pm \hbar\omega_s$, which correspond to the so-called Stokes (-) and anti-Stokes (+) lines [106]. Stokes radiation is associated with the lower energy and anti-Stokes radiation has greater energy. The energy difference is attributed to the vibrational energy levels in the ground electronic state of the molecule. Therefore, the observed Raman shift of the Stokes and anti-Stokes lines are a direct measure of the vibrational energies of the molecule.

The micro Raman system utilized for the characterization of the samples in this thesis makes use of an Argon ion laser performing excitation with green (514.5 nm) and UV (229 nm) light. The $Ar^{\pm}$ laser is used in conjunction with a Horiba Jobin-Yvon LabRAM HR Raman spectrometer. For focusing the laser beam onto the sample surface, a microscope attachment with 25X to 100X objective lens for visible and UV light was adapted to the Raman system. The backscattered light was dispersed via a 600 line/mm grating onto a liquid nitrogen-cooled charge-coupled device (CCD) detector. The system composed also of a micrometre motorized stage to manipulate the characterized specimen in the x, y, and z directions for line scans and mapping.

In this research, Raman spectroscopy was applied to establish the bonding type, domain size, and the structure of the laser irradiated sample. The analysis of the high and

low frequencies peaks, including their intensities, positions, and widths represent the major source of information in the Raman spectra. As for the better understanding of the structure and nanostructure of the samples, Raman spectra either as singles, or line scans were recorded, at the pulsed laser irradiated spots and extended to the surrounding zones. Spectra of virgin samples were recorded for comparison. The Raman spectra were collected for the same condition at a wavelength of 514 nm and a laser spot size of 1 μm to detect any changes in the structure. These unified conditions permit qualitative comparison, and minimise instrumental variations induced effects.

4.3 Physical Property Measurement Systems

The Physical Property Measurement System (PPMS) is a fully automated system which measure multiple physical properties of materials. The measurements of magnetic, mechanical, electronic, and thermal properties of bulk, thin film, and powder form are performed at low temperature and within a wide range of magnetic fields. These different measurement options are implemented by means of different sample holders and inserts.

The electrical and magnetic properties of the synthesised carbon nanospheres powders were measured by a Quantum Design Physical Property Measurement System (PPMS “DynaCool” 12T). The system offers the possibility to conduct measurements as a function of low-temperatures and precise magnetic fields for ranges of 1.8-400 K and 0-12 T respectively.

The magnetic properties were investigated by a DC-Vibrating Sample Magnetometer (VSM). In order to perform the measurements, a few milligrams (~12 mg) of the carbon powder was mounted in a polycarbonate capsule and placed in a holder of a low-background brass half-tube. Prior to any measurement, the centre position of the carbon powder in the capsule was set at 35 mm for optimum sample height at the coil set. The magnetic moment (μ) was measured in electromagnetic units (emu) as a function

of the magnetic field (Oe) at different temperature in (K). Field cooling (FC) and field warming (FW) mode measurements were acquired too.

The resistance and the magneto-resistance measurements were performed using the same PPMS system. The method consisted of a linear four-point probes system, in which a voltage was injected in the central probes and the current was measured from the sides. The probes were four Spring Loaded Contacts (SLC) in a single row plastic body, distancing each other by 2.54 mm. The electrical contact with the sample was by means of rounded tips mounted on springs. The rounded tips of 1.07 mm diameters allowed a large contact surface area, and the springs prevented damaging delicate and soft surfaces by applying uniform forces once the SLCs were in contact with the sample. The solder tails at the end of the SLCs facilitated the connections to the PPMS pad through gold plated wires.

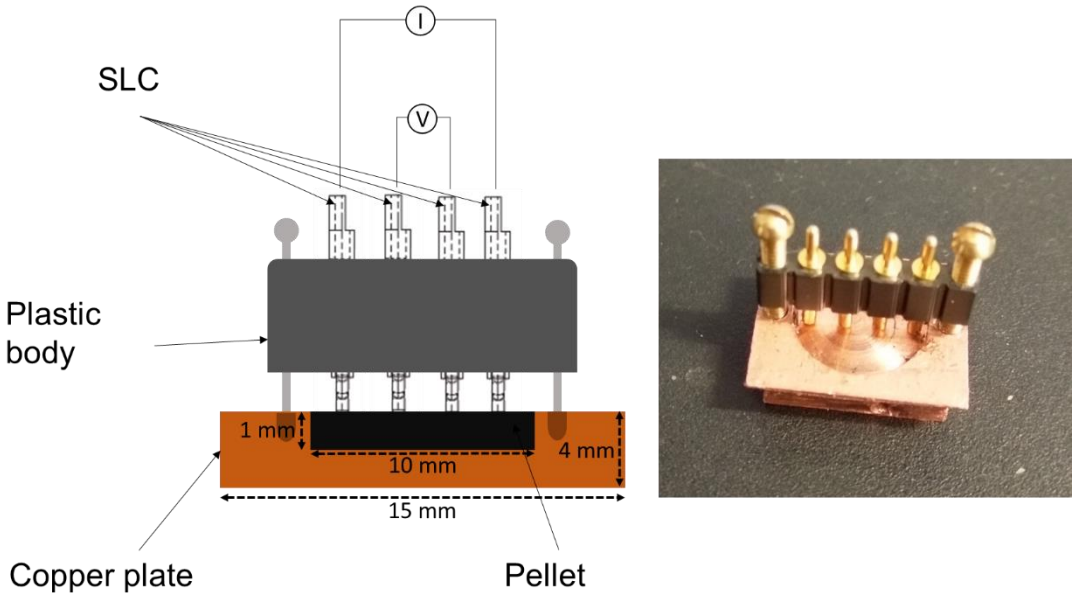

Figure 4.2: Sketch (left) and picture (right) of the system used for acquiring the electronic measurements with PPMS. The sketch shows the positioning of the Spring-Loaded Contacts (SLC) and the orientation of the applied voltage and the measured current within the SLCs.

For the measurements, a few milligrams of nano-carbon powder were pressed by a manual Parr press at 15 MPa for 15 minutes. The prepared nano-carbon pellet of a disc shape with a diameter and thickness of 10 mm and 1 mm respectively was placed on a sample holder. It is important to mention that the prepared pellet was based of carbon nanospheres only.

The pellet holder was made of copper with dimensions of 15×12×4 mm^3. On the top surface of the holder, a deep recession of 1 mm and a diameter of 10.2 mm was machined to assure the stability of the pellet while the measurements were collected. The SLCs centred vertically on the recession were secured on the holder by two screws located on the extremes of the plastic body, as seen in the picture of Figure 4.2.

4.4 Mössbauer spectroscopy

Mössbauer spectroscopy is an important technique in material sciences as it provides information regarding the chemical, structural and magnetic properties of materials. This technique is based on the Nobel prize winning Mössbauer effect, in which the recoil energy of the absorbed or emitted γ-ray by a nucleus is practically zero when the emitting and absorbing nuclei are in a solid matrix satisfying in this way a resonance condition.

The linewidth of the excited state of the isotope used, usually of the order of 10^{-9} eV depending on the lifetime of the given state, is the determining factor of the limiting resolution. The Mössbauer spectroscopy therefore uses and detects low excited lying states of selective isotopes of long lifetime and is practically limited to Fe, Ru, Sn, Sb, Te, I, W, Ir, Au, Eu, Gd, Dy, Er, Yb, Np. From all elements cited before, ^{57}Fe is considered as the most used isotope element in Mössbauer spectroscopy due to its very low energy γ-ray (14.4 keV) and long-lived excited state.

The environment of the Mössbauer probe-nuclei in a material affects the hyperfine splitting and changes the energies of the nuclear transition by billionths of an electron volt. In order to detect this and achieve resonance condition, the energy of the probing gamma-rays has to change in a minute way. This is achieved by slightly changing the energy using the Doppler effect by oscillating a radioactive source with a velocity of a few mm/s and recording the spectrum in discrete velocity steps.

Hyperfine interactions between the nuclear probe and its local environment are categorised as Isomer Shift (IS), Quadrupole Splitting (QS), and Magnetic Splitting interactions. The strength of these interacts is dependent on the electronic, magnetic and valency state of the atoms in the material.

The Isomer Shift (IS) arises due to differences in the electronic environment defined by the s-electron density and is observed as a negative or a positive shift off the centre (zero velocity) of the spectrum (Figure 4.3). The origin of the observed shift is the coulomb interaction between the nuclear charge and the electron density at the nucleus. Thus, the depicted difference in nuclei structures (s-electrons) of the absorber and the source is converted into a shift of the resonance energy of the transition. The IS reveals information about valency states, ligand bonding states, electron shielding and the electron-drawing power of electronegative groups.

The Quadrupole Splitting (QS) arises due to the interaction between the nuclear quadrupole moment of the nuclear state and the Electric Field Gradient (EFG) of the charge distribution in the surrounding environment. This asymmetric electronic charge distribution or ligand arrangement splits the nuclear energy levels. In the case of ^{57}Fe with I=3/2 excited state, the level splits into substates $m_i = \pm 1/2$ and $m_i = \pm 3/2$ and the spectrum consists of doublet transitions (±1/2 to ±1/2 and ±1/2 to ±3/2) (red diagram in Figure 4.3). The separation between the peaks of the doublet is proportional to the magnitude of the QS.

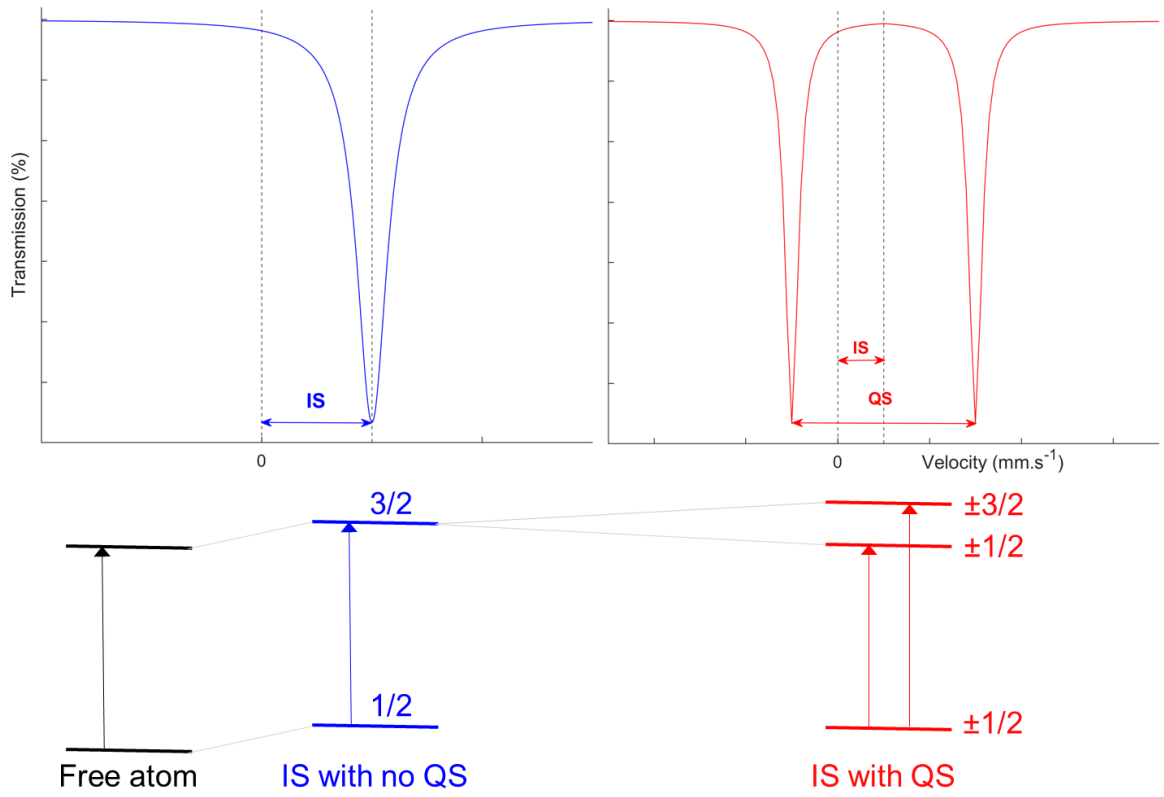

Figure 4.3: The diagram indicates the Isomer Shifts (IS) and Quadrupole Splitting (QS) for a 1/2 to 3/2 transition. The IS magnitudes are expressed as a shift from the centroid of the spectrum for a single peak (blue plot), while for a doublet, the IS is the segment between the midpoint of the doublet and zero and the QS is spacing between the two peaks.

The magnetic splitting (Zeeman splitting) is another characteristic of Mössbauer spectroscopy, which is observed in the fitted spectrum as six peaks. The sextet represents the dipolar interaction of the nuclear spin moment with the existing magnetic field. The peaks are in fact transitions between the excited and ground states of the nuclear levels as imposed by the selection rule.

Mossbauer spectroscopy measurements, in this work, were carried with a parallel plate avalanche counter (PPCA). The PPCA was equipped with ^{57}Fe enriched stainless steel and graphite electrodes, and the spectra were collected for more than 10 days (over 10000 counts for small statistical error).

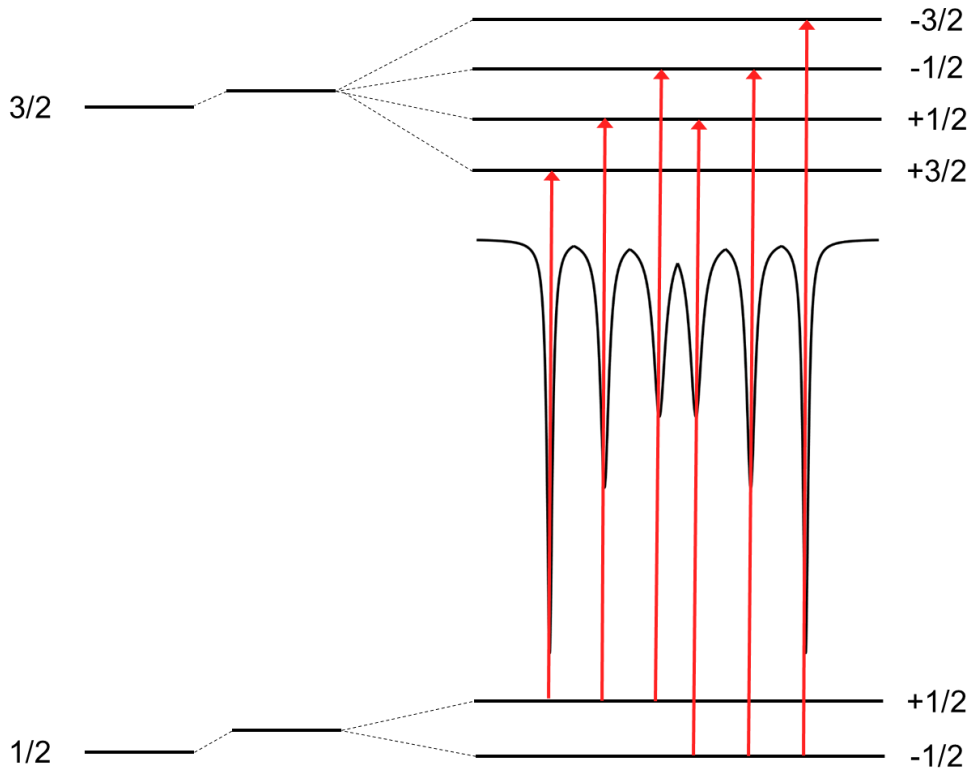

Figure 4.4: Magnetic splitting of the nuclear energy levels.

Chapter V

5 SYNTHESISED CARBON NANOSPHERES BY PLA: RESULTS

5.1 Morphology and composition analysis

The morphological features on the HOPG surface after successive laser irradiations were characterized by scanning electron microscopy. A typical SEM image of the laser impact region is shown in Figure 5.1. The laser beam was focused to a spot size of diameter ~350 μm corresponding to a laser fluence of 2 $J.cm^{-2}$. The impact region is characterized by a shallow ablation crater with a clear formation of a raised rim approximately 400 μm away from the impact epicentre. The surface ablated at repetition rates of 5 Hz with a pulse dwell time of 17 ns. In Figure 5.1, the SEM image illustrates the region where the raised rim is formed which at first instance is characterized by carbon lifted micro-size fragment shards, or simply graphene-like sheets. This is consistent with the formation and propagation of a shockwave as has been described in [107]. The intense absorption of the laser beam focused onto the solid material, generates a highly directed plume from the irradiated zone. This vapour plume may initially contain solid, and liquid clusters, which under more ablation get ionized, causing a phase transformation, and the outcome is hot dense plasma [44]. The expansion of this high-temperature plasma just a few microns above the irradiated zone, induce a mechanical impulse to this solid material causing plastic deformation and work hardening [39].

The result of the pressure waves produced at the target surface is a shockwave travelling laterally in the plane of the sample since the skin depth limits the energy spread in the transverse direction to 55 nm. This is also valid when the peak pressure exceeds the yield strength of graphite and agrees with Jenkins Model of plastic deformation for which micro-sized cracks within the centre of the irradiated spot due the strain induced

by the shockwave in elevated temperature were observed with electron microscopy [108], [109].

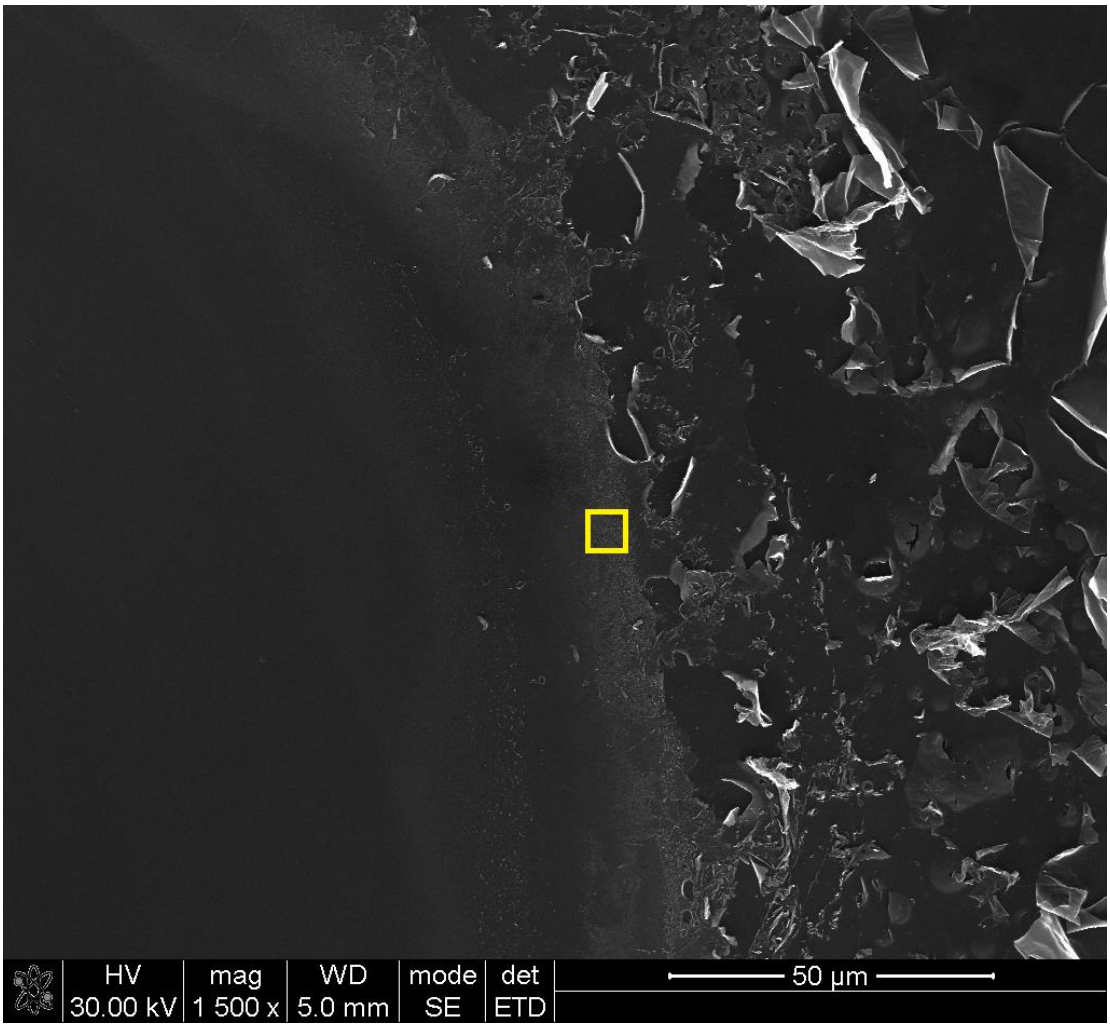

Figure 5.1: SEM image of irradiated HOPG sample for laser excitation fluence of 2 J.cm^{-2}, 15 sccm flowing rate, 1000 pulses, and 5Hz, showing the rim and the structural damages (disordered graphite and graphene-like sheets) caused by the shockwave in the surrounding area of the impact region. The yellow square in the inset image represent the magnified zone reported in the next figure.

Upon closer surveillance of the region at the edge of the rim and by using higher SEM magnification (×120000), additional interesting nanostructures with spherical morphology and a size range between 40 and 50 nm were observed, as seen in Figure 5.2 (a) and (b). EDX analysis performed over these nanostructures in this region next to the rim confirmed the pure carbon composition of the observed nanospheres and a typical EDX spectrum is shown in Figure 5.3.

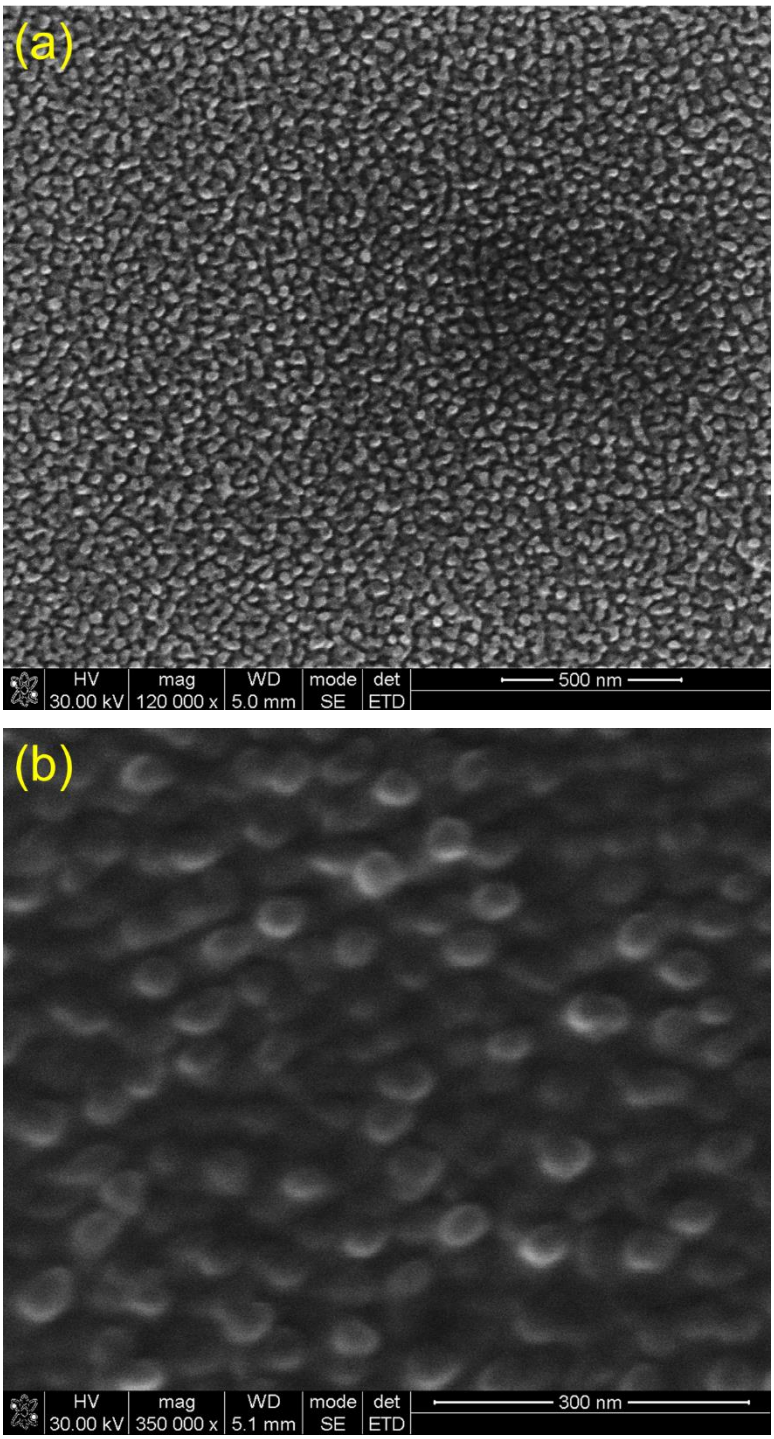

Figure 5.2: High magnification SEM images taken at the shockwave region shown in Figure 5.1 (yellow square), revealing the formation of carbon nanospherers on HOPG surface for a laser energy density of 2 $J.cm^{-2}$, 15 sccm flowing rate, 1000 pulses, and repetition rate of 5 Hz (a). (b) is a zoom within the region where the carbon nanospheres are formed.

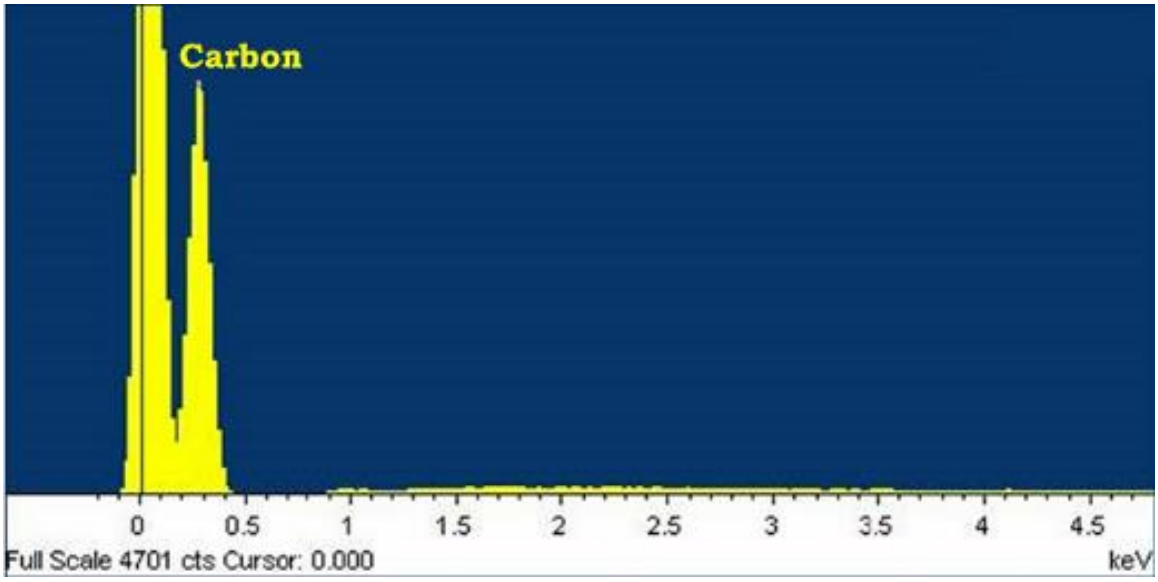

Figure 5.3: EDX spectrum was taken on the carbon nanospheres as in Figure 5.2 (a). The only presence of the carbon peak shows the purity of the formed carbon nanospheres from HOPG, and no external contaminations are detected.

5.2 Raman analysis

Subsequently to the morphology and elemental composition investigation, we performed Raman spectroscopy studies over the pulse laser irradiated areas and over the region where the nanospheres were observed. The micro Raman facility used in the present work was equipped with a scanning laser beam of ~1μm in diameter at the focal point, a CCD and a motorized micro-controlled stage for easy identification of the irradiated spots. In order to map the surface structural morphology caused by the laser in different areas of the impact and of the shockwave, line-scan spectra were acquired. The line-scan covered regions located within the impact area directly exposed to the laser (beam spot) and extended to the outer region over which the shockwave propagates, as seen schematically in Figure 5.4. These line-scan spectra are compared to Raman reference spectra obtained over the virgin HOPG surface of the same sample prior to irradiation, as shown in Figure 5.5. The corresponding laser irradiation was performed with 1000 pulses, with each pulse having energy density of the order of 2 $J.cm^{-2}$ and with an optimized Ar/H_2 gas flow rate of 15 sccm.

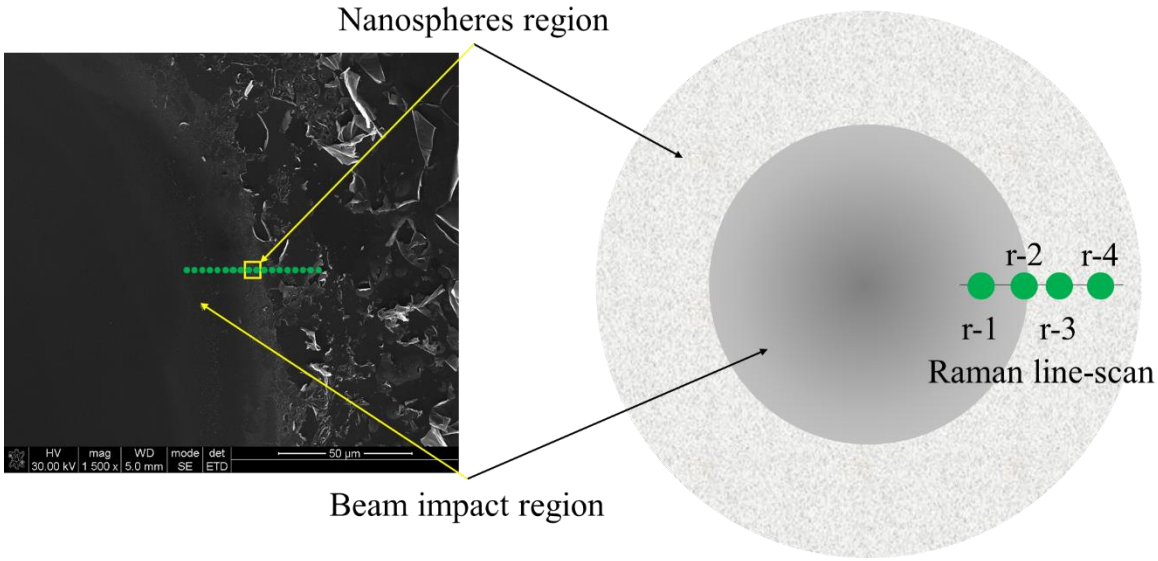

Figure 5.4: Illustration of the selected Raman spots (green spots) from a prior applied line-scan (inset on the left). The line-scan was taken within the impact laser region and extended to the shockwave area where carbon nanospheres are grown, as described in Figure 5.1.

The Raman spectrum of the pristine region shows a strong presence of the so-called G band around 1580 cm^{-1} corresponding to the first-order scattering of the E_{2g} mode. Also, it is the characteristic signature of the stretching of sp^2 bonds, forming the HOPG honeycomb structure [110].

In regions within the initial beam impact size, a second band at around 1350 cm^{-1} developed, and it corresponds to the well-known D band, associated with the breathing mode of the lattice. This mode describes any disorder or modification in the lattice that may be induced by laser irradiation. Raman spectra corresponding to regions just a few microns away from the formed rim of the shockwave (r1, r2) exhibits a progressive increase of the D-band intensity and the relative intensity ratio of the D and G bands.

The spectra over the rim boundary, where carbon nanostructures are observed according to the SEM analysis, are finally characterized by a noticeable decrease of the G band intensities and a visible shift to higher wavenumbers is observed by comparison to the virgin HOPG Raman spectrum.

The D band intensity increases and eventually becomes more prominent than the G band (r3, r4 (Figure 5.5 (a))). The progressive increase of the D band intensity is due to the intensification of the damage in agreement with the propagating shockwave.

As has been elaborated by Ferrari *et al.* [111], in their "Interpretation of Raman Spectra of Disordered and Amorphous Carbon", the transformation from graphite to nano-crystalline graphite is confirmed by

- the shift of the G peak from 1581 to ~1600 cm^{-1},
- the appearance of the D peak,
- an increase of I_D/I_G ratio, and
- the loss of the doublet of the 2D peak (~2700 cm^{-1}).

The manifestation of all these characteristics is conspicuous in our Raman spectra in Figure 5.5 (a) and (b), obtained over the region where the carbon nanostructures are formed and argue strongly for the formation of carbon nanospheres as visualized by the SEM imaging.

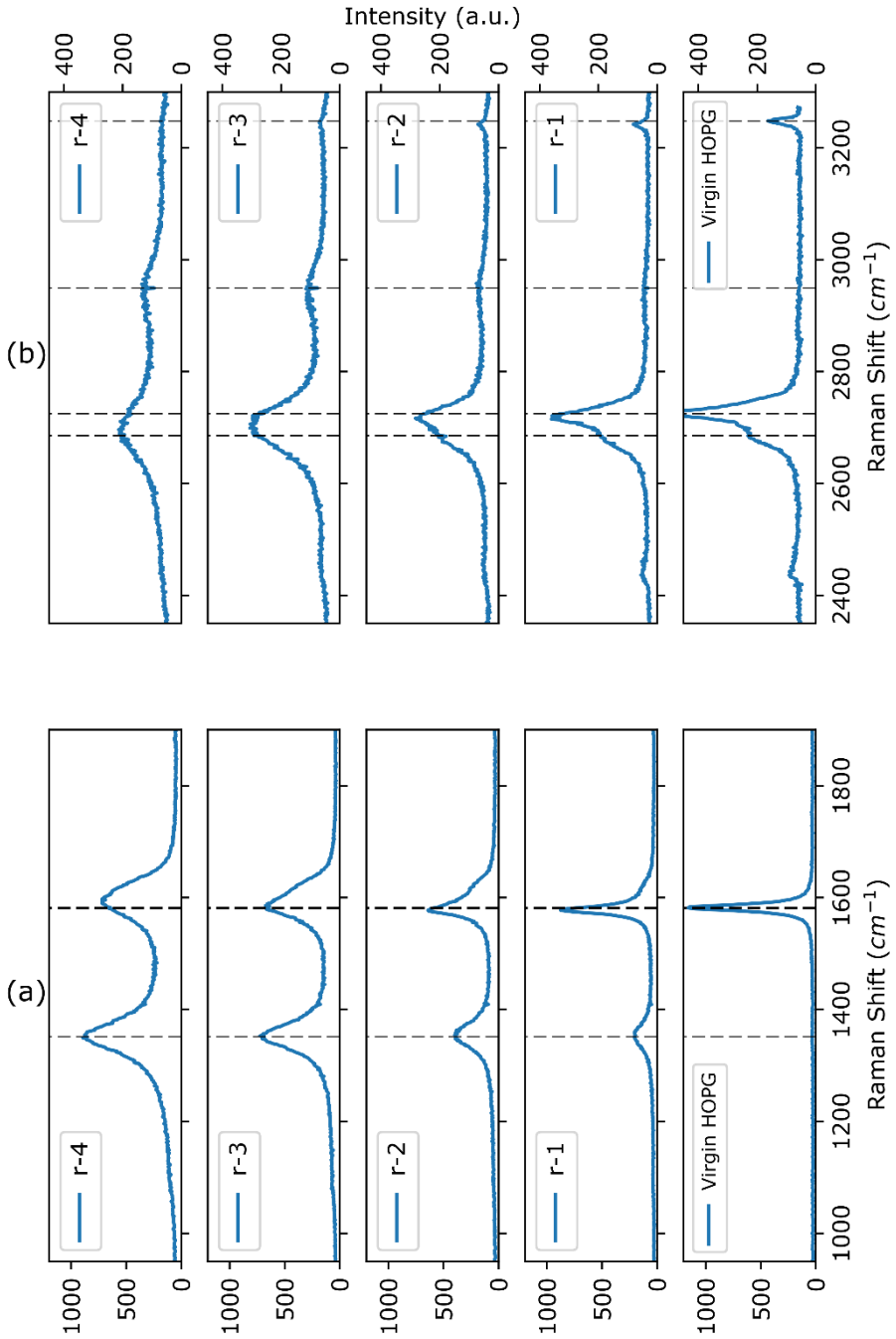

Figure 5.5: Low (a) and high (b) wavenumber spectra of micro Raman line-scan as schematically illustrated in Figure 5.4 for an irradiated HOPG sample with parameters of 2 J.cm^{-2}, 1000 pulses, 5 Hz, and 15 sccm. The line-scan covered the laser impact region (r-1, r-2), and the shockwave region (r-3, r-4), where carbon nanospheres were formed. The line-scan spectra were compared to Raman spectra of virgin HOPG sample.

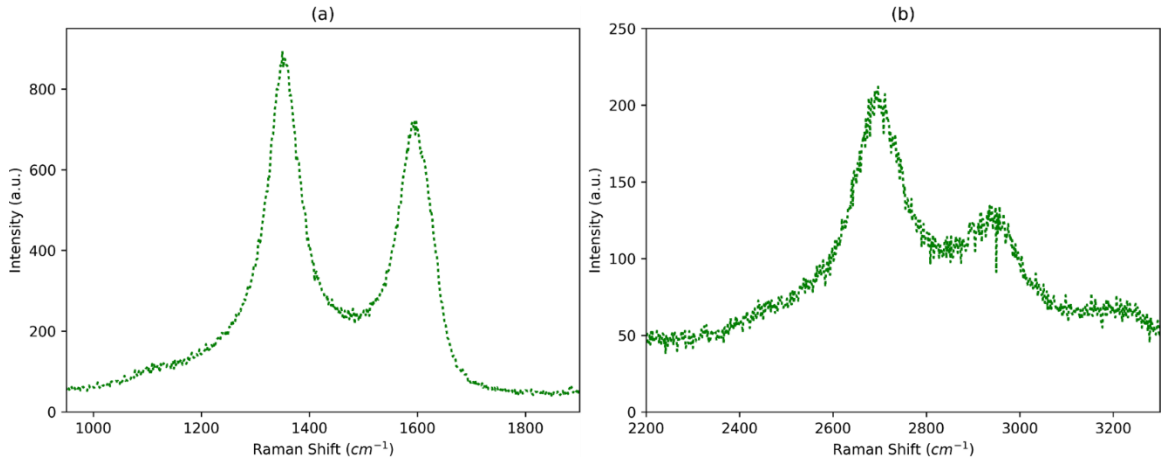

Figure 5.6: (a) and (b) shows respectively the low and high wavenumber of Raman spectra at the position r-4 (where carbon nanospheres are located) as mentioned in Figure 5.5.

It is interesting to note that, as seen in Figure 5.6 (b), additional broad bands in the range between 2700–3200 cm^{-1} have been observed in the Raman spectra corresponding to the nanospheres. These lines have been reported and discussed in the relevant literature before on carbon nanomaterials. The 2720 and 3242 cm^{-1} bands of HOPG are attributed to the second-order D (2D) and G (2G) modes respectively [110]. The observed band at 2950 cm^{-1} corresponds to the combination mode of D and G bands. The characteristics of these bands in terms of intensity, broadness, and red-shifts follow a well-established pattern reported in the literature [112], which is directly related to the growth of carbon nanostructures. Such a pattern can be noticeably seen in the present spectra (Figure 5.5 (b)). The 2720 cm^{-1} D' (2D) band progressively shifts to low frequencies, with broadening and decrease in the intensity in the region of high nanospheres production. The 3242 cm^{-1} G' (2G) band follows a similar pattern until it almost disappears in the region of high production of nanospheres.

In addition, the Raman spectra from the nanospheres produced with our pulsed Laser method were compared to Raman spectra obtained from carbon nanospheres produced by using the Non-Catalytic Chemical Vapour Deposition (N-CVD) approach. These CVD nanospheres were acquired from Neil Coville's group [12]. The comparison, as seen in Figure 5.7, shows a similar trend in terms of the intensity and the Raman shifts. The FWHM of the D band in our case is narrower suggesting that the carbon nanospheres

produced by our technique are much more crystalline with more ordered local structure and probably contain sp^3 type crystallites in comparison to carbon nanospheres formed by CVD. Furthermore, the combination mode of D and G bands at 2950 cm^{-1} is noticeably pronounced in the case of the laser-induced carbon nanospheres (Figure 5.7 (b)). This feature has also been observed in carbon nanospheres produced by Miao *et al.* [112].

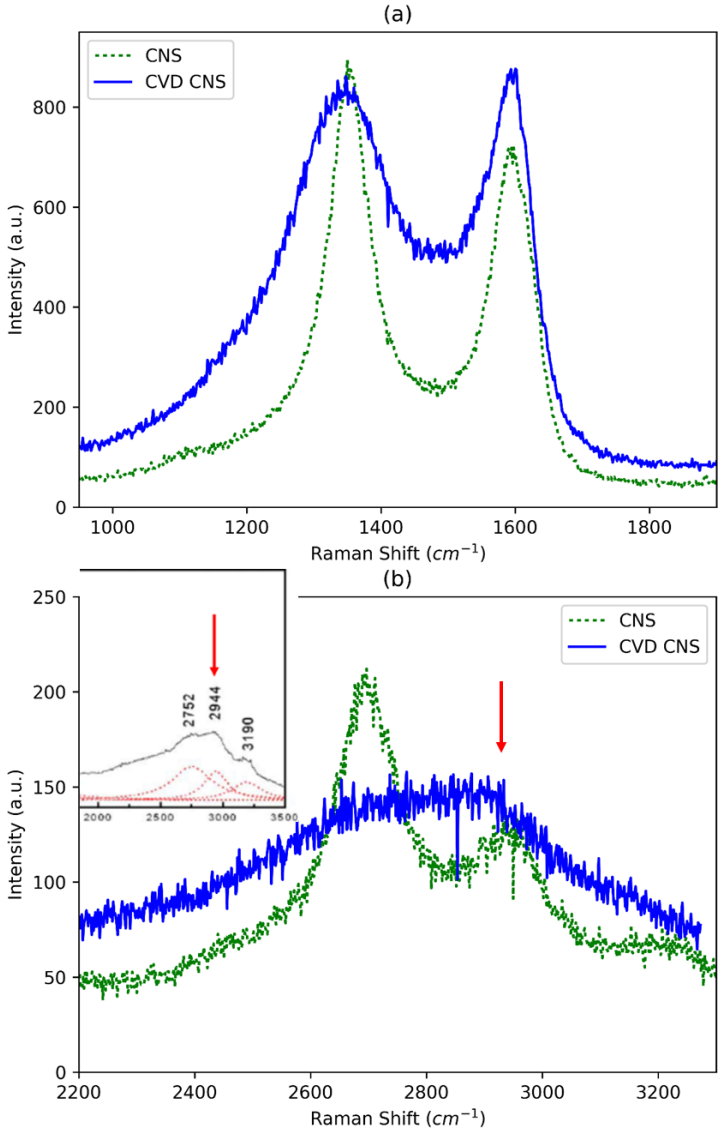

Figure 5.7: Low frequencies (a), and high frequencies (b) micro Raman spectra of carbon nanospheres produced by pulsed laser irradiation (green dashed line) of parameters of 2 $J.cm^{-2}$, 1000 pulses, 5 Hz, and a flow rate of 15 sccm, and carbon nanospheres produced by CVD (blue line). The red arrows shows the common peak observed at the high wavenumber in our carbon nanospheres spectra, and the spectra of carbon nanospheres reported in [112] (upper left inset of (b)).

5.3 Study of the Growth Process Parameters of carbon nanospheres

In order to establish the optima experimental conditions for the formation of carbon nanospheres and at the same time to obtain an insight on the physical processes and growth mechanism involved, the role of certain physical parameters was investigated, namely;

- the energy density,
- number of laser pulses,
- the hydrogen flow rate, and
- the pulses repetition rate.

5.3.1 Growth Dependence on Energy density

The fluence or energy density deposited by a laser pulse on the surface of materials determines, to a large degree, the surface response of the material and the possible phase transitions thereafter. Hence, in the present case, the fluence is regarded as an important parameter for the formation of carbon nanospheres. The carbon nanospheres growth dependence on the energy density deposited by the laser on the HOPG has therefore been investigated with and without the H_2 precursor gas.

The energy density was varied by changing the size of the focused beam spot on the HOPG surface. This was accomplished by manipulating the focal distance of the UV lens mounted on a translation stage, to forward or backward directions with respect to the HOPG surface. The repetition rate (5Hz), the number of pulses (1000 pulses) and the flow rate (15 sccm (standard cm^3/min)) of the H_2/Ar gas inside the chamber were kept constant. In this manner, energy densities of approximately 1, 2, 5, and 9 $J.cm^{-2}$ were selected.

The induced temperature and pressure rise upon the laser absorption and the plasma expansion was calculated. These calculations are based on the work of Burgess *et al.* [63], and Fabbro *et al.* [39] for different intensities, including the ones applied in our fluence study, and with K = 1800 W.m^{-1}.K^{-1}, cp = 0.72 J.g^{-1}.K^{-1}, and ρ = 2.27 g.cm^{-3} are the HOPG parameters provided by the material manufacturer. Figure 5.8 shows the temperature and pressure evolution as the pulse laser propagates to focus.

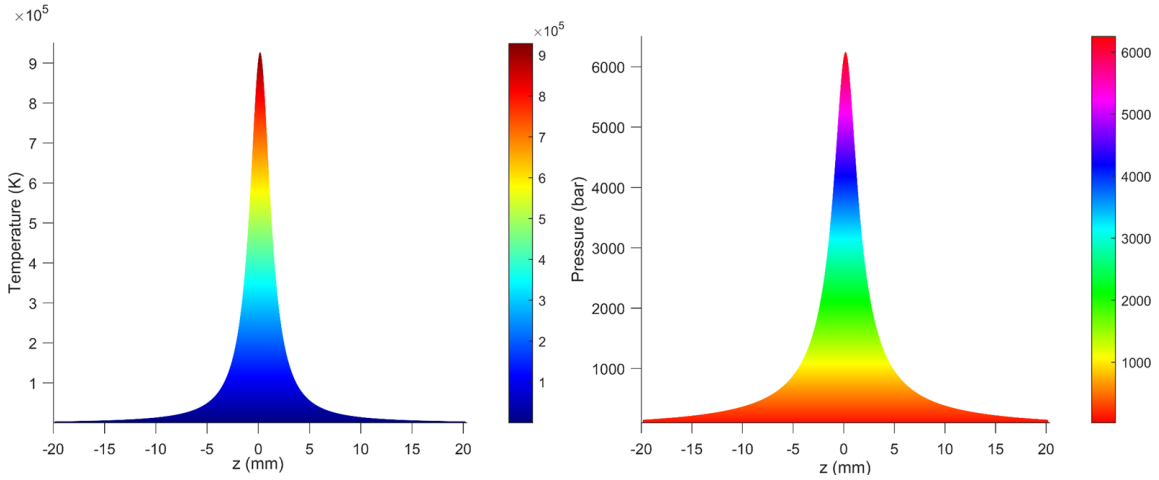

Figure 5.8: Calculated temperature (K) and pressure (bar) generated by the laser pulse as it propagated in the z-direction to focus. The temperature and the pressure were calculated based on the work of Burgess *et al.* [63], and Fabbro *et al.* [39].

SEM analysis was carried out on the sample irradiated by different laser energy densities (1, 2, 5 and 9 J/cm^2), in order to inspect and establish the degree of production (yield) of carbon nanospheres and morphology in terms of shape, size, and abundance. As before, the SEM images reveal two distinct regions; modifications at the epicentre and on the boundary of the laser impact. The common feature for all these different energy densities/fluences, as revealed in the SEM images, is the clear damage caused by the laser pulse at the centre of the impact region. Micro-sized cracks at the centre of the spots were observed in the four SEM images in the regions highlighted by the yellow arrows. The observed damaged morphology agrees with the Jenkins Model of plastic deformation according to which micro-sized cracks within the centre of the irradiated spot are formed due to the strain induced by the laser pressure in elevated temperature [108], [109]. These

pressure waves produced at the target surface are shockwaves travelling laterally in the plane of the sample, as shown in Figure 5.9 (b) (red arrows).

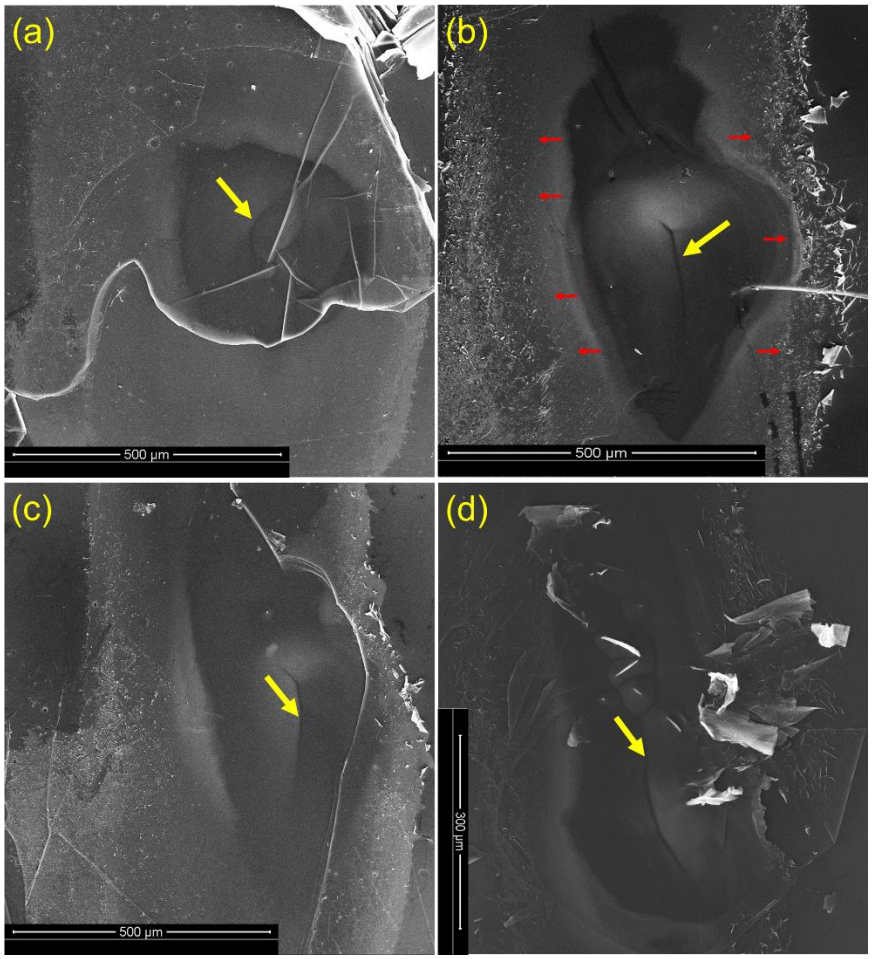

Figure 5.9: SEM imaging of irradiated spots with different energy densities. (a), (b), (c), and (d) represent spots irradiated with fluences of 1, 2, 5, and 9 J.cm^{-2} respectively.

Micro-structuring and nano-structuring takes place in different regions as the shockwave propagates along the surface seen in (b), (c), and (d) of Figure 5.9. This is indicative of phase transformations that require different optima values of temperature and pressure attained in different regions away from the epicentre and predicted by the graph seen in Figure 5.8. The nanostructures were observed under high-magnification in a region next to the rim of the created crater by the shockwave and covered an area of a couple of hundreds of squared microns (Figure 5.10 (b)). Microstructures are, on the other hand, observed further from the epicentre, close to the nano-structured HOPG surface

(Figure 5.10 (c)). These microstructures are mostly carbon lifted micro-size fragment shards, or simply graphene-like sheets as shown in Figure 5.10 (a).

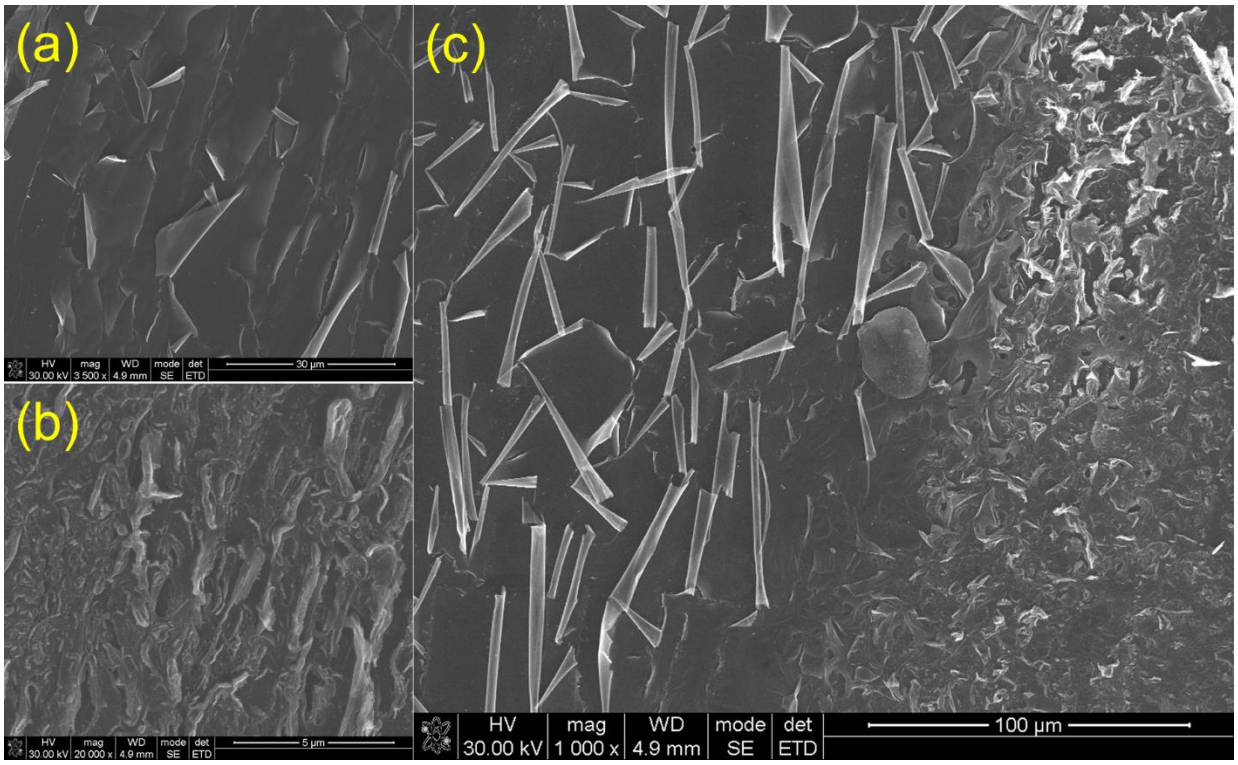

Figure 5.10: Example of (a) micro-structuration and (b) nano-structuration of the HOPG surface near the rim of the laser impact caused by the shockwave generated by the laser pulse (5 J.cm^{-2}, 5 sccm of H_2/Ar, 1000 pulses, and 5 Hz). (c) shows the damages and structurations (graphene like-sheets) evolution as the shockwave travelled to the outer region of the created crater. (a) and (b) are zoom-in from (c).

No production of carbon nanospheres was observed for the energy density of 1 J.cm^{-2}. The quality of the carbon nanospheres for fluences of 2 and 5 J.cm^{-2} are very similar (Figure 5.2 and Figure 5.11 (a). A lower fluence threshold for the formation of carbon nanostructures was therefore established to be of the order of 2 J.cm^{-2}. SEM images corresponding to the energy density of 9 J.cm^{-2} revealed extensive structural damage of the HOPG surface caused by the laser pulse accompanied by carbon nanospheres formation of inferior quality in terms of size, shape, and rate, as seen in Figure 5.11 (b). These type of carbon structures are referred to as nano-crystalline graphite [76].

It has been shown that the energy density is a highly critical laser parameter which influences the effect that the shockwave has on the modification and damage of the HOPG surface.

The different rate of formation of carbon nanospheres was established by careful inspection of their sizes and shapes in the acquired SEM images. The number of carbon nanospheres over ten different 250×250 nm^2 surfaces of the SEM images were counted and then the averages and standard deviations of created carbon nanospheres with different fluences (2, 5, and 9 $J.cm^{-2}$) were deduced. The results are tabulated in Table 5.1.

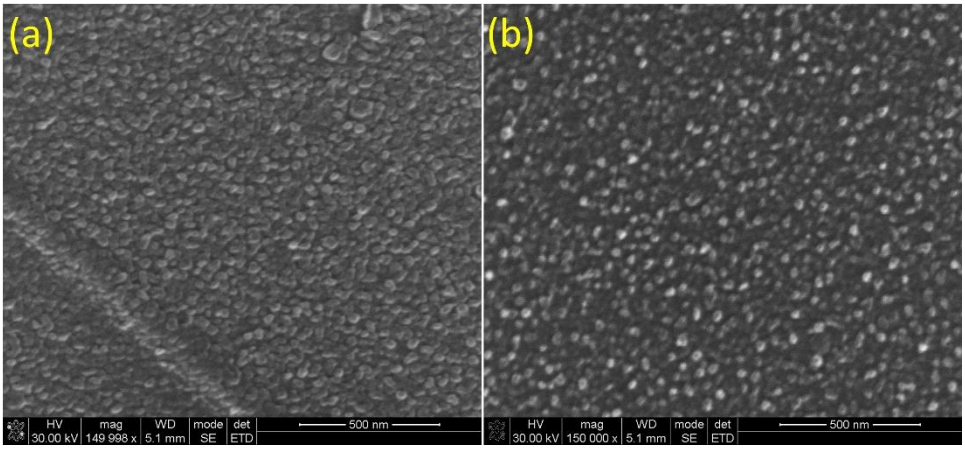

Figure 5.11: SEM images of carbon nanospheres formed using fluences of 5 $J.cm^{-2}$ (a), and 9 $J.cm^{-2}$ (b). The repetition rate, the number of pulses, and the flow rate were kept at their optimum values for both applied energy densities.

Table 5.1: Comparison of the different carbon nanospheres formed as the energy density applied is varied and the flow rate, the repetition rate, and the number of pulses were kept at 15 sccm, 5 Hz, and 1000 pulses.

Energy density (~$J.cm^{-2}$)	Rate (per 250 nm^2)
1	No carbon nanospheres
2	38 ± 3
5	24 ± 5
9	19 ± 3

Raman spectroscopy supplemented the scanning electron microscopy investigation of the aforementioned irradiations with respect to the role of the energy density influence. The same procedure which has been described in section 5.2 was followed to characterise the irradiated spots.

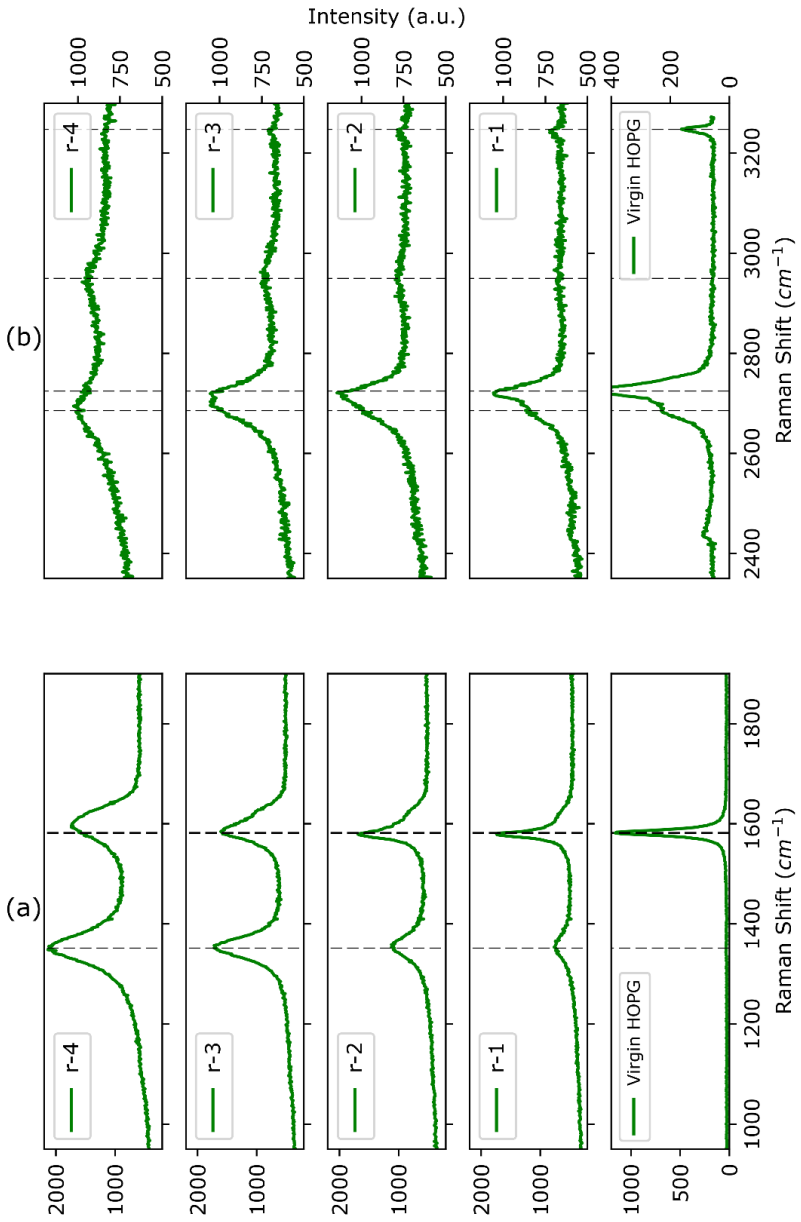

Figure 5.12: Low (a) and high (b) wavenumber spectra of micro Raman line-scan for an irradiated HOPG. The line-scan covered the laser impact region (r-1, r-2), and the shockwave region (r-3, r-4), where carbon nanospheres were formed. The characterized spot was irradiated under the laser condition of 5 J.cm^{-2}, 1000 pulses, 5 Hz, and gas flow rate of 15 sccm.

Micro Raman line-scan using low and high wavenumbers performed over an area irradiated with a fluence of 5 J.cm^{-2} are shown in Figure 5.12, corresponding to regions r-1, r-2, r-3 and r-4 as in the schematic representation of the crater/shock wave Figure 5.4. The spectra show a similar trend with respect to the peaks shifts and intensities increase and decay were observed in similar spectra corresponding to fluence of 2 J.cm^{-2} (Figure 5.5). This finding confirms that the carbon nanospheres created with 2 and 5 J.cm^{-2} are of similar structure.

The ratio between the intensities of the D and G lines of the Raman spectra, I_D/I_G, constitutes a good comparison with respect to the induced defect and nanostructure formation under different fluences. The calculated I_D/I_G ratio in that respect, for the 2 and 5 J.cm^{-2} fluences are tabulated in Table 5.2. The G and D intensities were selected from Raman spectra acquired exclusively from regions r-1, r-2, r-3, and r-4 of Figure 5.5 and Figure 5.12.

The crystallite size, L_a, can be deduced from the I_D/I_G ratios using the generalised Tuinistra-Koenig expression [111], which is valid for Raman with visible laser excitations [113], [114].

$$L_a(\mathrm{nm}) = 2.4 \times 10^{-10} \times \lambda^4 \left(\frac{I_D}{I_G}\right)^{-1} \quad (5.1)$$

The crystallite size, L_a, provides further evidence of crystalline disorder induced upon the laser impact. Table 5.2 shows the increase of disorder, expressed in the form of I_D/I_G ratios and their corresponding crystallite sizes L_a as the Raman line-scan progresses from the epicentre to the region with the formed carbon nanospheres.

Table 5.2: I_D/I_G ratios and their corresponding crystallite size L_a of Raman line-scans selected from laser spots irradiated with 2 and 5 J.cm^{-2}. The r-4 represented the crystallite size at the carbon nanospheres regions.

	Hydrogen flow rate = 15 sccm Number of pulses = 1000 Repetition rate = 5 Hz			
	2 J.cm^{-2}		**5 J.cm^{-2}**	
Region	**I_D/I_G**	**L_a (nm)**	**I_D/I_G**	**L_a (nm)**
r-1	0.23	71.41	0.24	69.12
r-2	0.61	27.15	0.66	25.36
r-3	1.07	15.66	1.07	15.70
r-4	1.24	13.51	1.22	13.70

5.3.2 The Role of Background Gasses on the carbon nanospheres growth

i. The role of Hydrogen content

As has been pointed out in the literature [115], [116], a non-catalytic growth process of carbon nanospheres involves the conversion of a carbon source into carbon and hydrogen radicals in a reaction that forms carbon nanospheres. The presence of hydrogen therefore during the laser irradiation of HOPG in the present work was an essential protagonist in the carbon nanospheres growth process.

The role of the hydrogen was consequently investigated in a two-pronged approaches namely

- foremost at constant laser irradiation conditions with varying hydrogen flow rates
- secondly by varying the laser pulse conditions at the optimized flow rate.

Thus, the evolution in the formation of carbon nanospheres was investigated in vacuum without Ar/H_2 gas flow, as well as with gas flow rates of 2, 5, 15, and 30 sccm, while the rest of the parameters were kept on their optimum as stated in Table 5.1.

It became apparent that no nanostructures could be obtained without the presence of hydrogen. This is because hydrogen is an essential quencher of the carbon vapour atoms and that it easily forms the C-H covalent bond [117]. SEM imaging of the formation of carbon nanospheres with respect to the hydrogen content corresponding to gas flow of 2 and 5 sccm is shown in Figure 5.13 (a) and (b) respectively. As the gas rate increased progressively, products that looked like carbon nanospheres appeared.

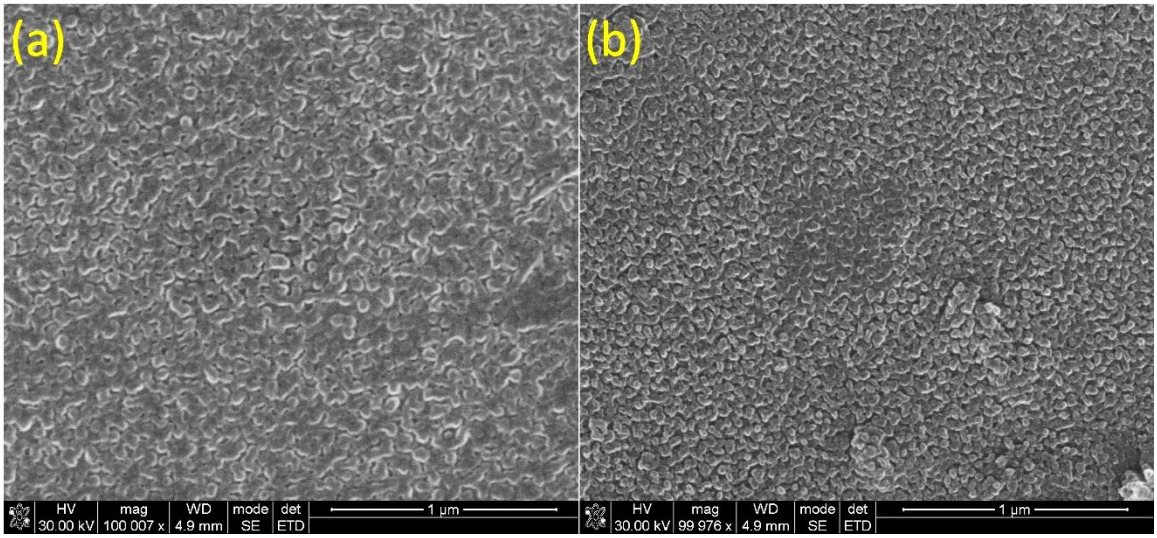

Figure 5.13: SEM images of carbon nano-structuration within the shockwave region. (a) and (b) are carbon nanospheres in gradual formation with a mixture gas of a flow rate of 2 sccm (a), and 5 sccm (b), as the energy density, the repetition rate, and the number of pulses were kept at their optimum values.

At higher flow rates (30-35 sccm), carbon nanospheres were still produced, however, of lower quality and rate (Figure 5.14 (a)), by comparison to the ones created with a flow rate of 15 sccm (Figure 5.2 (a)). In some parts of region r-4, structures like carbon nanospheres were observed aligned in a string-like pattern and finally conglomerated into clusters (Figure 5.14 (b)).

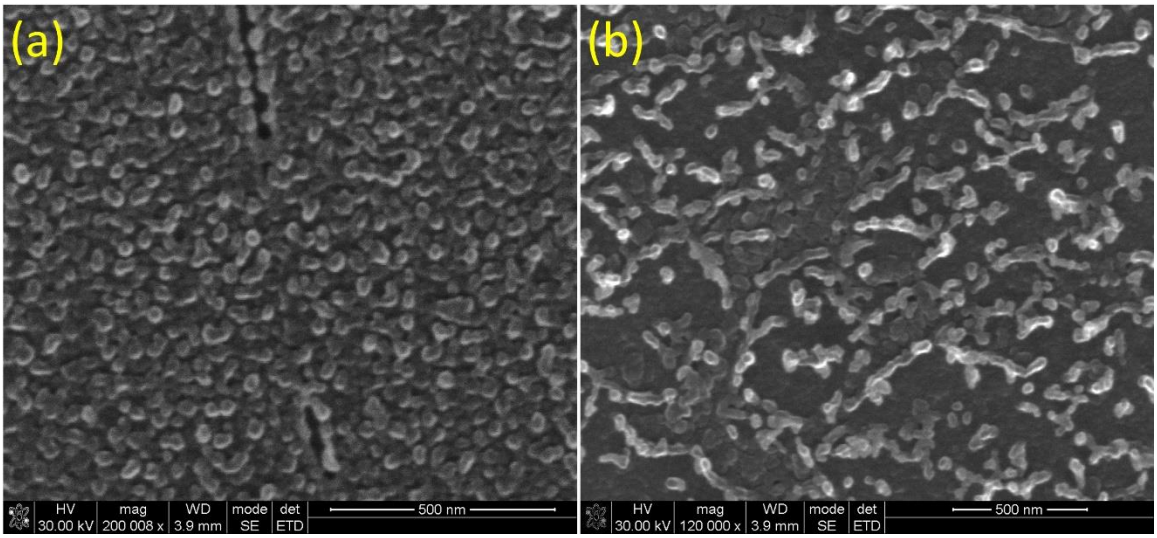

Figure 5.14: (a) SEM image of carbon nanospheres created with a H_2/Ar mixture of a flow rate of 35 sccm, a fluence of 2 J.cm^{-2}, a 1000 pulse, and a repetition rate of 5 Hz. (b) formation of different carbon nanostructures as strings and chains, or ropes of carbon nanospheres near within the shockwave region (as shown in Figure 5.1).

Table 5.3: Summary of the hydrogen influence on carbon nanospheres rate within the region of their formation and growth under the optimum condition.

Energy density = 2 J.cm^{-2} Repetition rate = 5Hz Number of pulses = 1000	
H_2/Ar flowing rate (sccm)	**Rate (per 250 nm^2)**
0	No carbon nanospheres
2	4 ± 2
5	7 ± 2
15	38 ± 3
30	19 ± 5

In summary, monodispersed and distinct carbon nanospheres as seen in Figure 5.2 are only observed for a flow rate of 15 sccm. These observations are consistent with the finding of You Zhang *et al.* in their paper “Preparation of Carbon Nanospheres by non-Catalytic Chemical Vapour Deposition and Their Formation Mechanism” [118], and more specifically the role the hydrogen plays in reducing the probability of collision between

carbon nanospheres nuclei, then their growth as spherical structures. Pol *et al.* showed the important role of hydrogen as a fluidizing agent in the formation of carbon spheres from hydrocarbons [119]. The hydrogen favoured the formation of hydrocarbon radicals that lead to carbon nanospheres growth [103]. The hydrogen contents controlled the morphology, size and the quality of the formed carbon nanospheres [101], [102].

ii. The Role of Methane (CH_4) content

In order to investigate further the effect of hydrogen on the formation of the carbon nanospheres during the laser ablation of HOPG, methane gas was used under the same vacuum conditions as before. The advantage has been that methane under the same vacuum conditions provides more hydrogen atoms by comparison to the H_2/Ar gas mixture which contains only 4% of hydrogen. In contrast methane, CH_4, contains 80% hydrogen in terms of atomic weight.

The same procedure as with the case of H_2/Ar was followed and a series of irradiations took place with the same optimised parameters as before. Therefore, the fluence, repetition rate and the number of pulses were set at 2 $J.cm^{-2}$, 5 Hz, and 1000 pulses, while the selected flow rates of methane inside the chamber were 1.2, 2, 5, and 10 sccm. Subsequent to the laser irradiations, SEM imaging analysis was conducted to investigate the morphological features of the impacted area and of the formed nanospheres.

The SEM analysis revealed very similar topological features and effects as the ones observed using H_2/Ar background gas described in the previous sections. As can be seen in Figure 5.15, the laser affected area is again characterised by two different regions; a central laser impact area with a crack at the origin (yellow arrows) and an area related to an outwards propagating shockwave (red arrows). At high magnification, the formation of carbon nanospheres is observed. Their location lies again at the outer region of the laser impact (yellow square). These nanospheres have similar shape, and size characteristics to the ones observed using H_2/Ar with the optimum flow rate of 15 sccm.

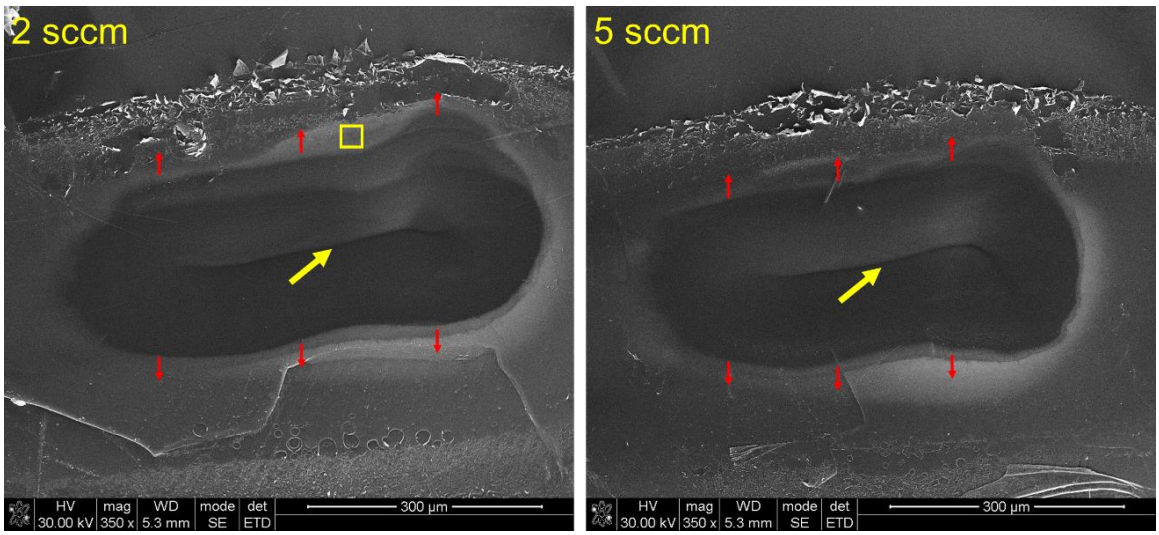

Figure 5.15: Laser ablated areas for variant methane flow rates (2 and 5 sccm) and laser parameters of 2 J.cm^{-2}, 5 Hz, and 1000 pulses. The image of the spots affected area displays a central laser impact region and the shockwave expansion in the surroundings (red arrows). High magnification from the shockwave region (yellow square) revealed the presence of carbon nanospheres as presented in Figure 5.16.

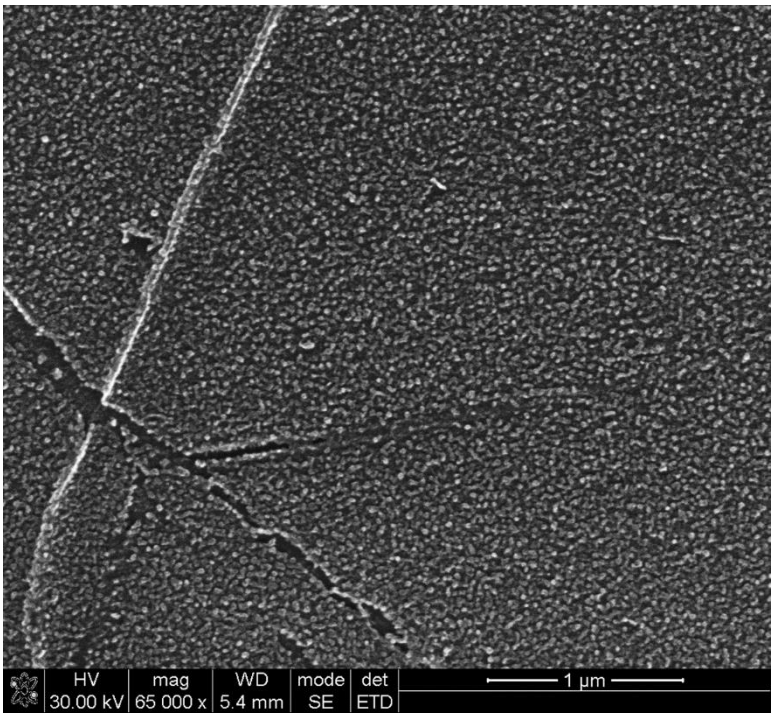

Figure 5.16: Map distribution of formed Carbon nanospheres within the shockwave region (yellow square from Figure 5.15) upon laser ablation in the presence of 2 sccm methane. (laser parameters: 2 J.cm^{-2}, 5 Hz, and 1000 pulses).

In contrast to the irradiations carried out in H_2/Ar environment, no flow rate threshold was observed for the formation of carbon nanospheres in the presence of methane. For all four flow rates selected (1.2, 2, 5, and 10 sccm), carbon nanospheres

formation were observed (Figure 5.17). The optimum spherical shape of the carbon nanospheres and their size distribution (between 40-50 nm), are clearly comparable to the carbon nanospheres grown under H_2/Ar gas background.

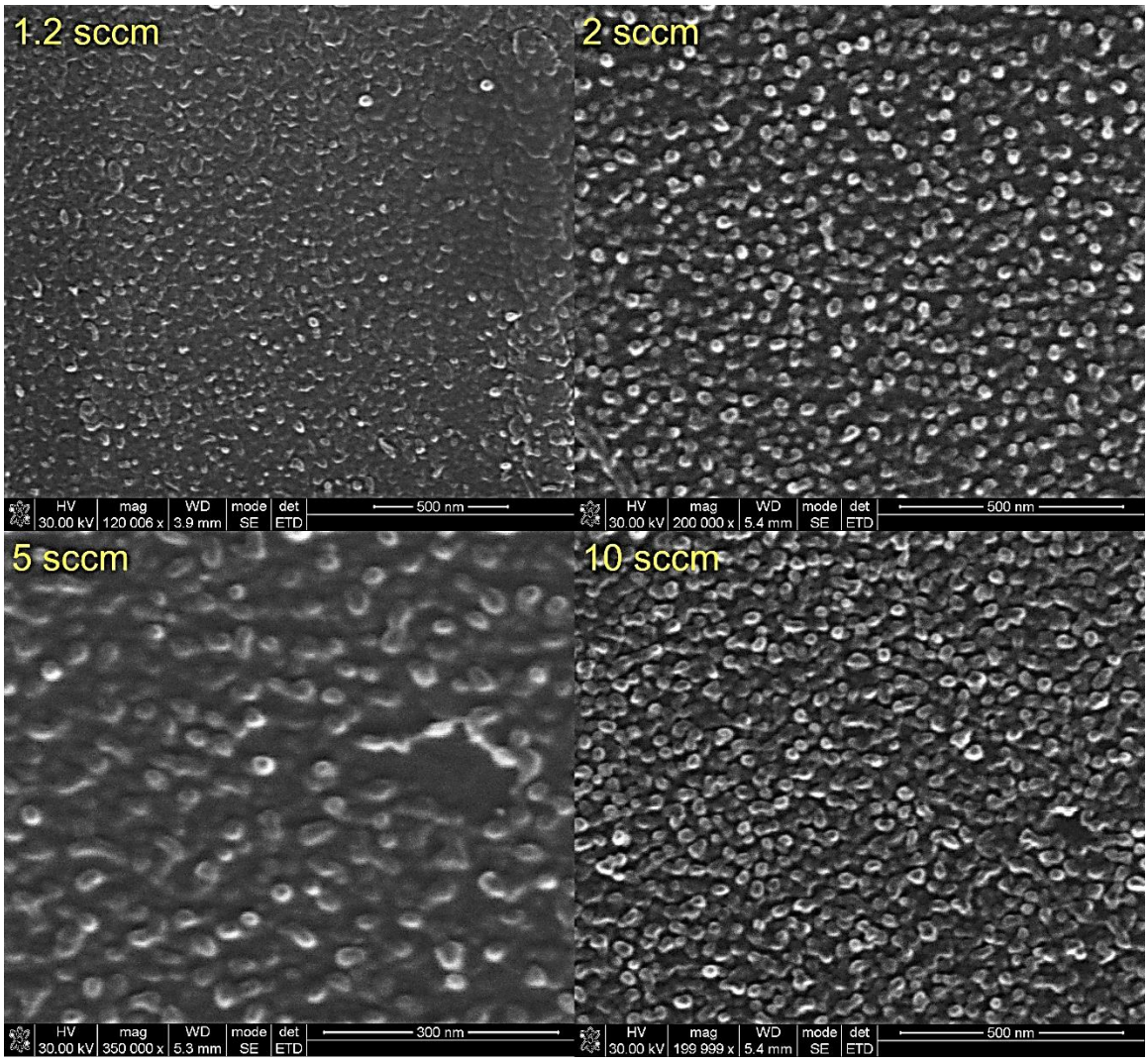

Figure 5.17: From shockwave regions revealing carbon nanospheres formation at spots irradiated at multiple flow rates of methane. The HOPG surfaces were irradiated with parameters of 2 sccm, 2 $J.cm^{-2}$, 5 Hz, and 1000 pulses.

Although carbon nanospheres are always formed, their abundance, shape and size, as seen in the SEM images (Figure 5.17), depend strongly on the methane flow rate used. The flow rate of 1.2 sccm is the lowest that could be used in the measurements, a limit imposed by the the potentiometer of the gas flow controller available. Even with this lowest flow rate (1.2 sccm), a high abundance of carbon nanospheres is formed, but of

inferior quality to that corresponding to 2 sccm. It seems that even at low flow rate there is enough quantity of hydrogen from the methane available to trigger the reaction. The optima values in terms of shape, size and abundance correspond to methane flow rates between 2 and 5 sccm.

5.3.3 Influence of Number of Pulses and Repetition Rate

The role of numbers of pulses was also investigated by using 100, 500, 1000 and 10,000 laser pulses while keeping the optimum values for the fluence at 2 $J.cm^{-2}$, for the hydrogen flowing rate at 15 sccm and the repetition rate at 5 Hz, constant. The first assemblies of carbon nanospheres are seen for 500 pulses. It was found that a critical number of 1000 pulses was needed for the optimum formation of carbon nanospheres with respect to abundance and quality as seen in Figure 5.18 (a) and (b). However, carbon nanospheres formation could still be observed after more than 10000 pulses were applied.

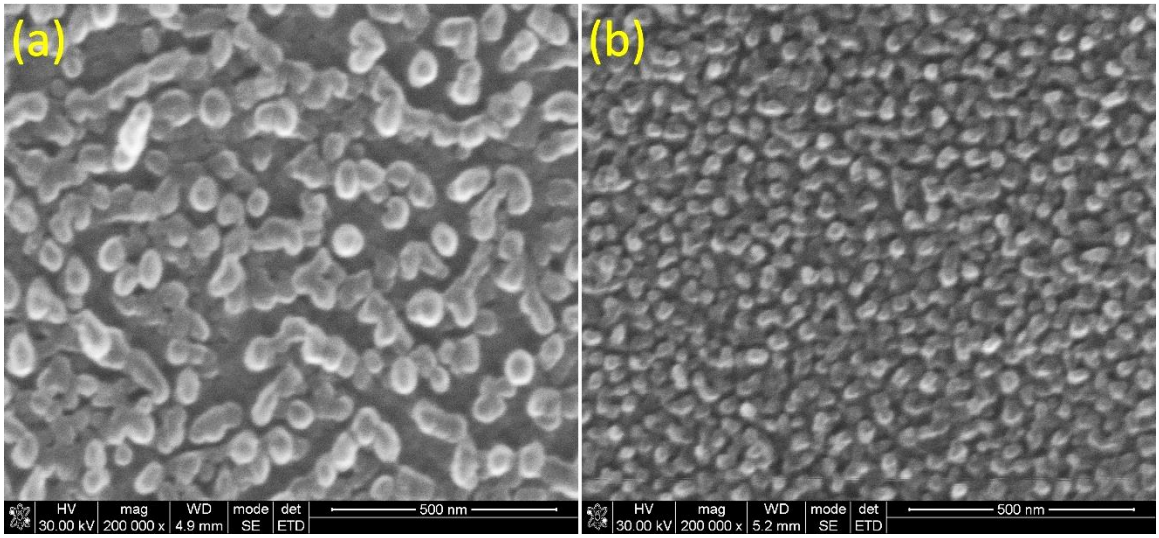

Figure 5.18: SEM imaging showing the effect of the number of pulses on the carbon nanospheres growth rate (a: 500 and b: 1000 pulses), as the rest of the parameters were kept at their optimum.

The pulse repetition rate seems to also be critical. As it was found to influence the carbon nanospheres formation, and in particular their growth rate or yield. Unfortunately,

with the currently available laser setup, it was not possible to use higher than 7Hz repetition rates (Table 5.4).

Table 5.4: Summary of the parameters study influence (number of pulses and repetition rate) on carbon nanospheres formation and growth.

Energy density = 2 J.cm^{-2} Hydrogen flow rate = 15 sccm Repetition rate = 5Hz		**Energy density = 2 J.cm^{-2} Hydrogen flow rate = 15 sccm Number of pulses = 1000**	
Number of pulses	**CNS rate (per 250 nm^2)**	**Repetition rate (Hz)**	**CNS rate (per 250 nm^2)**
100	No CNS	2	8 ± 1
500	9 ± 2	5	38 ± 3
1000	38 ± 3	7	18 ± 3
10000	15 ± 3	-	-

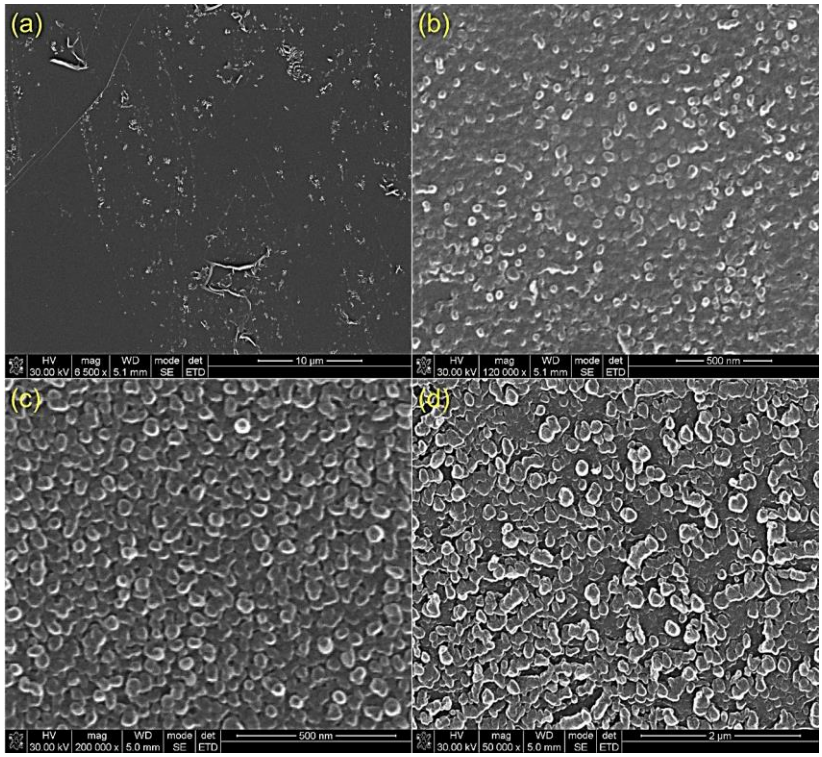

Figure 5.19: SEM images collected from the shockwave region of spots ablated with 2 J.cm^{-2}, 15 sccm of H_2/Ar, 7 Hz and numbers of pulses of 100 (a), 500 (b), and 1000 (c). (d) represents the new form of nanostructures depicted within the shockwave region for 1000 pulses.

Chapter VI

6 SYNTHESISED CARBON NANOSPHERES BY PLA: DISCUSSION

Numerous processes occur progressively during laser-solid interactions which involve intense, ultrafast electronic and vibrational states excitation and carrier diffusion, lattice expansion, photoionization, evaporation, melting, and shock wave generation [44]. The major portion of the energy carried by the laser is initially deposited into the electronic system of the lattice within the optical absorption depth (of the order of 55 nm in the present case) and the surface. Picosecond time-resolved shadowgraph and interferometry experiments [120], indicate that the plume is formed within the first picoseconds during laser ablation of solids above the ablated zone. This vapour plume may be associated with a large number of solid and liquid clusters emitted mainly from the ablated surface of the solid. Under more laser ablation, these clusters are ionized and phase transform into a gas phase known as plasma. The expansion of the hot plasma just a few microns from the irradiated surface launches a mechanical impulse, which propagates at sonic speed within the bulk of the crystal as a shockwave [39], [121]–[126].

Similarly, in the present case, the ablation of the surface resulted in two distinct regions of damage. The first region is noted as the laser impact region in which clear micro-cracks are revealed by SEM analysis. The damage induced upon impact is the result of numerous processes of photo-thermal nature (described above) during laser-solid interactions.

The second depicted region surrounds the impact regions. The generated vapour plume initially contains clusters of solid and liquid forms. Under successive ablations, these clusters become ionised forming a hot-dense plasma-plume. The expansion of this high-temperature plasma, just a few micrometres above the irradiated zone and in the presence of a background gas, causes a significant compression. Subsequently, the

pressure of the system (plume and background gas) reaches equilibrium by the launch of a mechanical impulse. The result of the pressure waves produced at the target surface in this manner is a shockwave which propagates at sonic speed laterally in the plane of the sample. These shockwaves induce the damage observed by SEM in the form of micro-sized cracks within the centre of the irradiated beam spot and at the borders of the laser impact regions. The latter agrees with Jenkins Model of plastic deformation due to the strain induced by the shockwave in elevated temperature [108], [109].

An important and exciting finding in the present work has been the formation of carbon nanospheres at a certain region of the shockwave propagation area. SEM imaging, EDX and Raman spectroscopy gave clear evidence that the formed nanostructures were pure carbon of nano-spherical forms, and linked them to similar findings in the literature, as has been reported in chapter VI.

It is clear that the formation of the carbon nanospheres is possibly initiated by photo-thermal ablation and a subsequently generated shockwave. The ablation and shockwave propagation leads to material extraction and liberation of carbon ions, after each laser pulse. The carbon ions recombine with hydrogen ions present in the background gas (H_2/Ar or CH_4) to form hydrocarbon radicals [127] prior to equilibrium, and prior to the next impact pulse. The coalescence and the recombination of the carbon-hydrogen species were favoured due to the large time scale between each pulse and the short relaxation time of the metallic system considered to be in the order of a few picoseconds.

The process of formation of these carbon nanospheres starts naturally with nucleation and ends with the complete growth of the created nuclei. Here, the nucleation is considered to be heterogeneous since hydrogen species are part of the nucleation process together with carbon ions. These hydrocarbon radicals constitute the embryos, which after each pulse become growth species (nuclei) and start to grow to clusters of a number of carbon-hydrogen molecules.

Based on the fundamental theory of nucleation, the nuclei are formed as follows:

- the formed plasma-plume is in a metastable state, contains carbon-hydrogen species and attempts to reach equilibrium by loss of Gibbs free energy,
- the variation in the Gibbs free energy, or simply the supersaturation, causes the transition from a metastable (plasma-plume) to a stable state (solid: nucleus).

The nuclei are considered to be of spherical shape with a radius greater than the critical radius R^*_{nuc} and contain n molecules of carbon-hydrogen. They need a minimum energy of W^*_{nuc} to form. Once a certain concentration of the nuclei is reached, they begin to grow by accommodating new hydrocarbon species produced after each laser pulse, until equilibrium is reached at which point stable clusters of 40-50 nm are formed.

The formation of these carbon nanospheres depends strictly on well-defined conditions, and each parameter plays a specific role and contributes towards the formation of the carbon nanospheres. These optimum conditions are summarized in Table 5.1, Table 5.3, and Table 5.4 and correspond to a fluence of 2 J.cm^{-2}, a gas flow rate of 15 sccm of H_2/Ar (2 sccm of CH_4), a 5 Hz repetition rate and 1000 of pulses.

Based on the fundamental theory of nucleation [86], there seems to be a critical carbon ion density needed in order to increase the probability of recombination to engender nucleation, and hence a critical number of pulses is a fundamental prerequisite. In the present study, 500 pulses were found to be the threshold pulse number needed for the growth of the nuclei, and the beginning of the carbon nanospheres configuration. It is interesting to note that the process has to follow the well-known phase diagrams with respect to temperature and pressure for any given phase. There are distinct temperature and pressure gradients along the direction of propagation of the shockwave from the epicentre of the impact to the rim. A critical combination of these parameters, in order to form Carbon Nanospheres, seems to be reached at the edge of the rim of the shockwave which promotes the phase transition and the growth of carbon nanospheres.

Following the theoretical description mentioned before, the values of these thermodynamic parameters, namely temperature and pressure, generated by the laser beam, have been calculated using formulas (2.13) and (2.17) respectively and the results are shown in Figure 6.1.

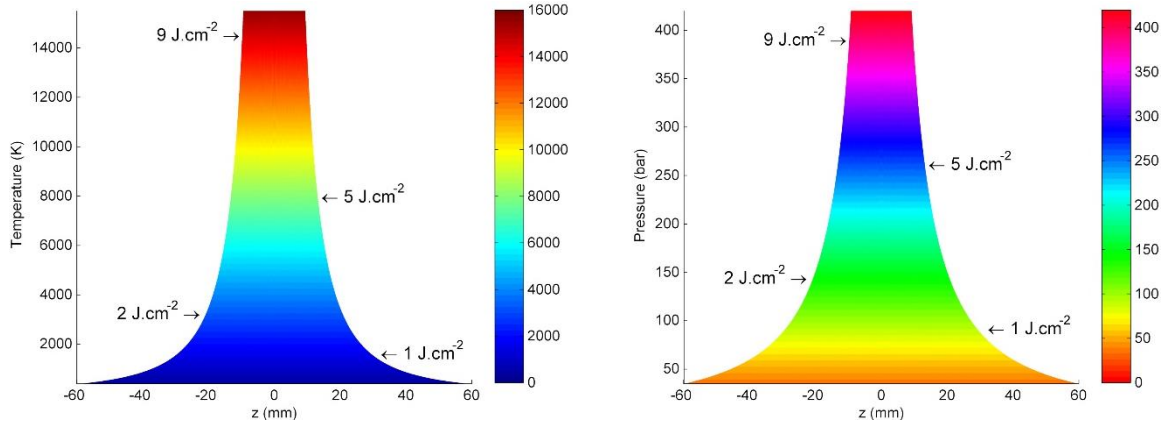

Figure 6.1: Calculated temperature (K) and pressure (bar) generated by the laser pulse, as it propagates in the z-direction to focus. The graph is cropped from Figure 5.8.

The calculated temperature and pressure values, therefore, corresponding to values of fluences 1, 2, 5, and 9 J.cm^{-2} used in this study are deduced from Figure 6.1 and presented in Table 6.1.

Table 6.1: The corresponding pressure, temperature, and supersaturation values calculated with formulas (2.17), (2.13), and (2.23).

Fluence (J.cm^{-2})	Pressure (Bar)	Temperature (K)	Supersaturation (J) ×e^{-21}
1	94.69	1731	-1.77
2	147.0	3349	16.9
5	264.5	8081	106.3
9	392.9	14630	272.4

These fluences are pinned in the P-T phase diagram of carbon shown in Figure 6.2 in order to assess the possibility of phase transition with respect to the different carbon phases. It was found that the experimentally determined optimum energy density (2 J.cm^{-2}) is located close to the border line between the carbon solid and carbon vapour phases. Within this area, most of the formed plasma-plume of metastable state transitions to a stable state (solid) to reach equilibrium.

This area between the solid and vapour carbon phases is known to be significant for thin carbon film formation where carbon deposition equilibrium is reached as well as for growth of carbon nanotubes [128]. Then, the nucleation process can be possible, provided that a high concentration of nuclei, becomes available, leading to a high rate formation of carbon nanospheres. It follows that the repetition rate, therefore, is also an important parameter which can control the critical number of carbon ions extracted between two pulses needed for the nucleation process to take place efficiently.

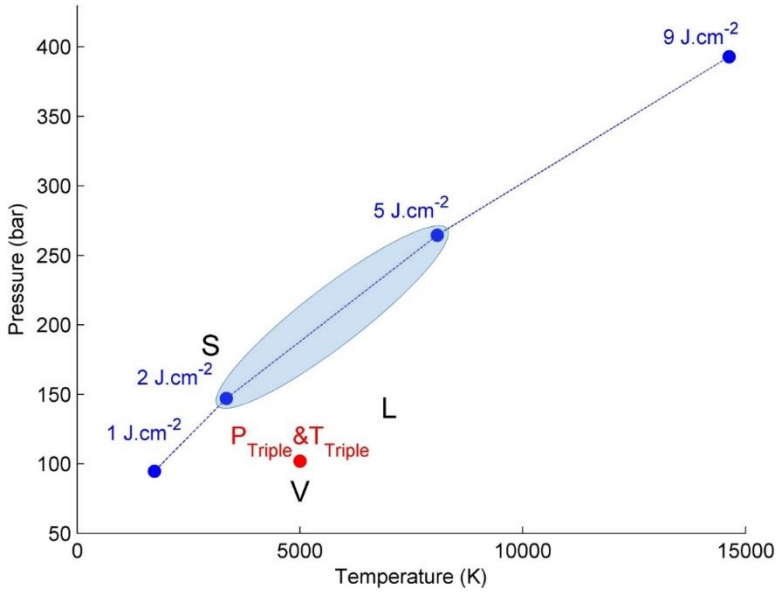

Figure 6.2: Pressure-Temperature diagram based on the fluences applied to the sample. The temperature and pressure are deduced from Table 6.1. S, L, and V represent the solid, liquid, and vapour carbon phases based on the P and T triple point data presented by the National Institute of Standards and Technology (NIST).

The supersaturation ($\Delta\mu$) values were also calculated with respect to the corresponding fluences used in Table 5.1. The calculation was based on equation (2.23)

which is commonly used to determine the supersaturation of a phase transition from a vapour to a solid phase as is the case in the present study (from a plasma-plume to carbon nanospheres). The calculations made use of the corresponding values of pressure and temperature listed in Table 6.1. The pressure at the thermodynamic equilibrium was taken as the pressure at the triple point (102 Bar), at which the three phases (solid, vapour, and liquid) coexist. The relation between the calculated values of supersaturation and the fluences of 1, 2, 5, and 9 J.cm^{-2} are shown in the graph in Figure 6.3: The blue markers show fluences for which the process of nucleation occurred, and the red marker where the nucleation process did not occur. The red and blue arrows define the directions of nucleation ($\Delta\mu > 0$) and non-nucleation ($\Delta\mu < 0$) respectively. This explains undoubtedly the reason why no nucleation occurs and therefore no carbon nanosphere formation was observed for fluences below 1 J.cm^{-2}.

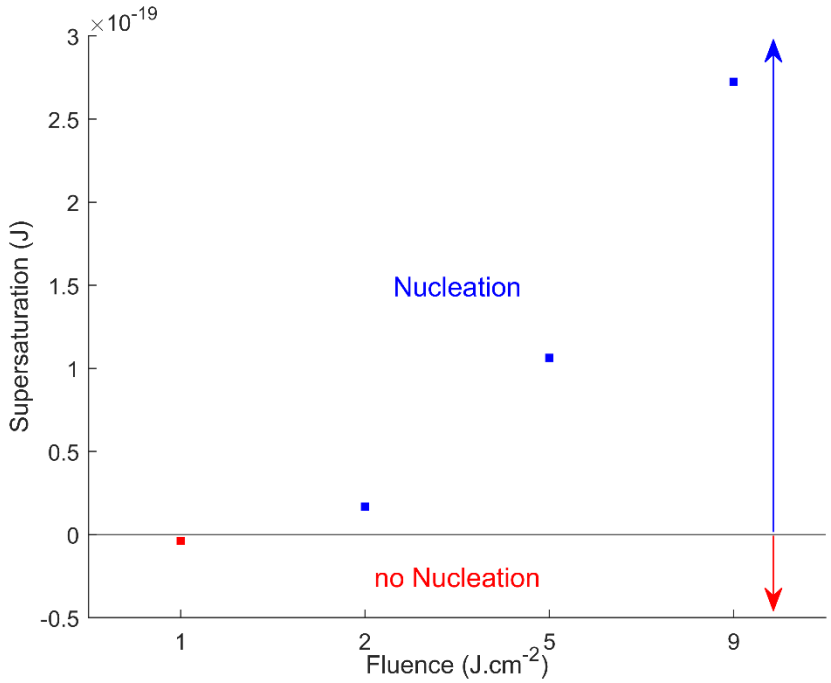

Figure 6.3: The graph represents the calculated values of supersaturation related to fluences of 1, 2, 5, and 9 J.cm^{-2}. The blue markers show fluences for which the process of nucleation occurred, and the red marker where the nucleation process did not occur. The red and blue arrows define the directions of nucleation ($\Delta\mu > 0$) and non-nucleation ($\Delta\mu < 0$) respectively.

The critical role of hydrogen to catalyse the sp^2 to sp^3 hybridisation is well known as is the characteristic sp^2/sp^3 fractions during the growth of carbon nanostructures. In

addition to the ease of forming the covalent C-H bonds. The hydrogen content as injected background gas during the laser ablation was an essential protagonist during the growth process of carbon nanospheres. The background gas has a dual role; firstly, it facilitates the generation of the shockwaves by introducing the required compression during the expansion of the hot plasma. Secondly, hydrogen ions in the background gas combine with carbon ions forming the hydro-carbon radical's embryos necessary for the initial nucleation process. It must be noted that in the present studies not a single carbon nanosphere was observed in ablations that took place in the absence of the background gas (H_2/Ar or CH_4). However, the progressive growth of carbon nanospheres started with injecting the background gas gradually (Table 5.3 for the case of H_2/Ar). The hydrogen played an important role in the formation of hydrocarbon species that enhanced the growth of carbon nanospheres. Also, the hydrogen content allowed the control of the morphology and the quality of the carbon nanospheres. Besides, this demonstrated the role of hydrogen as a fluidising agent and in reducing the probability of nuclei collision, then the growth of spherical carbon nanostructures. A critical hydrogen content was established at which carbon nanospheres were regularly-shaped and formed at high rates. The large difference between the optima flow rates of the two background gases needed is related to the high abundance of hydrogen ions in CH_4 (80% atomic weight) by comparison to H_2/Ar (4% of H_2).

Chapter VII

7 CARBON NANOSPHERES SYNTHESISED BY CVD: RESULTS AND DISCUSSION

7.1 Results and Discussion

High magnification SEM analysis performed on two sets of carbon nanospheres (A and B) produced in the School of Chemistry, University of the Witwatersrand [12], using the CVD method without catalysts, revealed nanostructures of spherical morphologies with diameters distribution of approximately 200-400 nm (A) and 400 nm (B). The carbon nanospheres from SEM images are not dispersed and are packed in necklace-like and foam-like structures.

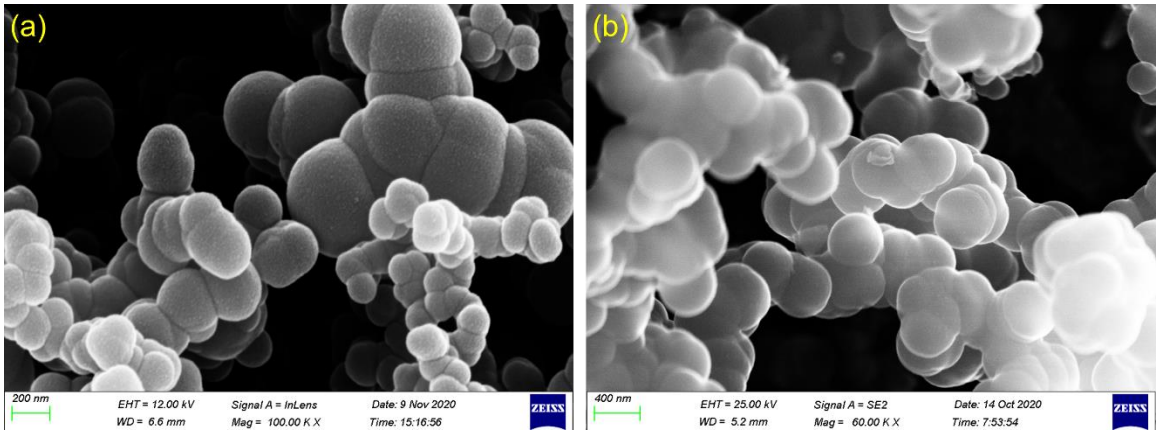

Figure 7.1: (a) and (b) are high magnification SEM images of carbon nanospheres powder of samples (A) and (B) respectively. The images show the necklace-like form structures of the carbon nanospheres of diameters of 200-400 and 400 nm.

EDX analysis of these carbon nanospheres shows the presence of carbon only, with no other elemental impurities detected within the limits of the measurements (at the parts per thousand sensitivity level), (Figure 7.2).

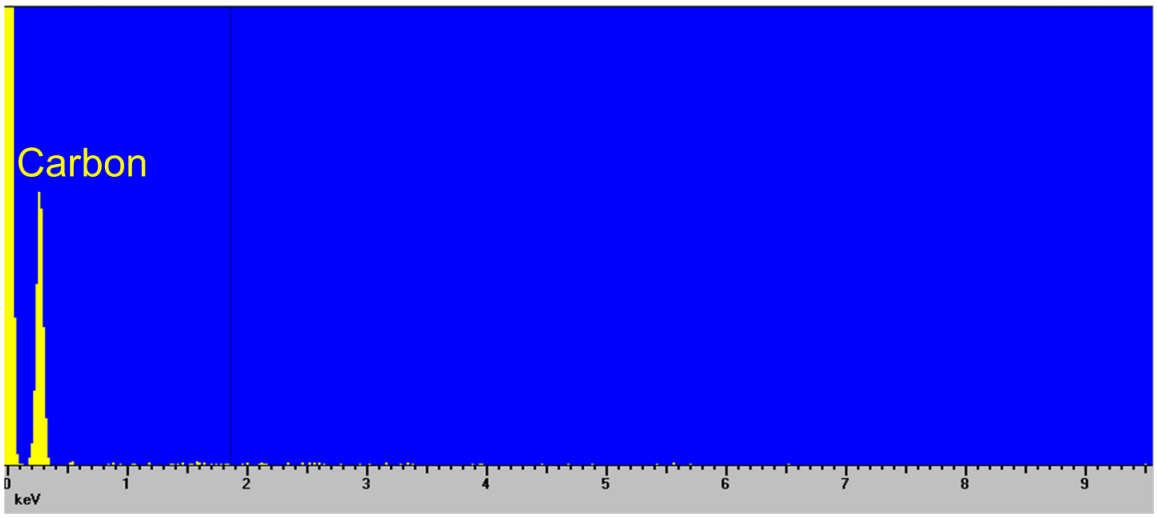

Figure 7.2: EDX spectrum of carbon nanospheres from the synthesized powder noted “A”. the spectrum shows the presence of the carbon elements only.

In addition, trace element analysis with sensitivity at the part per billion level was performed by means of Induced Coupled Plasma Mass Spectrometry (Perkin Elmer NexION 300 ICP-MS) on both samples “A” and “B” of the CVD synthesised carbon nanospheres. The main concern and focus has been on possible presence of elemental impurities that are magnetic. The ICP-MS scan was tuned to detect the following elements: ^{24}Mg, ^{51}V, ^{52}Cr, ^{55}Mn, ^{56}Fe, ^{59}Co, ^{60}Ni, ^{63}Cu, and the elemental composition is summarized in Table 7.1.

Table 7.1: Summary of the ICP-MS elemental analysis in part per million (ppm).

	^{24}Mg (ppm)	^{51}V (ppm)	^{52}Cr (ppm)	^{55}Mn (ppm)	^{56}Fe (ppm)	^{59}Co (ppm)	^{60}Ni (ppm)	^{63}Cu (ppm)
Sample “A”	91	9	4	1	126	0	3	1
Sample “B”	16	8	0	0	20	0	0	1

As can be seen, the metal contaminations detected are lower than 10 ppm in both samples except for ^{24}Mg, and ^{56}Fe impurities. These elements were detected in high quantities in sample “A” in comparison to sample “B”. For example, in sample “A”, the

amount of ^{56}Fe detected was 126 ppm, and 20 ppm in sample “B”, making ^{56}Fe the highest impurity in sample “A”.

7.1.1 Magnetic properties

Magnetic characterisation measurements were performed on the two synthesised samples “A” and “B” using the DynaCool 12T PPMS operating in DC-magnetisation of the VSM measurement mode. Prior to the measurements, the mass of the carbon powder samples was carefully measured with an electronic balance and then the samples were transferred to the poly-carbonate capsule and fitted in the gold coated brass holder at 35 mm. The sample holder was connected to the VSM probe and loaded onto the PPMS for calibration measurement and analysis.

Two types of measurements were performed. Firstly, the temperature dependence within a range of 2-300K of the magnetic moments μ(T) was determined at zero-field (ZFC) and field cooled (FC) conditions. The FC measurements were collected in both directions after the temperature was decreased (cooling) and then increased (warming) at constant ramp rates. Moreover, the dependence of the magnetic moments (in emu) on applied magnetic field (H) in Oersted (Oe) was investigated. These measurements were performed at a number of different temperatures from 2 K up to 310 K.

Figure 7.3 presents the temperature dependence of the magnetic moment $\mu(T)$ of samples “A” and “B” of the carbon nanospheres measured at 5 kOe in the temperature range $2 < T < 310$ K. Based on this graph, the FCC and FCW curves of both samples “A” and “B” are non-linear and the magnetic moment dependences typically show monotonic exponential increase with decreasing temperature. The values of the magnetic moments $\mu(T)$ for sample “A” are positive with high magnitudes, while for sample “B” the magnetic moments are negative all along the x-axis indicating a diamagnetic behaviour.

It is interesting to note that a discrepancy/gap between the FCC and FCW measurements, in the temperature range between 50 and 140K for sample “A”, was

observed as depicted in a close-up within this temperature range in the upper right-hand inset of Figure 7.3. The temperature dependence on magnetic moment could also be indicative of the condensation of electrons/fermions in Landau level n = 0 with H field (T >> 0K).

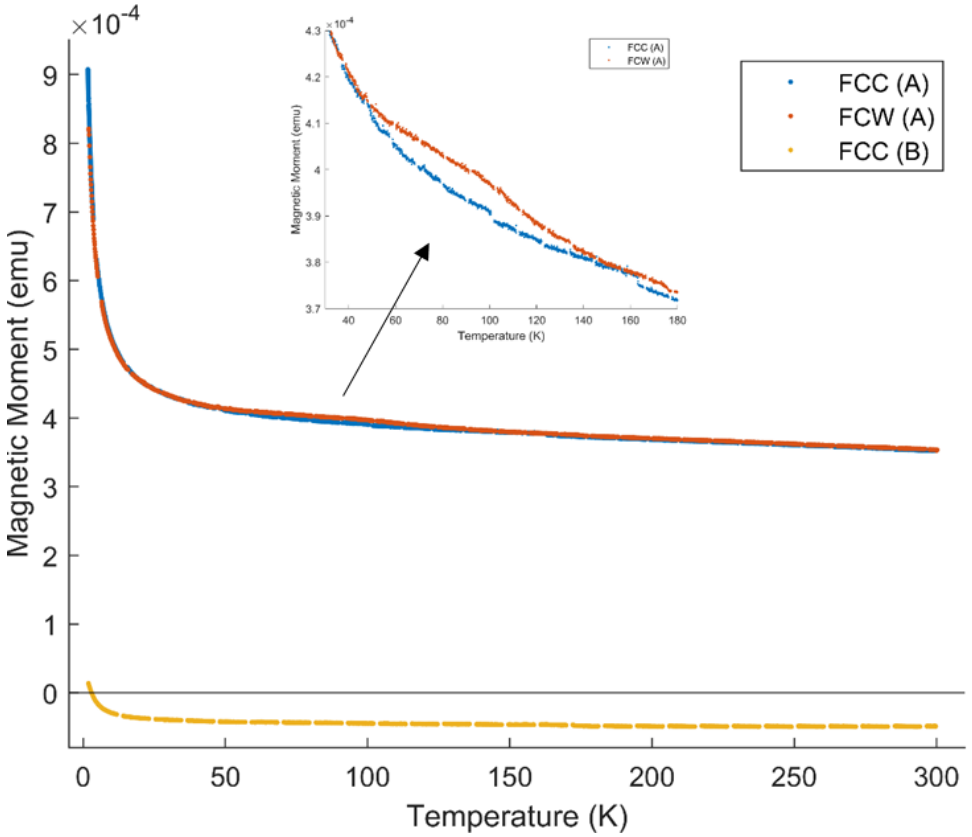

Figure 7.3: The magnetic moment as a function of the temperature of the samples A and B at 0.5 T. (FCC) and (FCW) represent the field-cooled cooling and warming respectively. The upper inset shows the FCC and FCW of sample "A" in a temperature range of 40-180K.

In order to determine whether the observed positive value of the magnetic moment as a function of temperature for sample "A" correspond to ferromagnetic or ferrimagnetic behaviour, the magnetic moments $\mu(H)$ versus the magnetic field H were measured at temperatures 2, 10, 50, 100, and 300K as shown in Figure 7.4. All curves are characterized by a hysteresis at all temperatures with a clear saturation of the magnetic moments μ_{Sat} (M_{Sat} = μ_{Sat}/mass) at high temperatures (> 100K). The magnetic moments reached saturation faster at high temperature, while at low temperature, the saturation of the magnetization was greater and a larger magnetic field H was required for saturation.

The remanent magnetization M_r of the sample exhibited a similar trend as the magnetic saturation M_S. The remanent magnetization M_r demonstrated a gradual increase as the sample temperature decreased. In contrast, the minimum magnetic coercivity H_c was recorded for a temperature of 50K and the maximum was recorded at 300K as seen in Table 7.2.

Table 7.2: The coercivity, saturation and remanent magnetic moments generated from the hysteresis at diverse temperatures.

Temperature (K)	$\mu_{Sat}\times10^{-4}$ (emu)	H_C(Oe)	$\mu_r\times10^{-5}$ (emu)
2	>8.5	-104	5.20
10	5.20	-111	4.80
50	4.16	-112.5	4.70
100	3.92	-92.5	3.95
300	3.54	-79	3.34

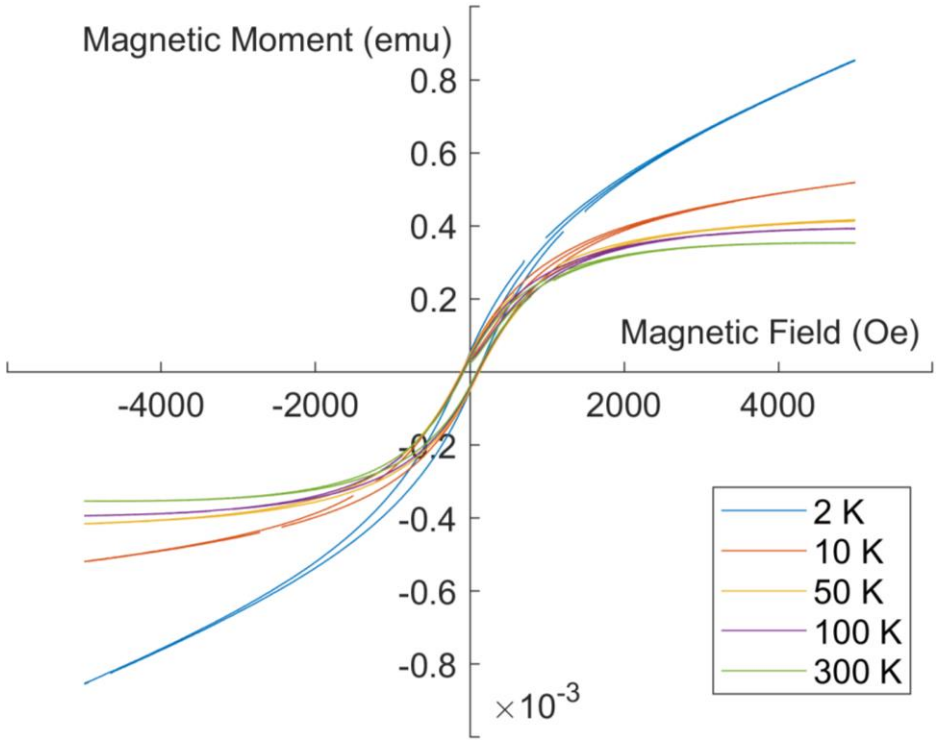

Figure 7.4: The magnetic moments $\mu(H)$ in a range of -0.5-0.5 T of sample "A" at temperatures 2, 10, 50, 100, and 300K. The curves show clearly the progress of the hysteresis at all temperatures.

The magnetic moment measurements $\mu(H)$ on sample "B" at temperatures of 2, 10, 50, 100, 200, and 300 K confirmed the conclusion drawn before from the $\mu(T)$ trend in Figure 7.3. The curves exhibit a clear diamagnetic behaviour above 2 K. In contrast, at 2 K the curve reveals a hysteresis with a very small width and a remanent magnetic moment of less than 3×10^{-5} emu. Moreover, the mass susceptibility above 50 K was calculated from Figure 7.5 to be ~-5.6×10^{-7} emu.g^{-1}.Oe^{-1}. This value is in good agreement with the susceptibility range of -(10^{-5}-10^{-7}) emu.g^{-1}.Oe^{-1} for carbon allotropes exhibiting diamagnetic behaviour [21]. Also, the appearance of positive magnetic moments at very low temperatures (>3 K) could be attributed to the retention of isolated paramagnetic spins in the carbon mass [21].

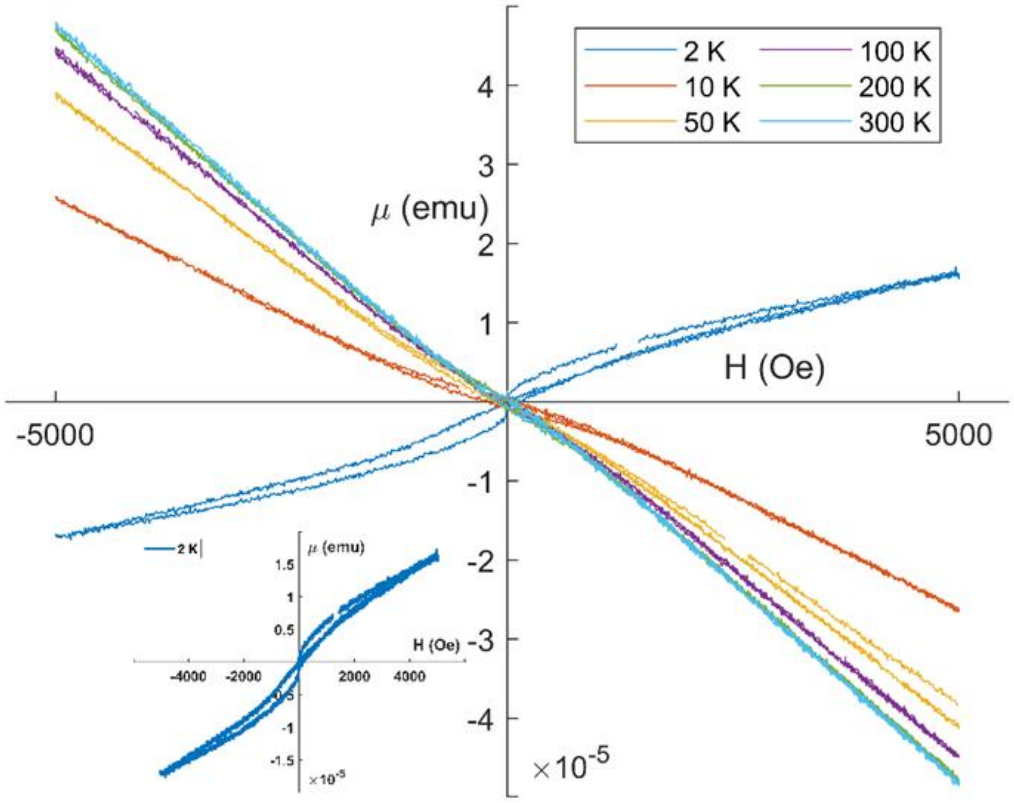

Figure 7.5: The magnetic moment $\mu(H)$ of sample "B" at temperatures 2, 10. 50, 100, 200, and 300 K. The curves show the diamagnetism at temperatures between 10 to 300 K, and superparamagnetic behaviour at 2 K. The down left inset shows clearly the ferromagnetic hysteresis at 2 K.

The above measurements point towards two different magnetic behaviours of the two different samples of carbon nanospheres investigated. With respect to $\mu(H)$, sample

“A” is characterized by ferromagnetic behaviour with a clear hysteresis observed at all temperatures, while sample” B” exhibits diamagnetism except at 2 K at which a hysteresis with small width is observed. These results are unusual as bulk carbon materials are known to be diamagnetic, and also, the samples were synthesized with the same method under similar conditions. The observed ferromagnetism in sample “A” might be as well attributed to the presence of magnetic impurities, however, if these cannot account quantitatively for the entire effect, then the rest of the magnetization must be related to magnetic moments induced within the carbon nanospheres.

The magnetism in carbon nanomaterials and the precise origin of ferromagnetism are still complicated and controversial. A number of different research studies have implied that carbon nanomaterials (carbon nanofoam, carbon nanospheres) could exhibit ferromagnetic behaviour without the introduction of magnetic elements [21]–[23], [129], but a well-defined explanation of such behaviour is still unclear.

In order to obtain a better understanding of the origin of ferromagnetism in the samples investigated, and determine whether the contribution of the ferromagnetic behaviour is intrinsic or extrinsic, more evidence was needed other than the magnetization measurements to supplement the reported results. Therefore, ICP-MS and Mossbauer analysis were performed on the two samples. The ICP-MS results are presented in Table 7.1, and have assisted in clarifying the possible contribution of the magnetic impurities in the samples towards the observed ferromagnetism.

The ICP-MS has shown that there exists only one magnetic impurity in the form of Fe in the samples “A” and “B”. The concentrations of Fe impurities were 126 ppm in sample “A” and 20 ppm in sample “B”. Concentrations of other magnetic elements such as Ni and Co were very low and less than 3 ppm (Ni) or not detectable at the ppm level (Co) for the two samples. The Fe impurity within the carbon nanospheres forms most probably complexes of FeC or FeO.

The saturation magnetization M_{Sat} for the samples “A” and “B” was estimated by extrapolation from the measured magnetization curves (Figure 7.4 and Figure 7.5) , to be 7.4×10^{-2} emu.g^{-1} and 2×10^{-3} emu.g^{-1} respectively. Given the amount of Fe impurity in the samples as measured by ICP-MS, the corresponding calculated magnetic saturation M_{Sat} values are expected to be of the order of 2.64×10^{-2} emu.g^{-1} and 4.44×10^{-3} emu.g^{-1} for sample “A” and “B” respectively, by making the gross assumption that all Fe atoms of the impurity content are participating in the form of magnetic complexes. This value for sample “A” is still 2.6 times lower than the observed magnetisation and it indicates that Fe cannot be the sole contributor to the magnetisation observed in these carbon nanospheres. We can speculate that the existence of edge states in sample A could also foster the localization of unpaired electrons and contribute to ferromagnetism.

In order to investigate further the possible origins of the observed ferromagnetic signal, Mossbauer spectroscopy was performed on the sample noted “A” with using iron ^{57}Fe as a source. As the concentration of Fe is extremely low, data were collected for more than 10 days (over 10000 counts) and the corresponding Mossbauer spectrum is presented in Figure 7.6. The spectrum is characterized by a weak signal in the form of a doublet around zero velocity with a large background. The signal is directly related to the presence of the iron element in the sample, and confirms the reported results by ICP-MS concerning the presence of Iron within the samples.

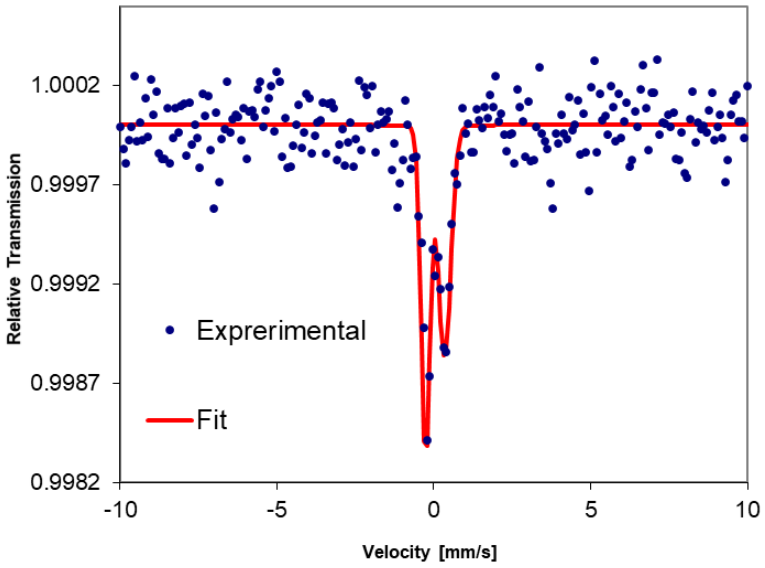

Figure 7.6: The Mossbauer data of sample “A” and its fit with a Lorentzian doublet.

The Mossbauer spectrum was fitted with a Lorentzian doublet. The characteristic parameters of this doublet such as the isomer shift, quadrupole splitting and Lorentzian linewidth have values 0.05, 0.5, and 0.25 mm/s respectively. By comparison to Mossbauer analysis results obtained in the literature [130] with respect to Fe inclusions in carbon materials, the present spectrum and the inferred associated parameters from the fit strongly suggest that the observed signal is due to Fe^{3+} and is of superparamagnetic nature. Moreover, the Fe^{3+} might also have ligand of hydrocarbon as the quadrupole splitting values found below 1 mm/s confirmed this observation [131].

It is important to note that in the Mossbauer spectrum no sextet signatures were detected, which is a typical characteristic of ferromagnetic Fe structures as shown by Alain Peigney *et al.* [130]. The Fe in the present samples therefore does not form ferromagnetic molecular complexes. This finding is important with respect to the clear ferromagnetic signal that has been observed for sample “A” using PPMS as it excludes the association of the observed ferromagnetism to Fe impurities.

The experimental data from ICP-MS and Mossbauer spectroscopy of sample “A” indicate that the observed ferromagnetic-like behaviour originate from s-p symmetry unpaired at structural defects rather than the d or f electrons of the magnetic impurities

[14], [17], [22]. Also, the hydrogen contents in the carbon nanospheres may play a significant role in the formation of the magnetic ordering as reported in [17].

Unlike sample “A”, sample “B” did not exhibit ferromagnetic-like behaviour (Figure 7.5). The absence of the ferromagnetism in sample “B” and its presence in sample “A” can be due to the difference in the morphology, size, and crystallinity of the two samples. A similar explanation is reported by Li *et al.* [14]. In the latter reference, it reveals that the disordered carbon with an interlayer spacing of 0.342 nm is diamagnetic, while the highly oriented pyrolytic graphite (HOPG) with a 0.337 nm spacing shows ferromagnetism. While at temperature below 10 K, the superparamagnetic characteristic or the spin-glass behaviour in sample “B” is attributed to the Fe nanoparticles of the impurities [14], [132].

7.1.2 Electronic properties

The electronic properties of carbon nanospheres and carbon nanomaterials, in general, are complicated and their behaviour (metallic or non-metallic) depends on many intrinsic characteristics such as structure, crystallinity, doping and defects. Moreover, the contact area between the carbon nanospheres plays an important role in the increase of the resistance within the carbon nanospheres network [133].

The electrical transport properties of the aforementioned CVD carbon nanospheres were investigated by performing electrical measurements on a pellet using a four-point probes system in the PPMS setup described above. These measurements included both resistance as well as magneto-resistance measurements.

The relevant results of these measurements from the carbon nanospheres pellets are presented in Figure 7.7. The measurements were conducted over a temperature range between 2-300 K, and the logarithmic of the inverse of the resistance (conductance) was plotted as a function of the inverse of the temperature too.

As seen in Figure 7.7, the resistance of the nanospheres network decreases non-linearly with the increase in the temperature, which indicates a nonmetallic behaviour of the sample. A logarithmic plot of the inverse of the resistance as a function of $T^{-1/4}$, shows that the electronic behaviour is described by three different sections. From 20 to 100 K, the resistance increases drastically with decreasing temperature, and the sample displays a semiconducting behaviour, while between 250 and 300 K, the resistance shows a linear relationship with the temperature. In the interval between the above two ranges (100-250 K), the resistance shows a transition-like point and decreases steadily.

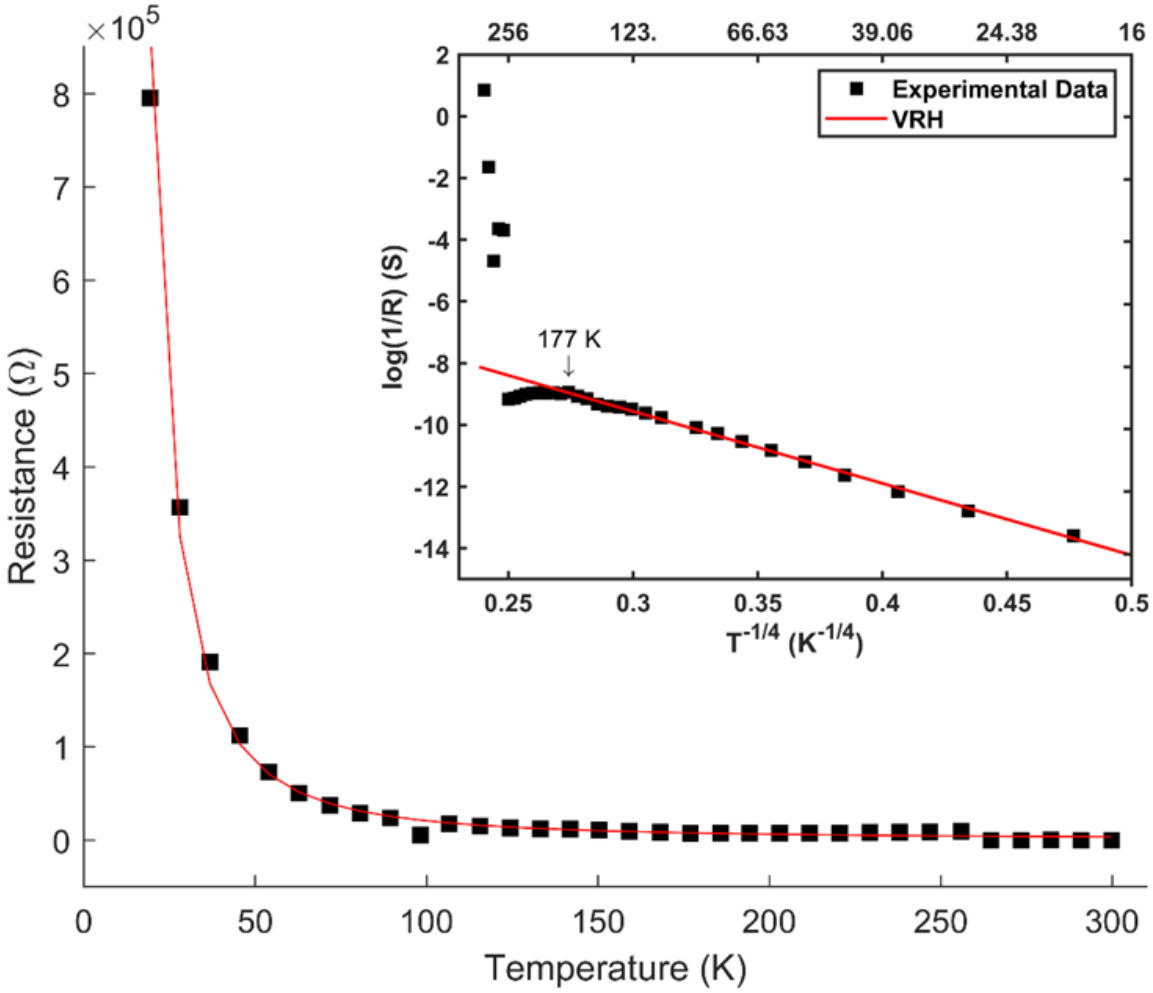

Figure 7.7: The resistance, logarithmic of the conductance as a function of the temperature in (K) and the fitted curves based on the 3D Variable Range Hopping (VRH). The absence of the data at low temperature (2-20 K) was related to the limitation of the PPMS, as very high resistance was measured within that temperature range. The upper axis represents the temperatures in (K).

Similar semiconducting features to the reported above were demonstrated in the literature for carbon microspheres [134], [135] and carbon nanotubes networks [133]. Furthermore, it has been reported that these non-metallic characteristics arise from disorder and defects within the structure of the carbon nanomaterials and have been successfully explained by the Variable Range Hopping (VRH) model [133]–[137]. It must be noted here that an important characteristic of the nanospheres studied in the present work is that they are of the order of 200-400 nanometres by comparison to the micrometre size of carbon spheres in [134], [135], and very importantly they have been produced without metal catalysts which have affected previous conductivity results in the literature.

According to the VRH model, the conduction in disordered carbon materials is mediated by hopping of the charge carriers between localized electronic states near the Fermi level in an extended temperature range. The process of electron hopping from one localized state to another is thermally assisted by phonons which offer the necessary energy, which explains the temperature dependence with respect to lattice vibrations modes.

In the VRH model, the resistance is expressed as a function of the Mott temperature T_0, the localization length L_c, and the density of states, $N(E_F)$, at the Fermi level [133], [136], [138]. In this model, the Mott characteristic temperature T_0, and the exponent n (1/2 (1D), 1/3 (2D), 1/4 (3D)) represent the degree of disorder and the hopping dimension respectively, expressed as

$$R(T) = R_0 \exp\left(\frac{T_0}{T}\right)^n \tag{7.1}$$

$$T_0 = \frac{24}{\pi k_B L_c^3 N(E_F)} \tag{7.2}$$

Based on the VRH model, the conduction in disordered carbon materials is displayed by the hop of the charge carriers between localized states located near the

Fermi level. The process of hopping is assisted by the phonons, which explains the temperature dependence.

From Figure 7.7 (R-T), the exponential escalation of the resistance with the decrease of the temperature reveals the strong localisation within the disordered carbon nanospheres network. Besides, at low temperature (2-180 K) the data are fitted with the 3D VRH model (n = 1/4), corresponding to the high disorder and the extreme localisation of the electrons within the carbon nanospheres. Moreover, the estimated value of the Mott characteristic temperature, T_0, and the subsequently deduced density of states $N(E_F)$ (7.2) were found to be 2.95×10^5 K and 3×10^{20} $eV^{-1}.cm^{-1}$ respectively. These are in good agreement with the ones which have been reported in the literature for a localisation length of 10 Å [136].

L. Wang *et al*. [133] reported on distinct electrical effects of multi-walled carbon nanotubes and their conductivity results, as shown in Figure 7.8, exhibit strong similarities with the ones presented here. Three distinct regions were also observed and the data were in good agreement with the VRH model.

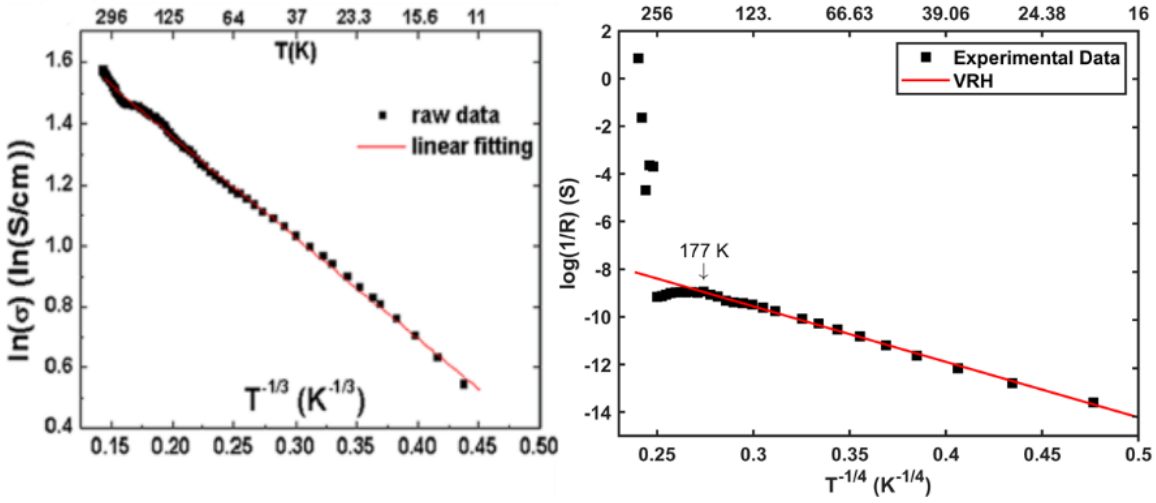

Figure 7.8: The graphs represent the temperature dependent conductivity of carbon nanotubes (left: from [133]) and carbon nanospheres (right: from our work) networks. The two graphs exhibit similarities concerning the evolution of the resistance as a function of the temperature.

In order to investigate the effect of the magnetic field on the charge carriers transport, magneto-resistance measurements were also conducted. For this, three different external magnetic fields of 0.5, 3, and 6 Tesla were applied while the magnetoresistance was measured with the same PPMS system described above. These electrical measurements were accomplished in a temperature range between 2-300 K. The acquired data was compared to the resistance measurements at zero fields.

The introduction of the magnetic field while measuring the conductivity of the carbon nanospheres network did not show any significant changes by comparison to the zero fields measurements, and the resistance in the presence of external magnetic fields showed again a semiconducting behaviour. Unfortunately, most of the quantum effects related to the introduction of the magnetic fields are taking place at very low temperatures (1-10 K), which are unattainable by the present PPMS setup.

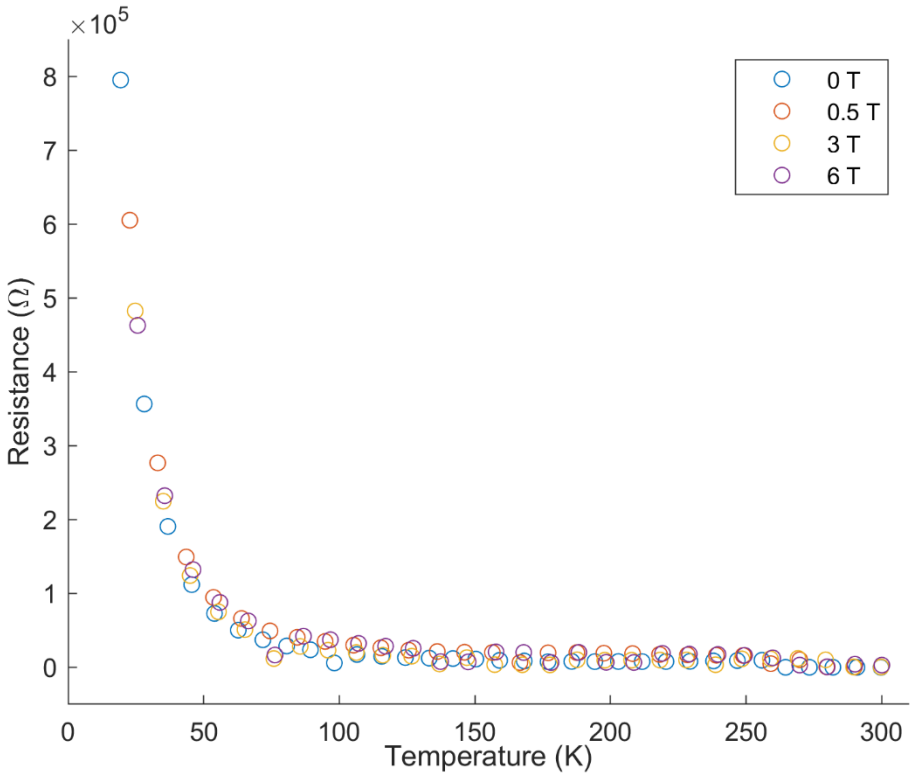

Figure 7.9: Magneto-resistance of the carbon nanospheres network at magnetics fields of 0, 0.5, 3, and 6 Tesla.

Chapter VIII

8 CONCLUSION

A novel technique for the synthesis of carbon nanomaterials based on the Pulsed Laser Ablation (PLA) method has been successfully developed. The PLA was chosen for its ability to control the power density deposited on the ablated surface as well as other physical parameters in order to achieve the necessary conditions required for inducing carbon phase transitions. In this manner, PLA was applied on highly oriented pyrolytic graphite surfaces, and an extensive investigation involving many different experiments took place in which critical parameters such as

- the energy density,
- number of laser pulses,
- the pulses repetition rate,
- as well as type and flow rates of catalysing confining gasses.

were carefully studied and considered.

The optimum conditions, within the available set up, were established making use of an ultraviolet pulsed laser with power densities in the order of 10^8 $W.cm^{-2}$ under the presence of hydrogen gas. The morphological and elemental characterisation carried out with Scanning Electron Microscopy revealed the existence of two different regions within a shockwave generated at the irradiated spots and the formation of pure carbon nanostructures with spherical shape. The diameter of the formed nanospheres is of the order between 40-50 nm, which is among the smallest reported in the literature so far.

Raman analysis of the laser impacted regions using micrometre size line-scans along the shockwave area confirmed the nano-structuration of the HOPG surfaces and the appearance of carbon nanospheres at specific shockwave regions. The Raman

extracted parameters from the spectra were shown to be in complete agreement with what has been suggested by Ferrari et al. [111], regarding phase transformation from graphite to nano-crystalline graphite in terms of

- the shift of the G peak from 1581 to ~1600 cm^{-1},
- the appearance of the D peak,
- an increase of I_D/I_G ratio, and
- the loss of the doublet of the 2D peak (~2700 cm^{-1}).

Previously reported Raman broad bands in the literature corresponding to the nanospheres in the range of 2700–3200 cm^{-1} have also been observed in the present work. The 2720 and 3242 cm^{-1} bands of HOPG are attributed to the second-order D (2D) and G (2G) modes respectively [110]. The observed band at 2950 cm^{-1} corresponds to the combination mode of D and G bands. The characteristics of these bands in terms of intensity, broadness, and red-shifts follow a well-established pattern reported in the literature [112], which is directly related to the growth of carbon nanostructures. Such a pattern can be noticeably seen in the present spectra (Figure 5.5 (b)). The 2720 cm^{-1} D' band progressively shifts to low frequencies, with broadening and decrease i)2D)n the intensity in the region of high nanospheres production. The 3242 cm^{-1} G' (2G) band follows a similar pattern until it almost disappears in the region of high production of nanospheres. These characterisations of the surfaces showed interesting evidence of surface nano-structuration.

The formation of nanospheres was found to depend on the generated heat along the propagation of the shockwave induced by the laser ablation. The important thermodynamic parameters, such as the temperature and pressure and plasma expansion, for the phase transition and the formation of nanospheres were calculated from the studies of the different fluences used and a P-T diagram was presented. From the same diagram, an explanation in regard to the optimum fluence was presented. The reason was found to be due the location of the applied fluence (2 $J.cm^{-2}$) within P-T diagram near the line that separates the solid and vapour carbon phases. These

calculations were based on the work of Burgess *et al.* [63] and Fabbro *et al.* [39] for different intensities, including the ones applied in our fluence study and confirmed that the use of the laser ablation offered the advantage of reproducibility of the results under optimum conditions. This reproducibility was introduced by the possibility of the laser to control the pressures and temperatures generated.

In addition, by referring to the fundamental theory of nucleation, we narrated in details and step by step the path that led to the transformation of HOPG to carbon nanospheres. Hence, processes such as nucleation and growth have been in the spotlight of our discussion. The calculations of the supersaturation $\Delta\mu$, nucleation work W_{nuc}^{*}, and the critical radius of the nuclei R_{nuc}^{*} were included in our research works and contributed to reasoning about the formation of the carbon nanospheres.

It was found that the minimum nucleation work W_{nuc}^{*} is 4.52×10^{-22} Joules, and for the nuclei to grow to become a cluster, its radius must be greater than R_{nuc}^{*}, and was calculated to be 0.479 Å. These values still have to be thoroughly verified due to the lack of related information in the literature. Also, the unidentified composition of the plasma-plume and the type of hydrocarbon bonding make it difficult to firmly confirm the calculated parameters (mostly for R_{nuc}^{*}). In the future work, the use of optical emission spectroscopy to characterise the generated plasma-plume may resolve this issue.

Furthermore, from the parameters study, the presence of hydrogen contents during the ablation of HOPG was found essential for the formation of carbon nanospheres. The study was conducted with H_2/Ar and CH_4 gasses. It was established that 15 and 2 sccm were the optimum flow rates respectively in regard to the formation of carbon nanospheres of high quality and production rate. Besides, the present study has confirmed the important role played by the hydrogen during the nucleation process.

The research was further extended to include studies of electronic and magnetic properties of carbon nanospheres grown with Chemical Vapour Deposition method using

a state of the art physical property measurement system. Scanning electron microscopy imaging of the two investigated sets of carbon nanospheres, grown under slightly different conditions, revealed a difference in size with diameters of about 200 and 400 nm respectively. Induced coupled plasma mass spectroscopy showed the presence of ferromagnetic impurities such as Fe, and Ni at concentration levels to be less than 120 and 3 ppm respectively. PPMS magnetic measurements of the two samples showed two different characteristics. In Sample “A”, with nanospheres of about 200 nm in diameter, clear ferromagnetism behaviour was observed, while in sample “B”, diamagnetic behaviour was observed except at low temperature (>10 K), at which clear superparamagnetic behaviour is observed. The gathered evidence from ICP-MS and Mössbauer spectroscopy showed that the observed ferromagnetism in the sample “A” is in excess of what it could be accounted for by the magnetic impurities introduced during the synthesis process. Presently, it is difficult to elaborate on the origin of the observed ferromagnetic behaviour and it will become the main focus of the future work with a series of new experiments and theoretical models.

For the electrical properties, the network of carbon nanospheres expressed a semiconducting behaviour, and fitted the 3D variable range hopping at temperature range in between 2-200K in agreement with work conducted on carbon nanotubes networks.

These properties of the carbon nanospheres discussed and described above, and more importantly the ferromagnetic behaviour, could open a door for biological related applications as drug delivery and photo-dynamic therapy. This characteristic of ferromagnetism without introducing any magnetic impurities makes these carbon nanospheres a good candidate for such applications.

REFERENCES

[1] W. Liu and G. Speranza, “Functionalization of Carbon Nanomaterials for Biomedical Applications,” *C—Journal of Carbon Research*, vol. 5, no. 4, p. 72, 2019.

[2] J. H. Warner, F. Schaffel, M. Rummeli, and A. Bachmatiuk, *Graphene: Fundamentals and emergent applications*. Newnes, 2012.

[3] F. Cowlard and J. Lewis, “Vitreous carbon—a new form of carbon,” *Journal of Materials Science*, vol. 2, no. 6, pp. 507–512, 1967.

[4] F. Bundy and J. Kasper, “Hexagonal diamond—a new form of carbon,” *The Journal of Chemical Physics*, vol. 46, no. 9, pp. 3437–3446, 1967.

[5] H. W. Kroto, J. R. Heath, S. C. O’Brien, R. F. Curl, and R. E. Smalley, “C60: Buckminsterfullerene,” *nature*, vol. 318, no. 6042, pp. 162–163, 1985.

[6] S. Iijima, “Helical microtubules of graphitic carbon,” *nature*, vol. 354, no. 6348, pp. 56–58, 1991.

[7] S. Iijima and T. Ichihashi, “Single-shell carbon nanotubes of 1-nm diameter,” *nature*, vol. 363, no. 6430, pp. 603–605, 1993.

[8] A. V. Rode, S. Hyde, E. Gamaly, R. Elliman, D. McKenzie, and S. Bulcock, “Structural analysis of a carbon foam formed by high pulse-rate laser ablation,” *Applied Physics A*, vol. 69, no. 1, pp. S755–S758, 1999.

[9] Y.-P. Sun *et al.*, “Quantum-sized carbon dots for bright and colorful photoluminescence,” *Journal of the American Chemical Society*, vol. 128, no. 24, pp. 7756–7757, 2006.

[10] I. Martin-Gullon, J. Vera, J. A. Conesa, J. L. González, and C. Merino, “Differences between carbon nanofibers produced using Fe and Ni catalysts in a floating catalyst reactor,” *Carbon*, vol. 44, no. 8, pp. 1572–1580, 2006.

[11] Y. Liu *et al.*, “Carbon nanorods,” *Chemical Physics Letters*, vol. 331, no. 1, pp. 31–34, 2000.

[12] A. A. Deshmukh, S. D. Mhlanga, and N. J. Coville, “Carbon spheres,” *Materials Science and Engineering: R: Reports*, vol. 70, no. 1–2, pp. 1–28, 2010.

[13] K. S. Novoselov *et al.*, “Electric field effect in atomically thin carbon films,” *science*, vol. 306, no. 5696, pp. 666–669, 2004.

[14] D. Li, Z. Han, B. Wu, D. Geng, and Z. Zhang, “Ferromagnetic and spin-glass behaviour of nanosized oriented pyrolytic graphite in Pb–C nanocomposites,” *Journal of Physics D: Applied Physics*, vol. 41, no. 11, p. 115005, 2008.

[15] Y. Murakami and H. Suematsu, “Magnetism of C60 induced by photo-assisted oxidation,” *Pure and applied chemistry*, vol. 68, no. 7, pp. 1463–1467, 1996.

[16] T. L. Makarova *et al.*, “Magnetic carbon,” *Nature*, vol. 413, no. 6857, pp. 716–718, 2001.

[17] P. Esquinazi, R. Höhne, K.-H. Han, A. Setzer, D. Spemann, and T. Butz, “Magnetic carbon: Explicit evidence of ferromagnetism induced by proton irradiation,” *Carbon*, vol. 42, no. 7, pp. 1213–1218, 2004.

[18] K. Han, D. Spemann, P. Esquinazi, R. Höhne, V. Riede, and T. Butz, “Ferromagnetic spots in graphite produced by proton irradiation,” *Advanced Materials*, vol. 15, no. 20, pp. 1719–1722, 2003.

[19] K. Kusakabe and Y. Takagi, “On possible surface magnetism in nanographite,” *Molecular Crystals and Liquid Crystals*, vol. 387, no. 1, pp. 7–11, 2002.

[20] M. Maruyama, K. Kusakabe, S. Tsuneyuki, K. Akagi, Y. Yoshimoto, and J. Yamauchi, “Magnetic properties of nanographite with modified zigzag edges,” *Journal of Physics and Chemistry of Solids*, vol. 65, no. 2–3, pp. 119–122, 2004.
[21] R. Caudillo, X. Gao, R. Escudero, M. Jose-Yacaman, and J. Goodenough, “Ferromagnetic behavior of carbon nanospheres encapsulating silver nanoparticles,” *Physical Review B*, vol. 74, no. 21, p. 214418, 2006.
[22] A. V. Rode *et al.*, “Unconventional magnetism in all-carbon nanofoam,” *Physical Review B*, vol. 70, no. 5, p. 054407, 2004.
[23] D. Arčon *et al.*, “Origin of magnetic moments in carbon nanofoam,” *Physical Review B*, vol. 74, no. 1, p. 014438, 2006.
[24] Y. Kopelevich, R. da Silva, J. Torres, A. Penicaud, and T. Kyotani, “Local ferromagnetism in microporous carbon with the structural regularity of zeolite Y,” *Physical Review B*, vol. 68, no. 9, p. 092408, 2003.
[25] C. T. White and T. N. Todorov, “Carbon nanotubes as long ballistic conductors,” *Nature*, vol. 393, no. 6682, pp. 240–242, 1998.
[26] F. Ghaemi, M. Ali, R. Yunus, and R. N. Othman, “Synthesis of carbon nanomaterials using catalytic chemical vapor deposition technique,” in *Synthesis, Technology and Applications of Carbon Nanomaterials*, Elsevier, 2019, pp. 1–27.
[27] V. Tornari, V. Zafiropulos, A. Bonarou, N. Vainos, and C. Fotakis, “Modern technology in artwork conservation: a laser-based approach for process control and evaluation,” *Optics and lasers in Engineering*, vol. 34, no. 4–6, pp. 309–326, 2000.
[28] R. A. Ismail, M. H. Mohsin, A. K. Ali, K. I. Hassoon, and S. Erten-Ela, “Preparation and characterization of carbon nanotubes by pulsed laser ablation in water for optoelectronic application,” *Physica E: Low-dimensional Systems and Nanostructures*, p. 113997, 2020.
[29] E. A. Ganash, G. A. Al-Jabarti, and R. M. Altuwirqi, “The synthesis of carbon-based nanomaterials by pulsed laser ablation in water,” *Materials Research Express*, vol. 7, no. 1, p. 015002, 2019.
[30] T. Milenov *et al.*, “Synthesis of graphene-like phases in a water colloid by laser ablation of graphite,” *Materials Science and Engineering: B*, vol. 247, p. 114379, 2019.
[31] S. Kamali, E. Solati, and D. Dorranian, “Effect of laser fluence on the characteristics of graphene nanosheets produced by pulsed laser ablation in water,” *Journal of Applied Spectroscopy*, vol. 86, no. 2, pp. 238–243, 2019.
[32] H. Sadeghi, E. Solati, and D. Dorranian, “Producing graphene nanosheets by pulsed laser ablation: Effects of liquid environment,” *Journal of Laser Applications*, vol. 31, no. 4, p. 042003, 2019.
[33] E. Shuaib, P. M. Shafi, G. K. Yogesh, A. C. Bose, and D. Sastikumar, “Carbon nanoparticles synthesized by laser ablation of coconut shell charcoal in liquids for glucose sensing applications,” *Materials Research Express*, vol. 6, no. 11, p. 115610, 2019.
[34] E. Vaghri, Z. Khalaj, and D. Dorranian, “Investigating the effects of different liquid environments on the characteristics of multilayer graphene and Graphene Oxide nanosheets synthesized by green laser ablation method,” *Diamond and Related Materials*, p. 107697, 2020.

[35] F. Gorrini *et al.*, “On the thermodynamic path enabling a room-temperature, laser-assisted graphite to nanodiamond transformation,” *Scientific reports*, vol. 6, p. 35244, 2016.
[36] L. Yang, P. May, L. Yin, J. Smith, and K. Rosser, “Growth of diamond nanocrystals by pulsed laser ablation of graphite in liquid,” *Diamond and Related Materials*, vol. 16, no. 4–7, pp. 725–729, 2007.
[37] J. Hao, L. Pan, S. Gao, H. Fan, and B. Gao, “Production of fluorescent nano-diamonds through femtosecond pulsed laser ablation,” *Optical Materials Express*, vol. 9, no. 12, pp. 4734–4741, 2019.
[38] X. Ren *et al.*, “A conversion model of graphite to ultrananocrystalline diamond via laser processing at ambient temperature and normal pressure,” *Applied Physics Letters*, vol. 105, no. 2, p. 021908, 2014.
[39] R. Fabbro, J. Fournier, P. Ballard, D. Devaux, and J. Virmont, “Physical study of laser-produced plasma in confined geometry,” *Journal of applied physics*, vol. 68, no. 2, pp. 775–784, 1990.
[40] N. B. Dahotre, *Lasers in surface engineering*, vol. 1. ASM international, 1998.
[41] W. M. Steen and J. Mazumder, “Basic laser optics,” in *Laser material processing*, Springer, 2010, pp. 79–130.
[42] S. Sundaram and E. Mazur, “Inducing and probing non-thermal transitions in semiconductors using femtosecond laser pulses,” *Nature materials*, vol. 1, no. 4, p. 217, 2002.
[43] M. v Allmen and A. Blatter, “Absorption of Laser Light,” in *Laser-beam interactions with materials: physical principles and applications*, Springer Science & Business Media, 2013, pp. 5–39.
[44] M. S. Brown and C. B. Arnold, “Fundamentals of laser-material interaction and application to multiscale surface modification,” in *Laser precision microfabrication*, Springer, 2010, pp. 91–120.
[45] D. R. Lide, *CRC handbook of chemistry and physics*, vol. 85. CRC press, 2004.
[46] D. Bäuerle, *Laser processing and chemistry*. Springer Science & Business Media, 2013.
[47] J.-C. Weeber, J. R. Krenn, A. Dereux, B. Lamprecht, Y. Lacroute, and J.-P. Goudonnet, “Near-field observation of surface plasmon polariton propagation on thin metal stripes,” *Physical review B*, vol. 64, no. 4, p. 045411, 2001.
[48] J. F. Seely, “Quantum theory of inverse bremsstrahlung absorption and pair production,” in *Laser interaction and related plasma phenomena*, Springer, 1974, pp. 835–847.
[49] M. Lenner, A. Kaplan, C. Huchon, and R. E. Palmer, “Ultrafast laser ablation of graphite,” *Physical Review B*, vol. 79, no. 18, p. 184105, 2009.
[50] A. Hu, M. Rybachuk, Q.-B. Lu, and W. Duley, “Direct synthesis of sp-bonded carbon chains on graphite surface by femtosecond laser irradiation,” *Applied Physics Letters*, vol. 91, no. 13, p. 131906, 2007.
[51] M. Currie *et al.*, “Quantifying pulsed laser induced damage to graphene,” *Applied Physics Letters*, vol. 99, no. 21, p. 211909, 2011.
[52] M. Huang, F. Zhao, Y. Cheng, N. Xu, and Z. Xu, “The morphological and optical characteristics of femtosecond laser-induced large-area micro/nanostructures on GaAs, Si, and brass,” *Optics express*, vol. 18, no. 104, pp. A600–A619, 2010.

[53] J. Bonse, S. Baudach, J. Krüger, W. Kautek, and M. Lenzner, “Femtosecond laser ablation of silicon–modification thresholds and morphology,” *Applied Physics A*, vol. 74, no. 1, pp. 19–25, 2002.
[54] Y. Jee, M. F. Becker, and R. M. Walser, “Laser-induced damage on single-crystal metal surfaces,” *JOSA B*, vol. 5, no. 3, pp. 648–659, 1988.
[55] B. K. Nayak, V. V. Iyengar, and M. C. Gupta, “Efficient light trapping in silicon solar cells by ultrafast-laser-induced self-assembled micro/nano structures,” *Progress in Photovoltaics: Research and Applications*, vol. 19, no. 6, pp. 631–639, 2011.
[56] X. Wang and X. Xu, “Thermoelastic wave induced by pulsed laser heating,” *Applied Physics A*, vol. 73, no. 1, pp. 107–114, 2001.
[57] B. R. Tull, J. E. Carey, E. Mazur, J. P. McDonald, and S. M. Yalisove, “Silicon surface morphologies after femtosecond laser irradiation,” *Mrs Bulletin*, vol. 31, no. 8, pp. 626–633, 2006.
[58] B. N. Chichkov, C. Momma, S. Nolte, F. Von Alvensleben, and A. Tünnermann, “Femtosecond, picosecond and nanosecond laser ablation of solids,” *Applied Physics A*, vol. 63, no. 2, pp. 109–115, 1996.
[59] M. v Allmen and A. Blatter, “Heating by Laser Light,” in *Laser-beam interactions with materials: physical principles and applications*, Springer Science & Business Media, 2013, pp. 41–65.
[60] L. V. Zhigilei, P. B. Kodali, and B. J. Garrison, “Molecular dynamics model for laser ablation and desorption of organic solids,” *The Journal of Physical Chemistry B*, vol. 101, no. 11, pp. 2028–2037, 1997.
[61] D. Bäuerle, “Fundamental Excitation Mechanisms,” in *Chemical Processing with Lasers*, Springer, 1986, pp. 5–35.
[62] J. Ready, *Effects of high-power laser radiation*. Elsevier, 2012.
[63] D. Burgess Jr, P. C. Stair, and E. Weitz, “Calculations of the surface temperature rise and desorption temperature in laser-induced thermal desorption,” *Journal of Vacuum Science & Technology A: Vacuum, Surfaces, and Films*, vol. 4, no. 3, pp. 1362–1366, 1986.
[64] D. Burgess Jr, R. Cavanagh, and D. King, “Laser-induced desorption: Thermal and nonthermal pathways,” *The Journal of chemical physics*, vol. 88, no. 10, pp. 6556–6569, 1988.
[65] M. J. Smith and others, “Femtosecond-laser irradiation as a platform for tailoring the optoelectronic properties of silicon,” PhD Thesis, Massachusetts Institute of Technology, 2012.
[66] A. Rousse *et al.*, “Non-thermal melting in semiconductors measured at femtosecond resolution,” *Nature*, vol. 410, no. 6824, p. 65, 2001.
[67] K. Sokolowski-Tinten, J. Bialkowski, and D. von der Linde, “Ultrafast laser-induced order-disorder transitions in semiconductors,” *Physical review B*, vol. 51, no. 20, p. 14186, 1995.
[68] M. Aziz, J. Tsao, M. O. Thompson, P. Peercy, and C. White, “Solute trapping: comparison of theory with experiment,” *Physical review letters*, vol. 56, no. 23, p. 2489, 1986.
[69] N. Bulgakova and A. Bulgakov, “Pulsed laser ablation of solids: transition from normal vaporization to phase explosion,” *Applied Physics A*, vol. 73, no. 2, pp. 199–208, 2001.

[70] M. Lenner, A. Kaplan, and R. Palmer, “Nanoscopic Coulomb explosion in ultrafast graphite ablation,” *Applied physics letters*, vol. 90, no. 15, p. 153119, 2007.
[71] P. Dyer, “Excimer laser polymer ablation: twenty years on,” *Applied Physics A*, vol. 77, no. 2, pp. 167–173, 2003.
[72] B. Luk’Yanchuk, N. Bityurin, S. Anisimov, and D. Bäuerle, “Photophysical ablation of organic polymers,” in *Excimer Lasers*, Springer, 1994, pp. 59–77.
[73] J.-L. Boulnois, “Photophysical processes in recent medical laser developments: a review,” *Lasers in medical science*, vol. 1, no. 1, pp. 47–66, 1986.
[74] H. S. Niehoff and F. Vollertson, “Laser induced shock waves in deformation processing,” *Metalurgija*, vol. 11, no. 3, pp. 183–194, 2005.
[75] Q. Nian *et al.*, “Direct laser writing of nanodiamond films from graphite under ambient conditions,” *Scientific reports*, vol. 4, p. 6612, 2014.
[76] D. Veysset, T. Pezeril, S. Kooi, A. Bulou, and K. A. Nelson, “Laser-induced versus shock wave induced transformation of highly ordered pyrolytic graphite,” *Applied Physics Letters*, vol. 106, no. 16, p. 161902, 2015.
[77] D. Devaux, R. Fabbro, L. Tollier, and E. Bartnicki, “Generation of shock waves by laser-induced plasma in confined geometry,” *Journal of Applied Physics*, vol. 74, no. 4, pp. 2268–2273, 1993.
[78] T. Pezeril *et al.*, “Direct visualization of laser-driven focusing shock waves,” *Physical review letters*, vol. 106, no. 21, p. 214503, 2011.
[79] C. Phipps Jr *et al.*, “Impulse coupling to targets in vacuum by KrF, HF, and CO2 single-pulse lasers,” *Journal of Applied Physics*, vol. 64, no. 3, pp. 1083–1096, 1988.
[80] S. Besner and M. Meunier, “Laser synthesis of nanomaterials,” in *Laser Precision Microfabrication*, Springer, 2010, pp. 163–187.
[81] P. M. Ossi and M. Dinescu, “Creating nanostructures with lasers,” in *Laser Processing of Materials*, Springer, 2010, pp. 131–167.
[82] M. N. Ashfold, F. Claeyssens, G. M. Fuge, and S. J. Henley, “Pulsed laser ablation and deposition of thin films,” *Chemical Society Reviews*, vol. 33, no. 1, pp. 23–31, 2004.
[83] D. R. NORTON, “Pulsed Laser Deposition of Complex Materials: Progress,” *Pulsed laser deposition of thin films: applications-led growth of functional materials*, p. 1, 2007.
[84] C. W. Schneider and T. Lippert, “Laser ablation and thin film deposition,” in *Laser Processing of Materials*, Springer, 2010, pp. 89–112.
[85] L. J. Lewis and D. Perez, “Theory and simulation of laser ablation–from basic mechanisms to applications,” in *Laser precision microfabrication*, Springer, 2010, pp. 35–61.
[86] D. Kashchiev, “Driving Force for Nucleation,” in *Nucleation*, Elsevier, 2000, pp. 9–16.
[87] D. Kashchiev, “First-order phase transitions,” in *Nucleation*, Elsevier, 2000, pp. 3–9.
[88] D. Kashchiev, “Work for cluster formation,” in *Nucleation*, Elsevier, 2000, pp. 17–45.
[89] L. B. Freund and S. Suresh, “Introduction and Overview,” in *Thin film materials: stress, defect formation and surface evolution*, Cambridge University Press, 2004, pp. 1–91.
[90] D. Kashchiev, “Nucleus size and nucleation work,” in *Nucleation*, Elsevier, 2000, pp. 45–55.

[91] W. Hoff and C. K. Rhodes, “Introduction,” in *Excimer Lasers*, Springer, 1994, pp. 1–4.
[92] C. A. Brau, “Rare gas halogen excimers,” in *Excimer Lasers*, Springer, 1994, pp. 87–137.
[93] M. Krauss and F. Mies, “Electronic structure and radiative transitions of excimer systems,” in *Excimer Lasers*, Springer, 1979, pp. 5–46.
[94] *Excimer lasers with magnetic switch control (EMG 100-200 MSC series)*. Lambda Physik.
[95] W. J. Marshall, “Two methods for measuring laser beam diameter,” *Journal of Laser Applications*, vol. 22, no. 4, pp. 132–136, 2010.
[96] M. Mylonakis *et al.*, “Simple precision measurements of optical beam sizes,” *Applied Optics*, vol. 57, no. 33, pp. 9863–9867, 2018.
[97] “Standard normal distribution table.” https://www.math.arizona.edu/~rsims/ma464/standardnormaltable.pdf (accessed Dec. 25, 2019).
[98] W. Wasel, K. Kuwana, P. T. Reilly, and K. Saito, “Experimental characterization of the role of hydrogen in CVD synthesis of MWCNTs,” *Carbon*, vol. 45, no. 4, pp. 833–838, 2007.
[99] M. Losurdo, M. M. Giangregorio, P. Capezzuto, and G. Bruno, “Graphene CVD growth on copper and nickel: role of hydrogen in kinetics and structure,” *Physical Chemistry Chemical Physics*, vol. 13, no. 46, pp. 20836–20843, 2011.
[100] Y. Li, K. Ji, Y. Duan, G. Meng, and Z. Dai, “Effect of hydrogen concentration on the growth of carbon nanotube arrays for gecko-inspired adhesive applications,” *Coatings*, vol. 7, no. 12, p. 221, 2017.
[101] M. Aksak and Y. Selamet, “Carbon nanotube diameter tuning using hydrogen amount and temperature on SiO 2/Si substrates,” *Applied Physics A*, vol. 100, no. 1, pp. 213–222, 2010.
[102] K. A. Shah and B. A. Tali, “Synthesis of carbon nanotubes by catalytic chemical vapour deposition: A review on carbon sources, catalysts and substrates,” *Materials Science in Semiconductor Processing*, vol. 41, pp. 67–82, 2016.
[103] B. Shukla, T. Saito, S. Ohmori, M. Koshi, M. Yumura, and S. Iijima, “Interdependency of gas phase intermediates and chemical vapor deposition growth of single wall carbon nanotubes,” *Chemistry of Materials*, vol. 22, no. 22, pp. 6035–6043, 2010.
[104] L. Reimer, *Scanning electron microscopy: physics of image formation and microanalysis*, vol. 45. Springer, 2013.
[105] S. Prawer and R. J. Nemanich, “Raman spectroscopy of diamond and doped diamond,” *Philosophical Transactions of the Royal Society of London. Series A: Mathematical, Physical and Engineering Sciences*, vol. 362, no. 1824, pp. 2537–2565, 2004.
[106] P. K. Chu and L. Li, “Characterization of amorphous and nanocrystalline carbon films,” *Materials Chemistry and Physics*, vol. 96, no. 2–3, pp. 253–277, 2006.
[107] S. Panchatsharam, B. Tan, and K. Venkatakrishnan, “Femtosecond laser-induced shockwave formation on ablated silicon surface,” *Journal of Applied Physics*, vol. 105, no. 9, p. 093103, 2009.

[108] G. Jenkins, “Analysis of the stress-strain relationships in reactor grade graphite,” *British Journal of Applied Physics*, vol. 13, no. 1, p. 30, 1962.
[109] O. Slagle, “Deformation mechanisms in polycrystalline graphite,” *Journal of the American Ceramic Society*, vol. 50, no. 10, pp. 495–500, 1967.
[110] S. Reich and C. Thomsen, “Raman spectroscopy of graphite,” *Philosophical Transactions of the Royal Society of London. Series A: Mathematical, Physical and Engineering Sciences*, vol. 362, no. 1824, pp. 2271–2288, 2004.
[111] A. C. Ferrari and J. Robertson, “Interpretation of Raman spectra of disordered and amorphous carbon,” *Physical review B*, vol. 61, no. 20, p. 14095, 2000.
[112] J.-Y. Miao *et al.*, “Synthesis and properties of carbon nanospheres grown by CVD using Kaolin supported transition metal catalysts,” *Carbon*, vol. 42, no. 4, pp. 813–822, 2004.
[113] L. Cançado *et al.*, “General equation for the determination of the crystallite size L a of nanographite by Raman spectroscopy,” *Applied Physics Letters*, vol. 88, no. 16, p. 163106, 2006.
[114] W. Lee and J. H. Moon, “Monodispersed N-doped carbon nanospheres for supercapacitor application,” *ACS applied materials & interfaces*, vol. 6, no. 16, pp. 13968–13976, 2014.
[115] J. Lahaye and F. Ehrburger-Dolle, “Mechanisms of carbon black formation. Correlation with the morphology of aggregates,” *Carbon*, vol. 32, no. 7, pp. 1319–1324, 1994.
[116] Y. Chen, M. Conway, J. F. Gerald, J. Williams, and L. Chadderton, “The nucleation and growth of carbon nanotubes in a mechano-thermal process,” *Carbon*, vol. 42, no. 8–9, pp. 1543–1548, 2004.
[117] X. Wang *et al.*, “The effect of hydrogen on the formation of carbon nanotubes and fullerenes,” *Journal of Materials Research*, vol. 10, no. 8, pp. 1977–1983, 1995.
[118] Y. Zhang, W. Yang, R. Luo, and H. Shang, “Preparation of carbon nanospheres by non-catalytic chemical vapor deposition and their formation mechanism,” *New Carbon Materials*, vol. 31, no. 5, pp. 467–474, 2016.
[119] V. G. Pol, S. V. Pol, J. M. C. Moreno, and A. Gedanken, “High yield one-step synthesis of carbon spheres produced by dissociating individual hydrocarbons at their autogenic pressure at low temperatures,” *Carbon*, vol. 44, no. 15, pp. 3285–3292, 2006.
[120] Q. Lu, S. S. Mao, X. Mao, and R. E. Russo, “Theory analysis of wavelength dependence of laser-induced phase explosion of silicon,” *Journal of Applied Physics*, vol. 104, no. 8, p. 083301, 2008.
[121] A. Kar and J. Mazumder, “Mathematical model for laser ablation to generate nanoscale and submicrometer-size particles,” *Physical review E*, vol. 49, no. 1, p. 410, 1994.
[122] A. Gnedovets, A. Gusarov, and I. Smurov, “A model for nanoparticles synthesis by pulsed laser evaporation,” *Journal of Physics D: Applied Physics*, vol. 32, no. 17, p. 2162, 1999.
[123] M. Tillack, D. Blair, and S. Harilal, “The effect of ionization on cluster formation in laser ablation plumes,” *Nanotechnology*, vol. 15, no. 3, p. 390, 2004.

[124] J. Perrière, C. Boulmer-Leborgne, R. Benzerga, and S. Tricot, “Nanoparticle formation by femtosecond laser ablation,” *Journal of Physics D: Applied Physics*, vol. 40, no. 22, p. 7069, 2007.
[125] E. Lescoute *et al.*, “Experimental observations and modeling of nanoparticle formation in laser-produced expanding plasma,” *Physics of Plasmas*, vol. 15, no. 6, p. 063507, 2008.
[126] S.-B. Wen, X. Mao, R. Greif, and R. E. Russo, “Experimental and theoretical studies of particle generation after laser ablation of copper with a background gas at atmospheric pressure,” *Journal of applied physics*, vol. 101, no. 12, p. 123105, 2007.
[127] S. A. Irimiciuc, B. C. Hodoroaba, G. Bulai, S. Gurlui, and V. Craciun, “Multiple structure formation and molecule dynamics in transient plasmas generated by laser ablation of graphite,” *Spectrochimica Acta Part B: Atomic Spectroscopy*, vol. 165, p. 105774, 2020.
[128] Z. Jaworski, B. Zakrzewska, and P. Pianko-Oprych, “On thermodynamic equilibrium of carbon deposition from gaseous CHO mixtures: updating for nanotubes,” *Reviews in Chemical Engineering*, vol. 33, no. 3, pp. 217–235, 2017.
[129] P. Esquinazi *et al.*, “Ferromagnetism in oriented graphite samples,” *Physical Review B*, vol. 66, no. 2, p. 024429, 2002.
[130] A. Peigney, P. Coquay, E. Flahaut, R. E. Vandenberghe, E. De Grave, and C. Laurent, “A study of the formation of single-and double-walled carbon nanotubes by a CVD method,” *The Journal of Physical Chemistry B*, vol. 105, no. 40, pp. 9699–9710, 2001.
[131] G. Argouarch, P. Thominot, F. Paul, L. Toupet, and C. Lapinte, “Metallacumulenylidene complexes in the [(η5-C5Me5)(η2-dppe) Fe (= C (= C) nR2)] X (n= 0, 1, 2) series: investigations of the iron-carbon bonding by Mössbauer spectroscopy and X-ray analyses,” *Comptes Rendus Chimie*, vol. 6, no. 2, pp. 209–222, 2003.
[132] B. Martinez, X. Obradors, L. Balcells, A. Rouanet, and C. Monty, “Low temperature surface spin-glass transition in γ-Fe 2 O 3 nanoparticles,” *Physical Review Letters*, vol. 80, no. 1, p. 181, 1998.
[133] L. Wang, H. Wang, T. Datta, M. Yin, and X. Tian, “Distinct electrical effects of multi-walled carbon nanotubes in two composites,” *Journal of Applied Physics*, vol. 116, no. 17, p. 173708, 2014.
[134] W. P. Wright, V. Marsicano, J. Keartland, R. Erasmus, S. Dube, and N. Coville, “The electrical transport properties of nitrogen doped carbon microspheres,” *Materials Chemistry and Physics*, vol. 147, no. 3, pp. 908–914, 2014.
[135] K. C. Mondal *et al.*, “Boron-doped carbon microspheres,” *Materials Chemistry and Physics*, vol. 114, no. 2–3, pp. 973–977, 2009.
[136] K. G. Raj and P. A. Joy, “Cross over from 3D variable range hopping to the 2D weak localization conduction mechanism in disordered carbon with the extent of graphitization,” *Physical Chemistry Chemical Physics*, vol. 17, no. 24, pp. 16178–16185, 2015.
[137] A. Imani, G. Farzi, and A. Ltaief, “Facile synthesis and characterization of polypyrrole-multiwalled carbon nanotubes by in situ oxidative polymerization,” *International Nano Letters*, vol. 3, no. 1, p. 52, 2013.

[138] M. Campos and B. Bello Jr, “Mechanism of conduction in doped polyaniline,” *Journal of Physics D: Applied Physics*, vol. 30, no. 10, p. 1531, 1997.